

Study of Spin Dynamics in III-V Quantum Dots  
by Time Resolved Kerr Rotation

Atsushi KANNO

January 2005

Study of Spin Dynamics in III-V Quantum Dots  
by Time Resolved Kerr Rotation

Atsushi KANNO

(Doctoral Program in Frontier Science)

Submitted to the Graduate School of  
Pure and Applied Sciences  
in Partial Fulfillment of the Requirements  
for the Degree of Doctor of Philosophy in Science  
at the  
University of Tsukuba

# Abstract

Time-resolved Kerr rotation measurement is a useful method to probe dynamics of photoexcited carrier spins under the resonant excitation. By using a photoelastic modulator, a balanced detector with an optical bridge and tandem double lock-in amplifiers, we successfully developed a very sensitive Kerr rotation measurement system. Its angle resolution reached to about  $5 \times 10^{-6}$  degrees, and is the highest resolution in the world. Using this system, we could observe the carrier spin dynamics in two kinds of samples containing quantum dots in a single layer.

In strain-induced GaAs quantum dots, we observed a Larmor precession of photoexcited electron spins under the transverse magnetic field at 10 K. The observed spin coherence time is longer than that for a quantum well. This may suggest that the spin relaxation by D'yakonov-Perel' mechanism is suppressed as a result of the reduction of the dimensions from a quantum well (two-dimension) to a quantum dot (zero-dimension). At low temperature, the dominant mechanism of the spin relaxation is Bir-Aronov-Pikus mechanism for nanostructures. We also estimated electron g-factors for quantum dots and a quantum well from the observed periods of the beat coming from electron Larmor precessions. These results are consistent with the results of time-resolved photoluminescence quantum beat measurements under the magnetic field.

In self-assembled InP quantum dots, we observed a Larmor precession of photoexcited hole spins owing to electron doping from an n-GaAs substrate to the quantum dots. Based on the Pauli principle, a photoexcited electron and a doped electron should have anti-parallel spins in a quantum dot, and their magnetic moments become canceled. Then we observed a Larmor precession of only hole spins. The observed g-factor was very small and the value was consistent with another report of the g-factor of a heavy hole spin in GaAs quantum well. This fact sup-

ports that the observed beats are due to the hole spin precession. In addition, we observed that the spin relaxation time and the g-factor of the electron for GaAs/InGaP interface are controlled by applying electric bias.

Using the time-resolved Kerr rotation as a probe, we could investigate spin dynamics in a single-layer quantum dots in detail.

# Contents

<b>1</b>	<b>Introduction</b>	<b>1</b>
<b>2</b>	<b>Fundamentals</b>	<b>4</b>
2.1	Principles of Magnet-optical Kerr Effect . . . . .	4
2.1.1	Uniaxial Magnetization and Off-diagonal Components of Dielectric Tensor . . . . .	4
2.1.2	Polar Kerr Effect under the Normal Incident Condition . . . . .	6
2.1.3	Photo-induced Kerr Rotation . . . . .	8
2.2	Highly Sensitive Kerr Rotation Detection by Means of a Photoelastic Modulator	12
2.3	Carrier Spin Dynamics in Semiconductor Nanostructures . . . . .	17
2.4	Electronic and Optical Properties . . . . .	22
2.4.1	Bulk GaAs and InP . . . . .	22
2.4.2	Strain-induced GaAs Quantum Dots . . . . .	22
2.4.3	Self-assembled InP Quantum Dots . . . . .	25
<b>3</b>	<b>Experimental Setup</b>	<b>36</b>
<b>4</b>	<b>Results and Discussion</b>	<b>42</b>
4.1	Strain-induced GaAs Quantum Dots . . . . .	42
4.2	Self-assembled InP Quantum Dots . . . . .	60
<b>5</b>	<b>Conclusion</b>	<b>74</b>

# Chapter 1

## Introduction

In recent years, the quantum information processing technology (QIPT) is the most attractive topic to overcome the limit of the present computation and communication technologies. Many research projects of the QIPT in various fields are proceeding all over the world.

An electron spin in semiconductor is one of the most promising candidates for a quantum bit (qubit) [1]. Especially in a semiconductor quantum dot, the so-called *artificial atom*, there is a possibility of a long spin coherence time due to a suppression of spin relaxation by three-dimensional confinement of electrons.

Many kinds of spin relaxation measurements have been performed in quantum wells and bulk semiconductors. In quantum dots, the spin relaxation measurements such as optical orientation in steady photoluminescence, Hanle effect [2] and time-resolved photoluminescence [3–9] have been done. The measurement under the resonant excitation, however, is rare because photoluminescence spectroscopy is difficult under this condition [10, 11].

In this work, we constructed a highly sensitive measurement system of time-resolved Kerr rotation (TRKR). This is a useful method to observe carrier spin dynamics under the resonant excitation. The angle resolution in this system was higher than those reported by any other groups by 2 to 10 times [12–16]. Therefore, we could observe carrier spin dynamics in single-layer quantum dots under the resonant excitation for the first time.

We used two kinds of single-layer III-V quantum dots samples. In strain-induced GaAs quantum dots (SIQDs), we succeeded in observing the spin relaxation of photoexcited elec-

trons. The result was in good agreement with the photoluminescence quantum beat measurement [17]. The observed spin coherence time in quantum dots was longer than that in a quantum well because of suppression of the spin relaxation. We observed that the spin relaxation times are almost constant at low temperature. This may indicate that the spin relaxation mechanism of D'yakonov-Perel' (DP) model [18] was suppressed as a result of the reduction of the dimensions from quantum well (two-dimension) to quantum dot (zero-dimension), and the dominant mechanism of the spin relaxation at low temperature is Bir-Aronov-Pikus (BAP) mechanism [18,19]. On the other hand, in negatively charged (electron doped) self-assembled InP quantum dots, we observed the spin relaxation of photoexcited holes. As doped electron already exists in a negatively charged quantum dot, a photoexcited electron and the doped electron should have anti-parallel spins and their magnetic moments become canceled out. Thus, in this case, we do not observe the Larmor precessions of electron spins. As a result, Larmor precession of only the photoexcited hole spins became observed. The absolute value of the observed hole g-factor was consistent with the value measured by the photoluminescence quantum beat [7] and with the hole g-factor of the GaAs quantum well [5]. In addition, we observed that the g-factor and the spin relaxation time of the electron for GaAs/InGaP interface are controlled by applying electric bias.

Using the developed TRKR system, we can observe the spin dynamics in single-layer quantum dots under the resonant excitation.

This paper consists of the following chapters.

**Chapter 2: Fundamentals** shows the fundamentals of magneto-optical Kerr effect first. Then we explain the highly sensitive detection of the Kerr rotation by means of a photoelastic modulator and spin relaxation mechanisms in semiconductor nanostructures. The sample structures of single-layer quantum dots are also shown.

The experimental setup and the angle resolution of the Kerr rotation are shown in **Chapter 3: Experimental Setup**.

In **Chapter 4: Results and Discussion**, we discuss the results in strain-induced quantum dots and negatively charged self-assembled InP quantum dots. We got spin lifetimes, about 30 ps in a quantum well of the SIQDs, 91 ps in quantum dots of the SIQDs, and 98 ps in the InP quantum dots. The carrier g-factors are also given by beat periods of the TRKR signals. In the SIQDs, we observed the suppression of the spin relaxation compared with a quantum well. It is considered that this suppression comes from the absence of the DP mechanism in the zero-dimension. At low temperature, the spin relaxation times are almost constant due to the BAP mechanism. In InP quantum dots, we observed the hole spin precession, owing to the cancellation of the signals of the magnetic moments of anti-parallel spins of a doped electron and a photoexcited electron.

**Chapter 5: Conclusion** summarizes this paper.

# Chapter 2

## Fundamentals

### 2.1 Principles of Magnet-optical Kerr Effect

To investigate the spin dynamics of photoexcited carriers, we can employ techniques of four-wave mixing and optical orientation in steady and time-resolved photoluminescence. In spite of these techniques, the measurement by means of the magneto-optical effect is highly sensitive for probing the carrier spin dynamics under the resonant excitation. In this work, we measured spin dynamics of carriers by the magneto-optical Kerr effect, which is one of the magneto-optic effects observed under the external magnetic field.

#### 2.1.1 Uniaxial Magnetization and Off-diagonal Components of Dielectric Tensor

We discuss the principle of magneto-optical Kerr effect in a phenomenological way first [20]. It is possible to describe the Kerr effect by the off-diagonal components of a dielectric tensor under the magnetic field. For simplicity, we discuss only the isotropic material as follows.

Let us take the  $z$  axis as the direction of the magnetization  $M$  and the magnetic field. Then one-axis anisotropy in this direction is caused by the field. The dielectric tensor,

$$\epsilon = \begin{pmatrix} \epsilon_{xx} & \epsilon_{xy} & \epsilon_{xz} \\ \epsilon_{yx} & \epsilon_{yy} & \epsilon_{yz} \\ \epsilon_{zx} & \epsilon_{zy} & \epsilon_{zz} \end{pmatrix},$$

should not be changed for the rotation around the  $z$  axis. Then from the rotation invariance,  $C_4^{-1}\epsilon C_4 = \epsilon$  where  $C_4$  means a four-fold rotational symmetry, the tensor components are given

by

$$\epsilon = \begin{pmatrix} \epsilon_{xx} & \epsilon_{xy} & 0 \\ -\epsilon_{xy} & \epsilon_{xx} & 0 \\ 0 & 0 & \epsilon_{zz} \end{pmatrix}.$$

When we substitute electromagnetic plane-wave functions,

$$\mathbf{E} = \mathbf{E}_0 e^{-i\omega t} \cdot e^{i\mathbf{k}\cdot\mathbf{r}},$$

$$\mathbf{H} = \mathbf{H}_0 e^{-i\omega t} \cdot e^{i\mathbf{k}\cdot\mathbf{r}},$$

to the Maxwell equations,

$$\begin{aligned} \text{rot}\mathbf{E} &= -\frac{\partial\mathbf{B}}{\partial t}, \\ \text{rot}\mathbf{H} &= \frac{\partial\mathbf{D}}{\partial t} + \mathbf{J}, \end{aligned}$$

in the conditions  $\mathbf{J} = 0$ ,  $\mathbf{B} = \mu_0\mathbf{H}$  and  $\mathbf{D} = \epsilon\epsilon_0\mathbf{E}$ , we obtain the following equation,

$$(\mathbf{E} \cdot \mathbf{k})\mathbf{k} - |\mathbf{k}|^2\mathbf{E} + (\omega/c)^2\epsilon\mathbf{E} = 0.$$

Since wavevector  $\mathbf{k}$  is written as  $\hat{N} = ck/\omega$  ( $\hat{N} = n + i\kappa$ ) using a complex refractive index,

$$\mathbf{E} = \mathbf{E}_0 e^{-i\omega\left(t - \frac{\hat{N}}{c}\cdot\mathbf{r}\right)}.$$

Thus, we obtain the following equation,

$$\hat{N}^2\mathbf{E} - (\mathbf{E} \cdot \hat{N})\hat{N} - \epsilon\mathbf{E} = 0.$$

When the propagation direction of light is parallel to the  $z$  axis (the *Faraday configuration*), the secular equation is described by

$$\begin{pmatrix} \hat{N}^2 - \epsilon_{xx} & -\epsilon_{xy} & 0 \\ \epsilon_{xy} & \hat{N}^2 - \epsilon_{yy} & 0 \\ 0 & 0 & -\epsilon_{zz} \end{pmatrix} \begin{pmatrix} E_x \\ E_y \\ E_z \end{pmatrix} = 0.$$

When  $\mathbf{E}$  has non-zero solutions,  $\hat{N}$  has two eigenvalues  $\hat{N}^2 = \epsilon_{xx} \pm i\epsilon_{xy}$ . The vectors corresponding to these eigenvalues are described by  $\mathbf{E}_{\pm} = \frac{E_0}{2}(\mathbf{x} \pm i\mathbf{y})e^{-i\omega\left(t - \frac{\hat{N}_{\pm}}{c}z\right)}$ . We note that  $\mathbf{E}_+$  and  $\mathbf{E}_-$  correspond to the right and left circularly polarized light, respectively.

## 2.1.2 Polar Kerr Effect under the Normal Incident Condition

In the Faraday configuration under the normal incident condition, the direction of the magnetization is along the direction of the incident light. Then we can only consider polar Kerr effect as follows because the direction of the magnetization is along the incident light. It is a kind of magneto-optical Kerr effects.

The Fresnel formula,

$$\hat{r}_{\pm} = \frac{\hat{N}_{\pm} - n_0}{\hat{N}_{\pm} + n_0},$$

gives reflectivity for right and left circularly polarized light. The electric field of incident light with the linear polarization whose direction is along the  $x$  axis is written by

$$\begin{aligned} \mathbf{E}_{in} &= E_0 e^{-i\omega t} \mathbf{x} \\ &= E_0 e^{-i\omega t} \frac{\mathbf{r} + \mathbf{l}}{\sqrt{2}}, \end{aligned}$$

where  $\mathbf{r} = (\mathbf{x} + i\mathbf{y}) / \sqrt{2}$  and  $\mathbf{l} = (\mathbf{x} - i\mathbf{y}) / \sqrt{2}$  are the unit vectors of a right and left circularly polarized light, respectively. Thus, the electric field of the reflected light is given by

$$\mathbf{E}_{out} = E_0 e^{i\omega t} \frac{|r_+| e^{i\theta_+} \mathbf{r} + |r_-| e^{i\theta_-} \mathbf{l}}{\sqrt{2}}$$

where  $\hat{r}_+ = |r_+| e^{i\theta_+}$  and  $\hat{r}_- = |r_-| e^{i\theta_-}$  are the Fresnel's reflectance coefficients for a right and left circularly polarized light, respectively. This equation is rewritten using by the unit vectors  $\mathbf{x}$  and  $\mathbf{y}$  as

$$\mathbf{E}_{out} = \frac{E_0}{\sqrt{2}} e^{-i\omega t + i\theta} \left\{ 2 \left( \cos \frac{\Delta\theta}{2} \mathbf{x} - \sin \frac{\Delta\theta}{2} \mathbf{y} \right) + i \frac{\Delta r}{r} \left( \sin \frac{\Delta\theta}{2} \mathbf{x} + \cos \frac{\Delta\theta}{2} \mathbf{y} \right) \right\},$$

where  $r = (|r_+| + |r_-|) / 2$ ,  $\Delta r = |r_+| - |r_-|$ ,  $\theta = (\theta_+ + \theta_-) / 2$  and  $\Delta\theta = \theta_+ - \theta_-$ , respectively. This equation is simplified in other coordinate axes,  $\mathbf{x}'$  and  $\mathbf{y}'$ , which are rotated by  $-\Delta\theta/2$  from the (original) coordinate axes  $\mathbf{x}$  and  $\mathbf{y}$  as follows,

$$\begin{pmatrix} x' \\ y' \end{pmatrix} = \begin{pmatrix} \cos \frac{-\Delta\theta}{2} & \sin \frac{-\Delta\theta}{2} \\ -\sin \frac{-\Delta\theta}{2} & \cos \frac{-\Delta\theta}{2} \end{pmatrix} \begin{pmatrix} x \\ y \end{pmatrix}.$$

Thus the electric field of the reflected light is given by

$$\mathbf{E}_{out} = \frac{E_0}{\sqrt{2}} e^{-i\omega t + i\theta} \left( 2\mathbf{x}' + i \frac{\Delta r}{r} \mathbf{y}' \right).$$

Therefore, the polarization of the reflected light becomes elliptic. The principal axis of this reflected light polarization is rotated by  $\theta_K = -\Delta\theta/2$  from the  $x$  axis and the ellipticity is given by  $\eta_K = (1/2)(\Delta r/r)$ .

Here we introduce the complex Kerr rotation angle  $\Phi_K = \theta_K + i\eta_K$ . It is written by the Kerr rotation angle and ellipticity calculated above as,

$$\begin{aligned}\Phi_K &= -\frac{\Delta\theta}{2} - i\frac{1}{2}\frac{\Delta r}{r} = -i\frac{\Delta\hat{r}}{2\hat{r}} \\ &\sim -i\frac{1}{2}\left(1 + \frac{\Delta\hat{r}}{\hat{r}}\right) \\ &\sim -i\frac{1}{2}\ln\frac{2\hat{r} + \Delta\hat{r}}{2\hat{r} - \Delta\hat{r}} \\ &= i\frac{1}{2}\ln\left(\frac{\hat{r}_-}{\hat{r}_+}\right),\end{aligned}$$

where  $\hat{r} = (\hat{r}_+ + \hat{r}_-)/2$  and  $\Delta\hat{r} = \hat{r}_+ - \hat{r}_-$ , respectively. Then we substitute  $\hat{r}_\pm = (\hat{N}_\pm - n_0)/(\hat{N}_\pm + n_0)$  for the above equation and the complex Kerr rotation is rewritten by

$$\Phi_K \sim \frac{n_0\epsilon_{xy}}{(n_0^2 - \epsilon_{xx})\sqrt{\epsilon_{xx}}}.$$

This shows that the complex Kerr rotation  $\Phi_K$  depends not only on diagonal component  $\epsilon_{xx}$  of the dielectric tensor but also on off-diagonal component  $\epsilon_{xy}$ .

Next, we discuss the frequency dispersion of the Kerr rotation angle and the ellipticity. For simplicity, we consider only a moving electron under the classical treatment. The equation of motion of an electron under the magnetic field  $\mathbf{B}$  and the electric field  $\mathbf{E}$  is given by

$$m\frac{d^2\mathbf{u}}{dt^2} + m\gamma\frac{d\mathbf{u}}{dt} + m\omega_0^2\mathbf{u} = e\left(\mathbf{E} + \mathbf{B} \times \frac{d\mathbf{u}}{dt}\right),$$

where  $\gamma$  is a damping constant and  $\omega_0$  is a resonance frequency. We can calculate the diagonal and off-diagonal components of the dielectric tensor,

$$\begin{aligned}\epsilon_{xx}(\omega) &= 1 - \frac{ne^2}{n\epsilon_0} \frac{\omega^2 + i\omega\gamma - \omega_0^2}{(\omega^2 + i\omega\gamma - \omega_0^2)^2 - \omega^2\omega_c^2}, \\ \epsilon_{xy}(\omega) &= \frac{ne^2}{n\epsilon_0} \frac{-i\omega\omega_c}{(\omega^2 + i\omega\gamma - \omega_0^2)^2 - \omega^2\omega_c^2},\end{aligned}$$

where  $\omega_c = |eB/m|$  denotes the cyclotron frequency of the electron. The functional form of the dielectric tensor is Lorentzian. Figure 2.1 shows the calculated spectra of the Kerr rotation

angle  $\theta_K$  and the ellipticity  $\eta_K$  derived from the dielectric tensor given above. The refractive index  $n$  and the attenuation coefficient  $\kappa$  are also shown in the figure. Since  $\kappa$  corresponds to the absorption coefficient, this result indicates that the peak of the absorption agrees with that of the Kerr rotation angle. The figure shows that the off-diagonal component of the dielectric tensor  $\epsilon_{xy}$  is dominant for the Kerr rotation angle  $\theta_K$ . When the cyclotron frequency increases, which indicates increasing the magnetization (applied magnetic field), the magnitude of  $\epsilon_{xy}$  at the resonance frequency increases linearly without the change of the resonance frequency. Therefore, we can estimate the magnitude of the magnetization owing to the Kerr rotation angle.

### 2.1.3 Photo-induced Kerr Rotation

In zincblende structures, the spin-polarized carriers are excited following on the selection rule of the optical transition (Fig. 2.2 (a)). For example, in case of heavy holes, it is possible to generate a hole with the total angular momentum  $J_x = -3/2$  and an electron with the spin  $s_x = -1/2$  by a right circularly polarized light ( $\sigma^+$ ) with the propagation direction along the  $x$  axis. The magneto-optical effect is caused by this local magnetization, spins of carriers, because the spins behave as the magnetic moments. We call this the photo-induced Kerr effect. Because the direction of the local magnetization is along the direction of the incident light, this magneto-optical Kerr effect becomes polar Kerr effect.

When the external transverse magnetic field was applied parallel to the  $z$  axis (the *Voigt configuration*) and when the propagation direction of the incident light is along the  $x$  axis, the electron spin begins rotational motion in the plane ( $xy$ -plane) around the external magnetic field ( $z$  axis). This is the Larmor precession of an electron spin (Fig. 2.2 (b)). Thus the expectation value of the  $x$  component of the electron spin has the time dependence of

$$\langle S_x \rangle \propto \cos\left(\frac{g\mu_B B}{\hbar} t\right),$$

where  $\mu_B$ ,  $g$  and  $B$  denote the Bohr magneton, the electron  $g$ -factor and the external magnetic field, respectively. As the local magnetization  $M_x$  is proportional to the electron spin  $S_x$ , the

polar Kerr effect is induced by the local magnetization parallel to the direction of the incident light. Since the Kerr rotation angle is proportional to  $M_x$ , the oscillatory signal will be observed. This is the photo-induced Kerr rotation under the transverse magnetic field. We can estimate the g-factor from the period of the observed oscillation. The practical detection method will be shown in the next section in detail.

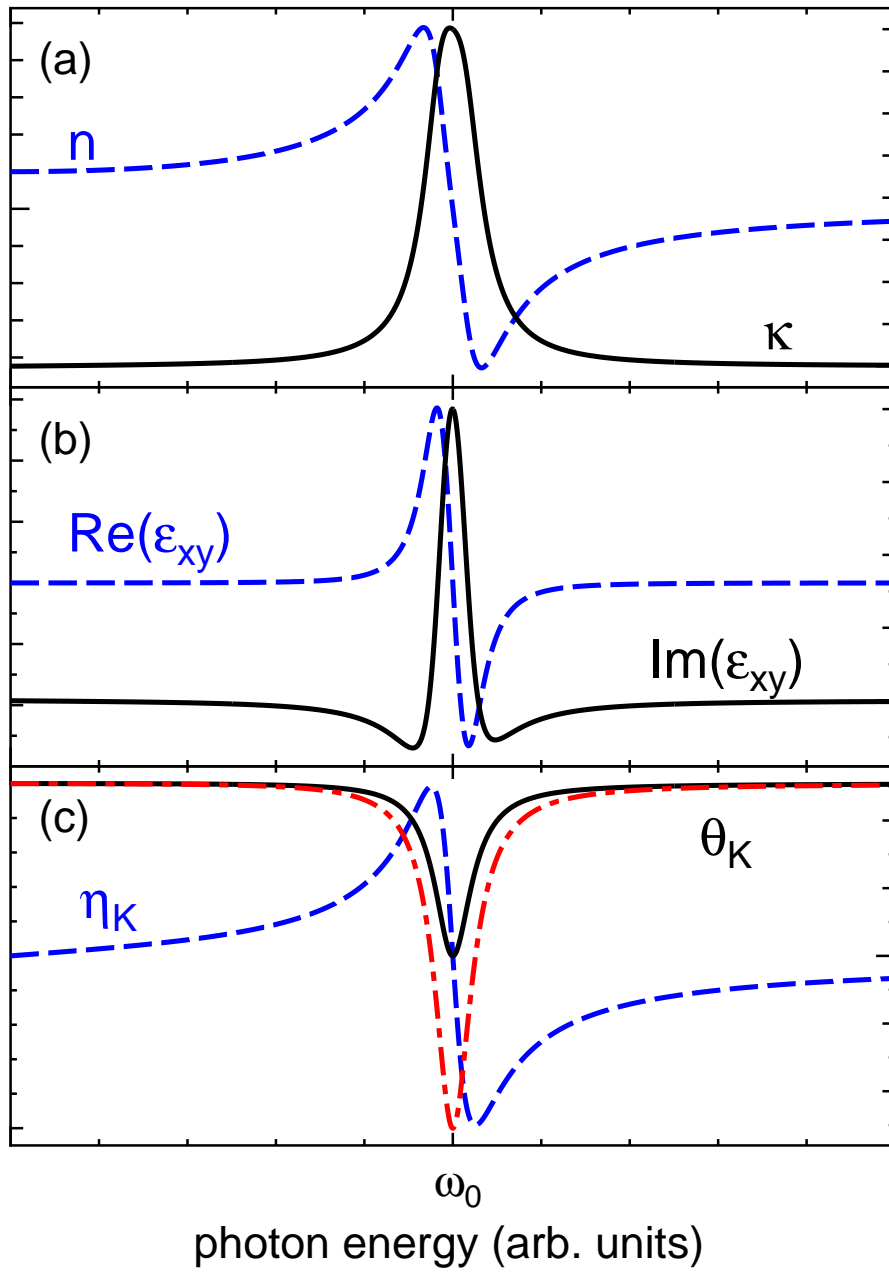


Fig. 2.1 Calculated spectra of (a) a refractive index  $n$  (blue dashed) and an attenuation coefficient  $\kappa$  (black solid), (b) the real part (blue dashed) and the imaginary part (black solid) of the off-diagonal component of the dielectric tensor  $\epsilon_{xy}$  and (c) the Kerr rotation angle  $\theta_K$  (black solid) and the Kerr ellipticity  $\eta_K$  (blue dashed) by classical treatment of a moving electron under magnetic and electric fields. Red dot-dashed line indicates the Kerr rotation angle  $\theta_K$  with the cyclotron frequency which is larger than that of solid line by two times.

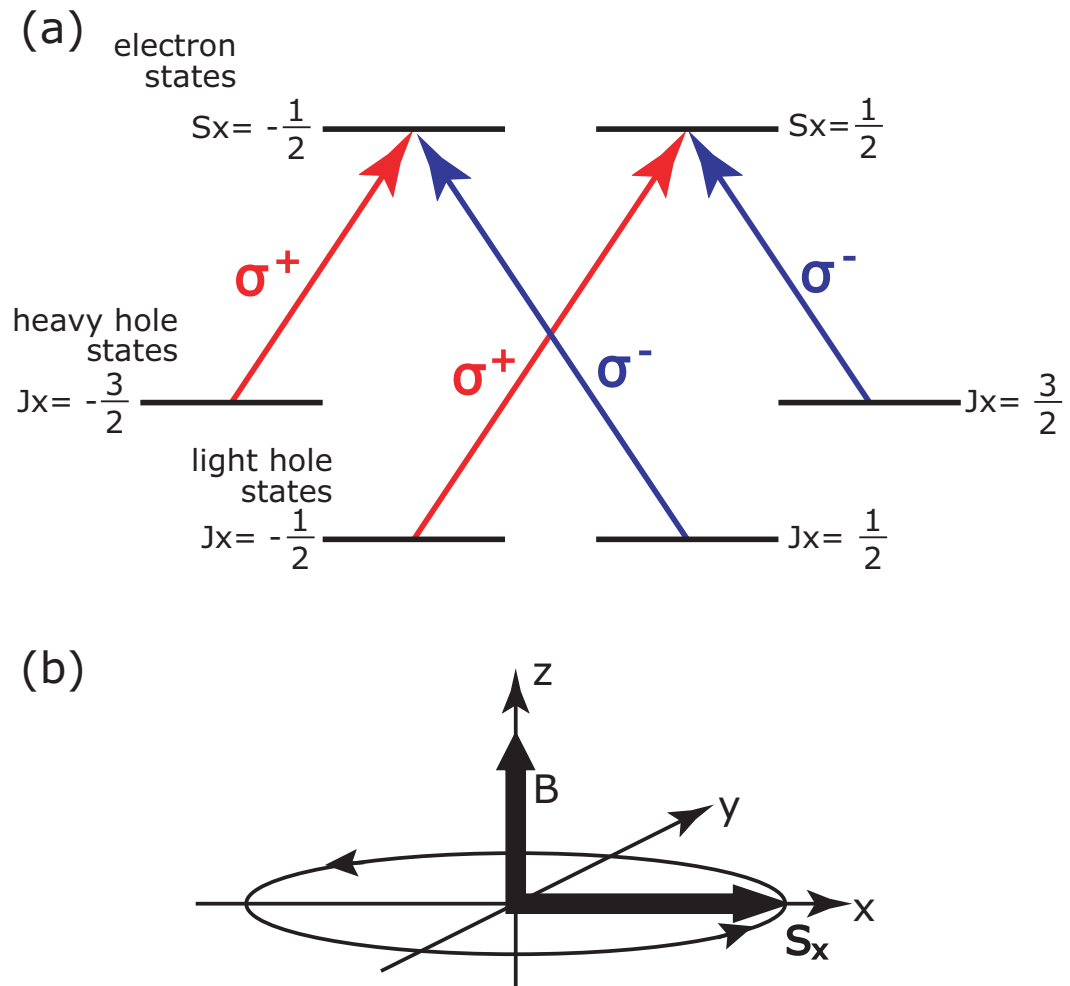


Fig. 2.2 (a) Energy levels of a quantum well in a zincblende structure and the selection rule for the optical transition. (b) Larmor precession of the spin under the transverse magnetic field.

## 2.2 Highly Sensitive Kerr Rotation Detection by Means of a Photoelastic Modulator

For the observation of spin dynamics in single-layer quantum dots, the major experimental method is based on the photoluminescence measurements such as the photoluminescence quantum beat [4–9]. These experiments were performed, however, under the non- (quasi-) resonant excitation. There is few experiment under the resonant excitation, because of the difficulty of measurement. So we constructed highly sensitive detection system of time-resolved Kerr rotation by means of a photoelastic modulator (PEM) [21, 22], an optical bridge with a balanced detector [23] and tandem double lock-in amplifiers. The details are shown in the following.

A PEM is a quartz glass modulator with a piezo-electric transducer oscillator. The oscillator makes an acoustic oscillation in the quartz glass. The resultant birefringence in the quartz glass modulates the optical delay for the cross-linearly polarized light. We can make any polarization of light using a PEM.

At the oscillation frequency  $p$  [rad/s] of the PEM, the retardation is given by  $\delta = (2\pi\Delta l/\lambda) \sin pt = \delta_0 \sin pt$  where  $\Delta l$  and  $\lambda$  are the thickness of a quartz glass and the wavelength of the incident light, respectively. At  $\delta_0 = \pi/2$ , for example, the maximum retardation becomes  $\pi/2$ . This gives circularly polarized light (Fig. 2.3).

When the axis of the polarizer  $P$  is set at 45 degrees from the  $x$  axis in Fig. 2.4, the electric field  $\mathbf{E}_1$  of the light passing through the polarizer is given by

$$\mathbf{E}_1 = \frac{E_0}{\sqrt{2}} (\mathbf{x} + \mathbf{y}) .$$

The electric field  $\mathbf{E}_2$  of the light passing through the PEM has an optical delay  $\delta$  between the  $x$  and  $y$  components,

$$\begin{aligned} \mathbf{E}_2 &= \frac{E_0}{\sqrt{2}} (\mathbf{x} + e^{i\delta} \mathbf{y}) \\ &= \frac{E_0}{\sqrt{2}} ((1 - ie^{i\delta}) \mathbf{r} + (1 + ie^{i\delta}) \mathbf{l}) , \end{aligned}$$

where  $\mathbf{r}$  and  $\mathbf{l}$  are unit vectors of right and left circularly polarized light, respectively.

The electric field of the reflected light from a sample,  $\mathbf{E}_3$ , is written by the use of Fresnel's reflection coefficients  $\hat{r}_+ = |r_+| e^{i\theta_+}$  ( $\hat{r}_- = |r_-| e^{i\theta_-}$ ) for the right (left) circularly polarized light.

$$\begin{aligned}\mathbf{E}_3 &= \frac{E_0}{\sqrt{2}} \left( \hat{r}_+ (1 - ie^{i\delta}) \mathbf{r} + \hat{r}_- (1 + ie^{i\delta}) \mathbf{l} \right) \\ &= \frac{E_0}{\sqrt{2}} \left( (\hat{r}_+ + \hat{r}_-) - i(\hat{r}_+ - \hat{r}_-) e^{i\delta} \right) \mathbf{x} + i \left( (\hat{r}_+ - \hat{r}_-) - i(\hat{r}_+ + \hat{r}_-) e^{i\delta} \right) \mathbf{y}\end{aligned}$$

Therefore the components of the electric field which are divided into the  $x$  and  $y$  components by the analyzer  $A$  are represented by

$$\begin{aligned}E_{3x} &= \frac{E_0}{\sqrt{2}} \left( \hat{r}_+ (1 - ie^{i\delta}) + \hat{r}_- (1 + ie^{i\delta}) \right) \\ E_{3y} &= \frac{E_0}{\sqrt{2}} \left( \hat{r}_+ (1 - ie^{i\delta}) - \hat{r}_- (1 + ie^{i\delta}) \right).\end{aligned}$$

Since the light intensity is proportional to the square of the electric field,  $I \propto |E|^2$ , the difference between the intensities of the  $x$  and  $y$  components is described by

$$\begin{aligned}I &= |E_{3x}|^2 - |E_{3y}|^2 \\ &= 4|r_+||r_-| \sin(\theta_+ - \theta_-) \cos \delta.\end{aligned}$$

As shown in the previous section, the Kerr rotation angle becomes  $\theta_K = -(\theta_+ - \theta_-)/2$ . Thus, this intensity is given by

$$I = 4|r_+||r_-| \sin 2\theta_K \cos \delta.$$

After  $\delta = \delta_0 \sin pt$  is substituted,  $\cos \delta$  is expanded by a series of Bessel's functions. In addition,  $\sin 2\theta_K \approx 2\theta_K$  holds, if  $\theta_K \ll 1$ .

$$\begin{aligned}I &\sim 8|r_+||r_-|\theta_K \cos(\delta_0 \sin pt) \\ &= 8|r_+||r_-|\theta_K (J_0(\delta_0) + 2J_2(\delta_0) \cos 2pt + \dots)\end{aligned}\tag{2.1}$$

This shows that the Kerr rotation angle  $\theta_K$  is determined by the component measurement of  $\cos 2pt$ . Figure 2.3 shows the schematic drawing of this detection method, and the details are discussed below. The polarization axis of light rotates due to the difference of the phases of right

and left circularly polarized light. When this axis is rotated, the  $x$  and  $y$  components oscillate out of phase at the frequency  $2p$ . Therefore, the difference of these components also oscillates at this frequency (Fig. 2.3 (b)). When the polarization of the reflected light from a sample becomes elliptic, the amplitudes of the right and left circularly polarized light are not equal. As the  $x$  and  $y$  components oscillate in phase, the frequency of the sum of the oscillation components becomes  $p$ . The differential signal becomes zero since these components oscillating just in phase are canceled (Fig. 2.3 (c)). Therefore the differential detection system measures only the Kerr rotation angle  $\theta_K$ .

In this work, we used a balanced detector with an optical bridge as the differential detection system. A Wollaston prism as an optical bridge divides the light into the  $x$  and  $y$  components and a differential signal of these components is detected by the balanced detector with high sensitivity.

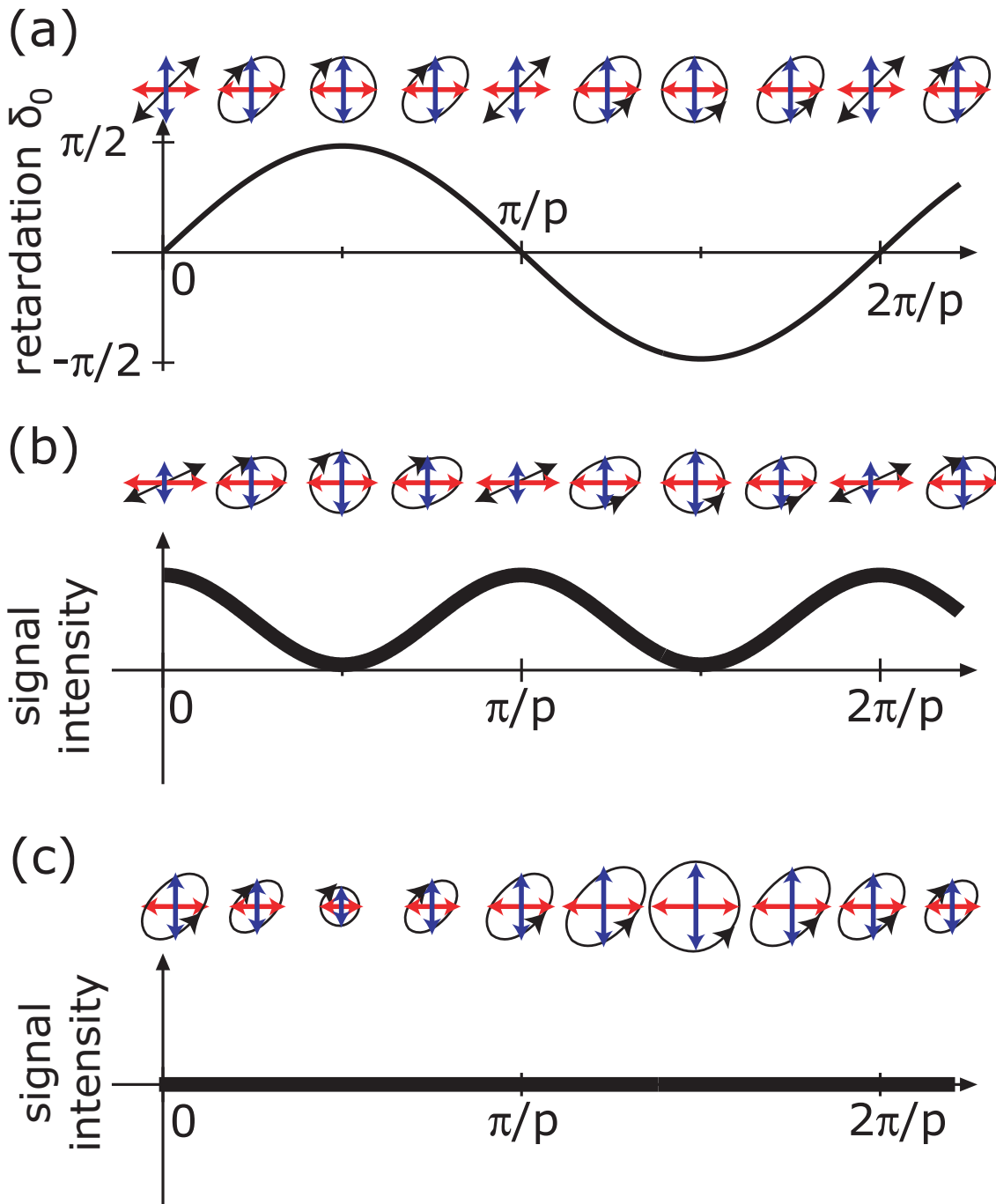


Fig. 2.3 The schematic diagram of the light polarization and the observed signal intensity by the differential detection. (a) The light passing through the PEM driven at the frequency  $p$ . (b) Polarization rotation of the reflected light from the sample passing through the PEM. This signal oscillates at the frequency  $2p$ . (c) When the reflected light polarization becomes elliptic and the principal axis does not change, the differential signal intensity becomes zero. The parallel (red) and perpendicular (blue) components are canceled because they oscillate out of phase by just  $\pi$  radians.

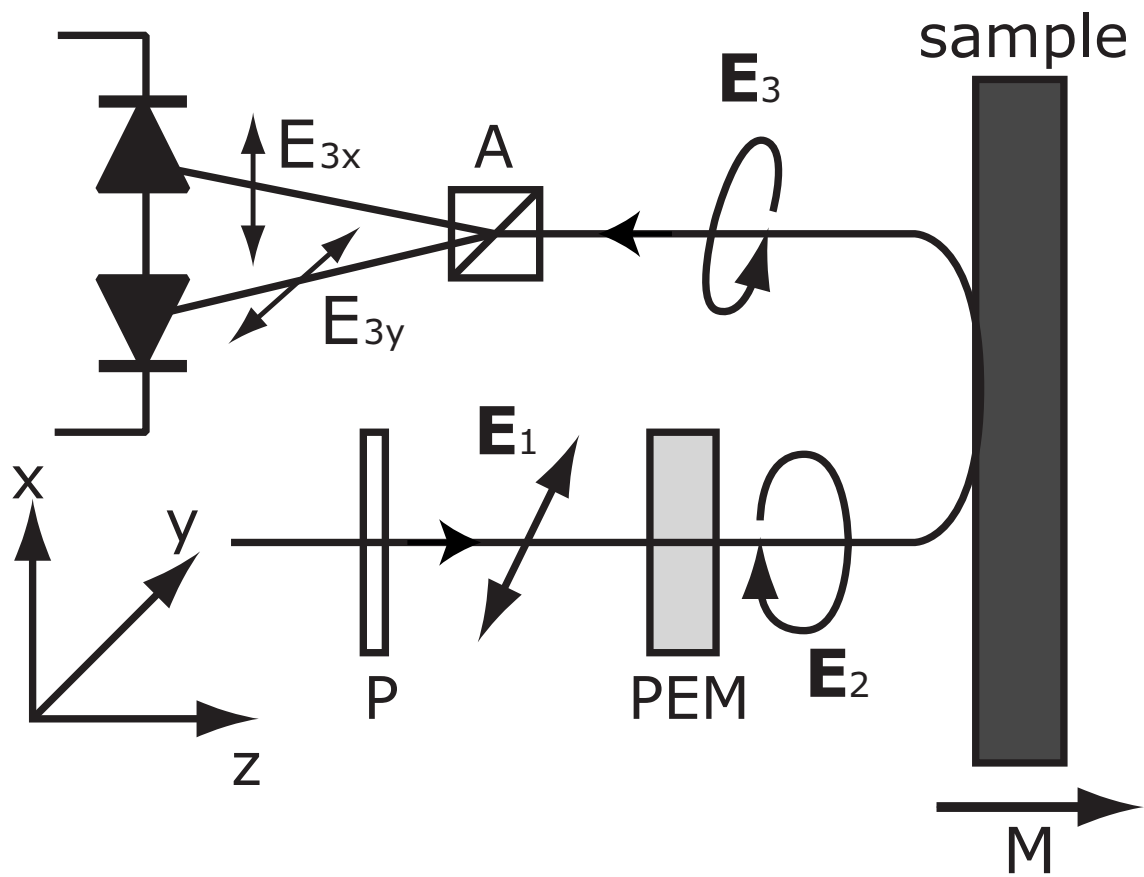


Fig. 2.4 The schematic drawing of the system of the Kerr rotation detection.  $P$  is a polarizer.  $A$  is a Wollaston prism as an analyzer. The differential signal is detected by a balanced detector.

## 2.3 Carrier Spin Dynamics in Semiconductor Nanostructures

Carrier spins in semiconductors relax by spin-related interactions between the carrier spins and the other environments. They are a magnetic interaction between the magnetic momentum of electrons, a spin-orbit interaction between a spin momentum and an angular momentum of the carriers, an exchange interaction between electron and hole spins, and a hyperfine interaction between electron spins and nuclear spins [18,24,25]. The magnetic interaction is caused by the direct dipole-dipole interaction between the magnetic moments of a pair of electrons. If the electrons are separated from each other, this effect is weak, and is negligible. The hyperfine interaction with nuclear spins is the magnetic interaction between the electron spins and the nuclear spins. This mechanism was suggested by Overhauser et al. for the electron localized on donors [26, 27]. The interaction is important when the lattice nuclei have non-zero spin, like GaAs. We omit, however, this effect because the spin relaxation related to the hyperfine interaction was not observed in this work. Therefore, a spin-orbit interaction and an exchange interaction are considered below.

The exchange interaction is caused by the electrostatic Coulomb interaction between carriers. This is spin-dependent phenomena due to the Pauli principle. Hamiltonian for the exchange interaction between two electron spins is described simply by

$$H_{ex} \sim -2Js_i \cdot s_j ,$$

where  $J$  is an exchange integral, and  $s_i$  and  $s_j$  are spin vectors for the two carriers. The spin relaxation mechanism due to the exchange interaction is called Bir-Aronov-Pikus model [18, 19]. The spin relaxation is caused by spin-flip between an electron and a hole due to short-range exchange interaction and long-range (annihilation) interaction. In fact, this exchange interaction is not negligible for p-type GaAs, because of the presence of many holes. The BAP mechanism may play an important role in the nanostructures, such as a quantum well and a quantum dot, because the space limitation makes the distance between an electron and a hole.

Next, we discuss the physical origin of the spin-orbit interaction. A mobile carrier under the

external electric field  $\mathbf{E}$  makes the effective magnetic field  $\mathbf{B} = (\mathbf{v}/c) \times \mathbf{E}$  ( $c$  is the velocity of light). The orbital angular momentum is caused by this magnetic field. Because Hamiltonian of the spin-orbit interaction is described by

$$H_{SO} \sim \lambda \mathbf{s} \cdot \mathbf{l},$$

with the spin momentum  $\mathbf{s}$ , the angular momentum  $\mathbf{l}$  acts on the magnetic (spin) moment of the carrier. Note that any electric and magnetic field, static or alternative, acts on the moving carriers.

The purpose of this thesis is the understanding of the dynamics of photoexcited spin-polarized carriers. Therefore, the process of the spin relaxation of carriers is a matter of great importance. The spin relaxation means disappearance of initial non-equilibrium spin polarization. This is generally understood to be the result of the interaction due to the temporally fluctuated magnetic field. This fluctuation is not *real* magnetic field, but *effective* magnetic field due to the spin-orbit interaction and/or the exchange interaction. This randomly fluctuated magnetic field is characterized by the magnitude  $B_{rms}$  and the correlation time  $\tau_C$ . During this correlation time, the magnetic field is regarded as almost constant. In the following, the precession frequency of carrier spin  $\omega$  is used instead of the magnitude of the magnetic field  $B_{rms}$  because of the relation,  $\omega = g\mu_B B_{rms}/\hbar$ .

The physical image of the spin relaxation is described below: the spin precesses at the frequency  $\omega$  around the direction of the random magnetic field during the correlation time  $\tau_C$ . After the correlation time  $\tau_C$ , the effective magnetic field is changed randomly in the magnitude and the direction. Then the spin starts to precess around a *new* magnetic field. After a number of such steps, the spin forgets completely its initial direction. This is an intuitional physical image of the spin relaxation.

We discuss the non-dimensional value  $\omega\tau_C$  which means the angle change due to the precessional motion during the correlation time. In the usual case,  $\omega\tau_C \ll 1$ , the spin diffusion is slow. The number of random steps during the time  $t$  is represented by  $t/\tau_C$ , and the squared angle change for each step is given by  $(\omega\tau_C)^2$ . Since these steps have no correlation with each

other, the squared angle after the time  $t$  is given by  $(\omega\tau_C)^2 t / \tau_C = \omega^2 \tau_C t$ . The spin relaxation time  $\tau_s$  is defined as the time at which this squared angle becomes the order of unity

$$\tau_s^{-1} \sim \omega^2 \tau_C .$$

Note that the spin relaxation time is much longer than the correlation time, that is  $\tau_s \gg \tau_C$ . In addition, it should be noted that this treatment of spin relaxation is within *classical* consideration, and the Planck constant does not appear in the expression.

In the opposite case,  $\omega\tau_C \gg 1$ , the spin will precess for many cycles during the correlation time. The projection of the spin transverse to the random magnetic field is completely lost during the time of the order of  $1/\omega$ . On the other hand, the spin projection along the direction of the magnetic field is conserved. After the correlation time, however, the direction of the magnetic field will change, and the initial spin memory will disappear. Therefore the spin relaxation time is in the order of the correlation time,  $\tau_s \sim \tau_C$ , in this case.

Next, we consider a spin relaxation for the real structure, especially for the non-centrosymmetric semiconductor such as zincblende structure like GaAs. Hamiltonian of an electron in the conduction band for this structure is written by [18]

$$H = \frac{\hbar^2 k^2}{2m_e^*} + \frac{\hbar}{2} \boldsymbol{\sigma} \cdot \boldsymbol{\Omega}(\mathbf{k}) ,$$

where  $\boldsymbol{\sigma}$  and  $m_e^*$  are Pauli matrix and an effective mass of the electron, respectively.  $\boldsymbol{\Omega}(\mathbf{k})$  is a vector given by

$$\Omega_x(\mathbf{k}) = \alpha \hbar^2 \left( m_e \sqrt{2m_e E_g} \right)^{-1} k_x (k_y^2 - k_z^2) ,$$

and its cyclic permutation of indices  $x, y, z$  for  $\Omega_y$  and  $\Omega_z$ . Note that the vector  $\boldsymbol{\Omega}$  is always perpendicular to quasimomentum  $\mathbf{k}$ . Here the axes  $x, y, z$  are corresponding to the direction along the crystal axes [100], [010], [001], respectively.  $\alpha$  is the non-dimensional value, and  $\alpha = 6 \times 10^{-2}$  for GaAs. Therefore non-centrosymmetric structure leads to split the spin-related conduction bands (see Fig. 2.5). Thus, at the quasimomentum  $\mathbf{k}'$ , there is an energy splitting  $\Delta E$  between *up-spin* and *down-spin* band. This energy splitting causes an effective magnetic field, which depend on the quasimomentum. So the electron spin precesses around this magnetic

field at the frequency  $\Omega$ . For a moving electron, we can understand the effective magnetic field changes its magnitude and direction depending on the quasimomentum  $\mathbf{k}$ . The typical spin relaxation time can, however, be given by  $\tau_S^{-1} \sim \Omega^2 \tau_C$ . This mechanism is called D'yakonov-Perel' (DP) model for structures without the inversion symmetry. The main feature of this model is the existence of the effective magnetic field, which depends on the quasimomentum of a mobile electron. In fact, there are some reports which show that the DP mechanism works in the semiconductor quantum well structure [28,29]. In the exact treatment of the DP mechanism, the spin relaxation rate for an electron in a crystal without the inversion center is given by the expression [18, 30]

$$\frac{1}{\tau_S} = Q\alpha_C^2 \tau_P \frac{(k_B T)^3}{\hbar^2 E_g}, \quad (2.2)$$

where the spin-orbit parameter  $\alpha_C$  is 0.07,  $E_g$  is the band gap and  $\tau_P$  is the momentum relaxation time.  $Q$  depends on the scattering mechanism, and has a value in the order of unity. Note that the spin relaxation rates is proportional not only to  $\tau_P$  but also to  $T^3$ .

In semiconductor quantum dots, the confined electron cannot move due to fully three-dimensional confinement. Thus, the spin relaxation will be suppressed because the DP mechanism does not work even if the crystal structure has the inversion center. In addition, there are calculated results of the spin relaxation of an electron in a GaAs quantum dot by Khaetskii [31–33]. These reports indicate that the spin relaxation time determined from inelastic scatterings, such as phonon scatterings and spin-orbit interaction, becomes much longer than that in a quantum well or other systems at low temperature. Therefore, we can expect the spin relaxation will be suppressed in quantum dot systems.

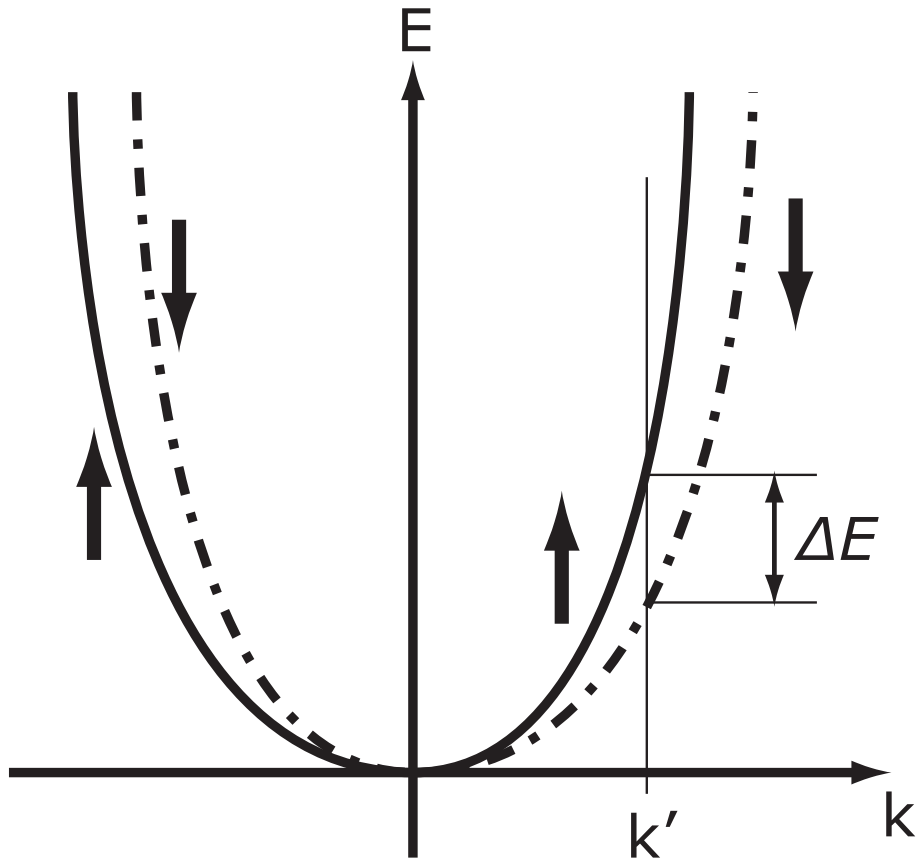


Fig. 2.5 The schematic diagram of the spin splitting of a conduction band in D'yakonov-Perel' model [18, 25]. A solid line shows the band for up-spin electrons, and a dot-dashed line for down-spin ones.  $\Delta E$  is the energy splitting between the up-spin and down-spin bands at the wavevector  $k'$ .

## 2.4 Electronic and Optical Properties

### 2.4.1 Bulk GaAs and InP

Gallium arsenide (GaAs) is a III-V compound semiconductor and forms zincblende structure. The band structure of GaAs is shown in Fig. 2.6 . The energy minimum of the conduction band and the energy maximum of the valence band are located at the center of the Brillouin zone ( $\Gamma$  point). Thus, GaAs has direct band gap structure. The conduction band has a symmetry of  $\Gamma_6$ . The valence bands degenerate into two bands, composed of a doublet  $\Gamma_8$  and a singlet  $\Gamma_7$ . The doublet  $\Gamma_8$  band consists of a heavy hole band with a total angular momentum  $J_z = 3/2$  and a light hole band with  $J_z = 1/2$ . Since the singlet  $\Gamma_7$  is splitted from the doublet  $\Gamma_8$  by a spin-orbit interaction, this band is called a *split-off band*. The energy splitting between  $\Gamma_8$  and  $\Gamma_7$ , spin-orbit splitting energy, is equal to 0.34 eV in GaAs [34].

In GaAs, an exciton can be formed from a  $\Gamma_6$  electron and a  $\Gamma_8$  hole, a distinct exciton absorption is observed near the band gap energy. The exciton energy is 1.519 eV at 2 K. Other properties are shown in Table 2.1. The selection rule of the exciton by a photon is already shown in Fig. 2.2. By tuning the excitation photon energy of and the polarization, spin polarized electrons and holes are generated selectively.

Indium phosphide (InP) also forms the zincblende structure. Therefore, the dominant behavior is similar to that of GaAs. The band structure and optical properties are shown in Fig. 2.7 and Table 2.2.

### 2.4.2 Strain-induced GaAs Quantum Dots

A quantum dot is a system with fully three-dimensional quantum confinement. The confinement gives the system the discrete energy levels like an atom and, therefore, a quantum dot is called an *artificial atom*. Since the size is small, and the ratio of the surface to the volume becomes very large, the interface plays an important role in the system.

To prepare III-V quantum dots, we usually use the Stranski-Krastanov (SK) growth method.

This method utilizes a lattice mismatch between the lattice constants of quantum dot material and matrix material. By this method, it is possible to grow self-assembled quantum dots by molecular beam epitaxy (MBE) or metal organic vapor phase epitaxy (MOVPE) techniques. The SK grown quantum dots may have defects and/or strains in its interface because of the lattice mismatch. Non-radiative recombination centers caused by the strains and defects impair its optical functionalities such as photoluminescence efficiency. To remove these disadvantages, we consider strain-induced quantum dots (SIQDs).

In SIQDs, the confinement consists of two components. One is the vertical confinement in the quantum well and another is the lateral confinement by the strain potential. This strain potential is formed by the quantum dots located on the surface (Fig. 2.8). Since these quantum dots, stressor quantum dots on the surface, introduce the strain into the sample, and by lattice mismatch the strain penetrates into a quantum well layer fabricated near the surface. This local strain forms the potential well in this layer. Thus, carriers in the quantum well are confined by this strain potential. Therefore the *virtual* quantum dots are fabricated in the quantum well layer. The advantages of the SIQDs are the uniformity of thickness along the growth direction and the absence of defects. Especially the energy levels are separated by an equal energy, because the two-dimensional confinement potential formed in the quantum well becomes almost parabolic.

The decrease of the band gap for electrons in SIQDs is understood by using the hydrostatic deformation potential for simplicity. We assume that the stress is applied uniaxially in plane perpendicular to the growth direction. For the case of the GaAs quantum well and the  $\text{Al}_{0.5}\text{Ga}_{0.5}\text{As}$  barrier layers, the deformation potential  $a$  caused by stress on the  $\Gamma$  point is given by

$$a = \frac{dE}{d \ln V} = \frac{dE}{dV/V} \propto -C \frac{dE}{dP},$$

where  $C$  is a positive constant value and  $dE$  is the increase in the energy gap due to the presence of the hydrostatic pressure [35].  $V$  and  $P$  are the volume and pressure of the crystal, respectively. The deformation potential of the conduction band  $a_c$  and the valence band  $a_v$  for the bulk GaAs are -0.710 eV and 1.16 eV, respectively. Since the lattice constants of the bulk GaAs and the

bulk InP are 0.56420 nm and 0.58687 nm, respectively, the tensile stress is applied to the GaAs quantum well below the center of the InP stressor dots. The lattice constant increases laterally when the tensile stress is applied. Then  $dE$  is described by

$$\begin{aligned} dE_c &< 0 && \text{for the conduction band, and} \\ dE_v &> 0 && \text{for the valence band.} \end{aligned}$$

This indicates that the energy interval between the conduction and the valence bands, the energy gap, decreases below the center of the stressor dots. On the other hand, the energy gap increases below the edge of the stressor dots where the quantum well feels compressive stress. Note that there are not only the hydrostatic deformation potential  $\delta E_{hy}$  but also the shear potential  $\delta E_{sh}$ . Due to these potentials, the confinement potentials for an electron and a heavy hole are shifted by stress as [36],

$$\begin{aligned} V_e &= V_e^{QW} - \frac{2}{3}\delta E_{hy} && \text{for electron, and} \\ V_{hh} &= V_{hh}^{QW} + \frac{1}{3}\delta E_{hy} - \frac{1}{2}\delta E_{sh} && \text{for heavy hole,} \end{aligned}$$

where  $V_e^{QW}$  and  $V_{hh}^{QW}$  are the confinement potentials of an electron and heavy hole for the quantum well, respectively. The relation between these strain potentials is given by [37]

$$\frac{\delta E_{hy}}{\delta E_{sh}} \sim 2.18.$$

Therefore, the confinement potential for an electron decreases and that for a heavy hole increases, then the band gap energy for the SIQDs decreases under the stressor quantum dots.

In this work, the SIQDs sample was fabricated by MBE. At first, an  $\text{Al}_{0.3}\text{Ga}_{0.7}\text{As}$  buffer layer was deposited on (100) GaAs substrate. After that a quantum well layer 4 nm thick, an  $\text{Al}_{0.3}\text{Ga}_{0.7}\text{As}$  barrier 14 nm thick and a GaAs cap layer 10 nm thick were deposited in order. SK grown self-assembled InP stressor quantum dots were fabricated on the surface of the cap layer (Fig. 2.9). Since this stressor dots put the local strain into 4 nm QW layer, the SIQDs were fabricated in the QW layer. A surface image of this sample observed by an atomic force microscope is shown in Fig. 2.10. The average diameter, the height and the areal density of stressor dots are about 60 nm, 15 nm and  $4 \times 10^9 \text{ cm}^{-2}$ , respectively. The photoluminescence spectra are shown in Fig. 2.11. The excitation light source is the frequency-doubled output of

a Ti:sapphire laser. At high excitation density, many carriers generated by photons seized the higher energy levels of the SIQDs as observed in the photoluminescence spectra. These energy levels of the SIQDs are seen at equal intervals.

### 2.4.3 Self-assembled InP Quantum Dots

The quantum dots fabricated on the carrier-doped substrate are ionized because doped carriers move and propagate into the quantum dots. This *charged quantum dot* has unique properties. One of them is the observation of a *charged exciton* which consists of an exciton and a doped carrier. The charged exciton has fine energy structures due to the many-body effect. In addition, more complex phenomena about their spin relaxation are observed. It is possible to control charge state of the quantum dots with doped carriers by changing the quantity of the doping to the matrix material. On the other hand, by applying the electric field to the sample, we can control the number of the doped carriers in quantum dots by changing the Fermi level of the system. Recently, there are reports on spin dynamics of number-controlled carriers in quantum dots by means of time-resolved photoluminescence measurements [6–9].

In this work, to investigate carrier spin dynamics in charged quantum dots, we performed TRKR experiments in self-assembled InP quantum dots fabricated by MOVPE. The schematic drawing of this sample structure is shown in Fig. 2.12. First, a GaAs buffer layer was deposited on an n-type GaAs (Si doped) substrate. A layer of self-assembled InP quantum dots is fabricated between  $\text{Ga}_{0.5}\text{In}_{0.5}\text{P}$  barrier layers after the buffer layer is deposited on the n-GaAs substrate. A thin GaAs layer capped the structure. The average diameter, the height and the areal density of the quantum dots are about 40 nm, 5 nm and  $10^{10} \text{ cm}^{-2}$ , respectively. Figure 2.13 shows photoluminescence spectra of this sample. Three peaks attributed to a wetting layer (WL), quantum dots (QDs) and the substrate (bulk GaAs) are clearly observed.

In addition, we prepared another sample with the electrodes. The sample structure was almost the same mentioned above, but the diameter of the quantum dots was smaller, and the

sample was prepared by MBE. The back contact was Au:Ge for the n-GaAs substrate which was prepared by evaporation. Then ohmic contact was made by annealing in hydrogen atmosphere. We prepared ITO (indium tin oxide) on the top surface by sputtering apparatus as a top contact. The photoluminescence spectra depending on the applied bias are shown in Fig. 2.14. The suppression of the photoluminescence with increasing applied bias was clearly observed. This means that the photoexcited electrons are moved from the quantum dots to the substrate with the increase of the negative bias.

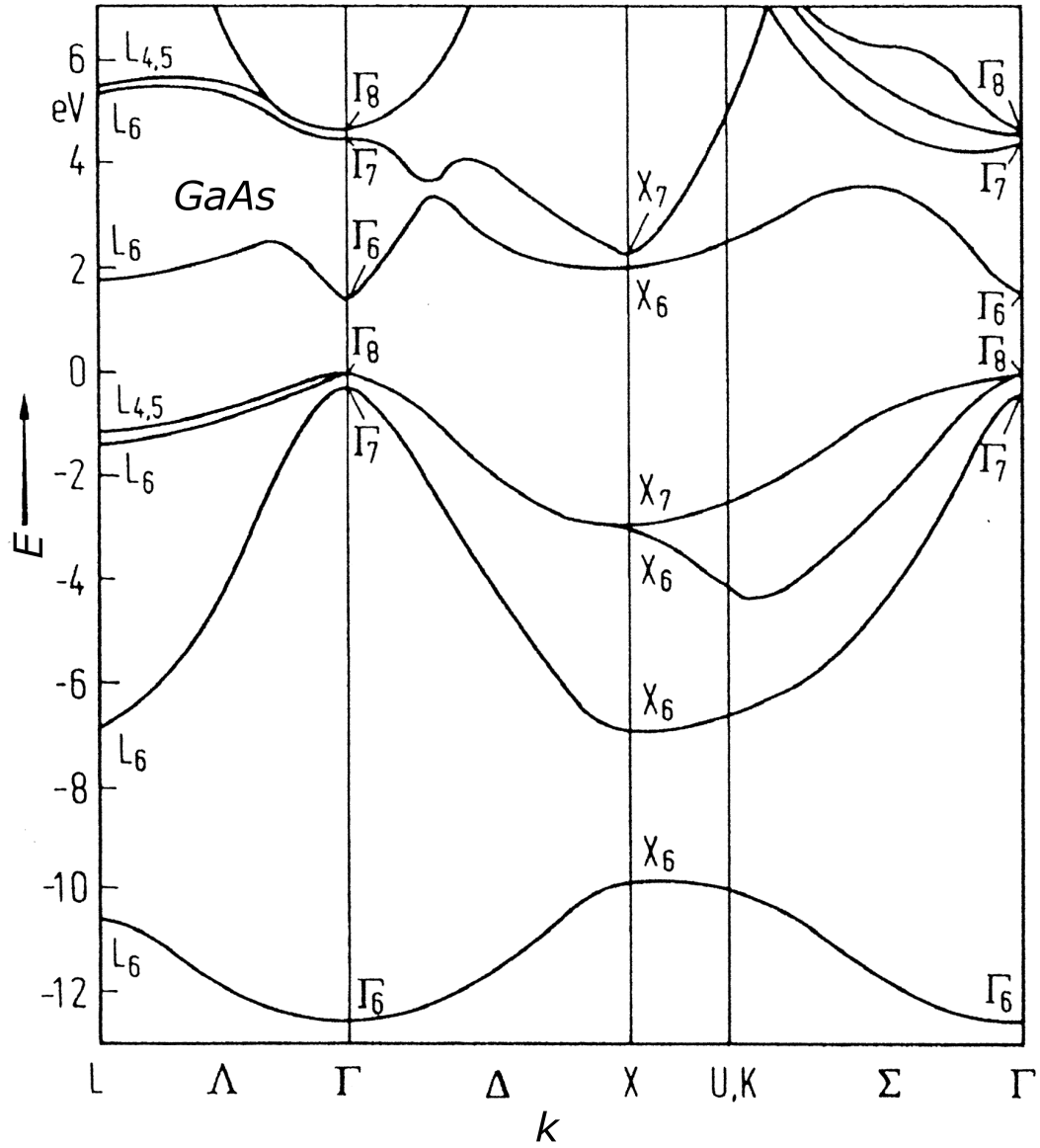


Fig. 2.6 Band structure of GaAs [34]

Band gap energy $E_g$	1.51914 eV (at 0 K)
Spin-orbit splitting energy $\Delta_{SO}$	0.341 eV (at 4.2 K)
Electron g-factor	-0.44

Table 2.1 Optical and electronic properties for GaAs [34, 38]

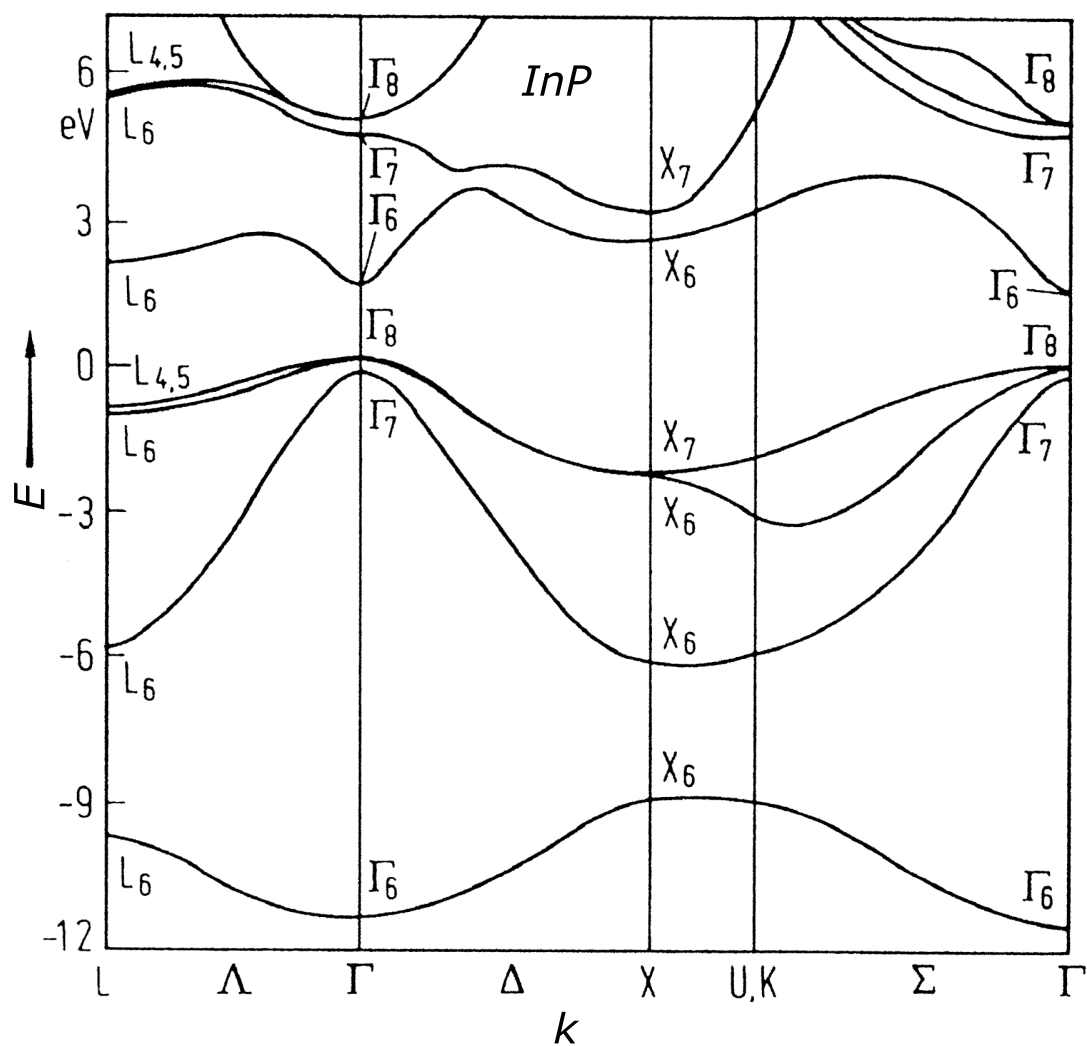


Fig. 2.7 Band structure of InP [34]

Band gap energy $E_g$	1.4236 eV (at 1.6 K)
Spin-orbit splitting energy $\Delta_{SO}$	0.108 eV (at 5 K)
Electron g-factor $g_c$	1.48 (at 4.2 K)
Electron g-factor $g_{SO}$	-1.90

Table 2.2 Optical and electronic properties for InP [34, 38]

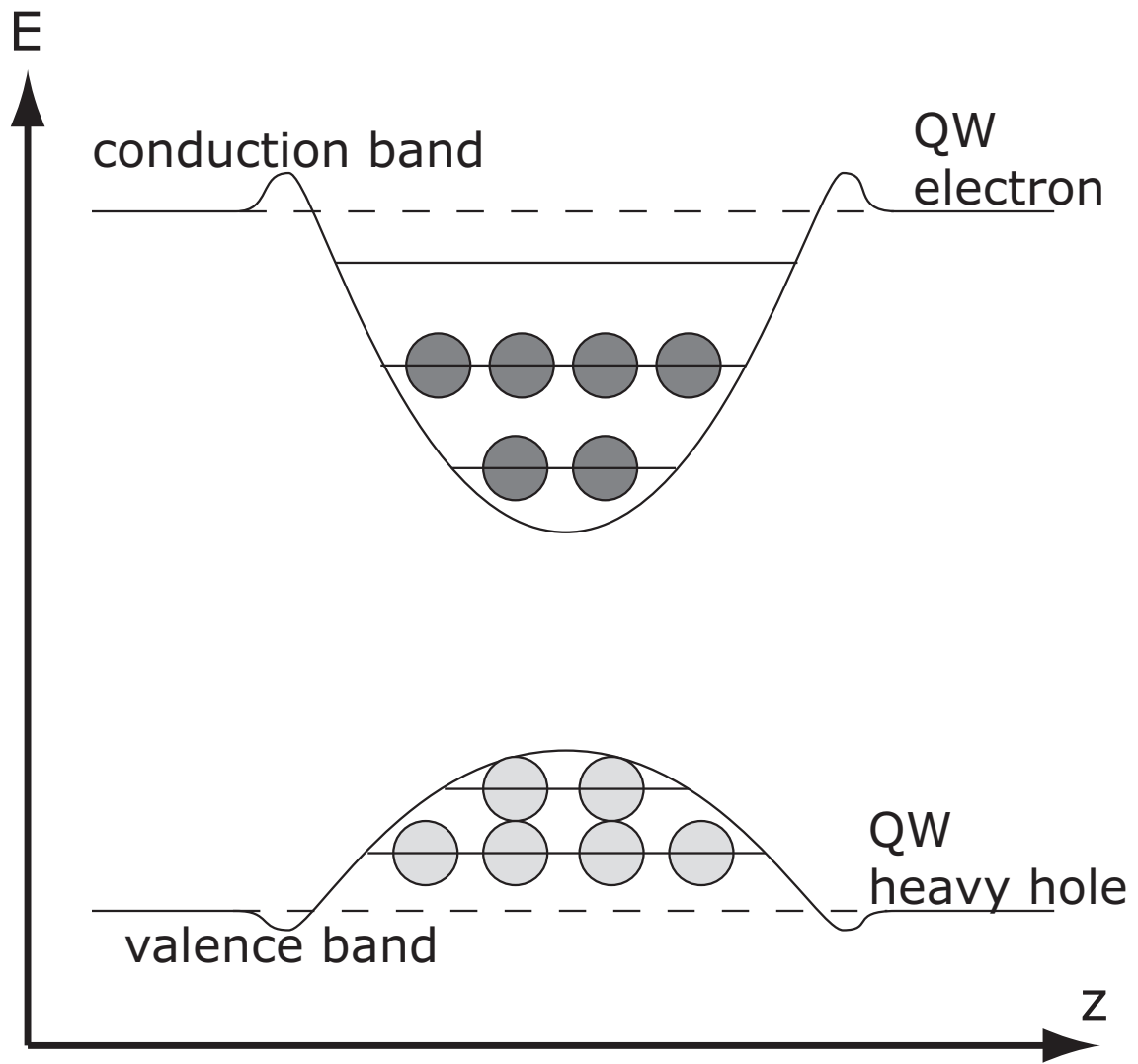


Fig. 2.8 The schematic drawing of the energy potential in GaAs quantum well and strain-induced GaAs quantum dots.

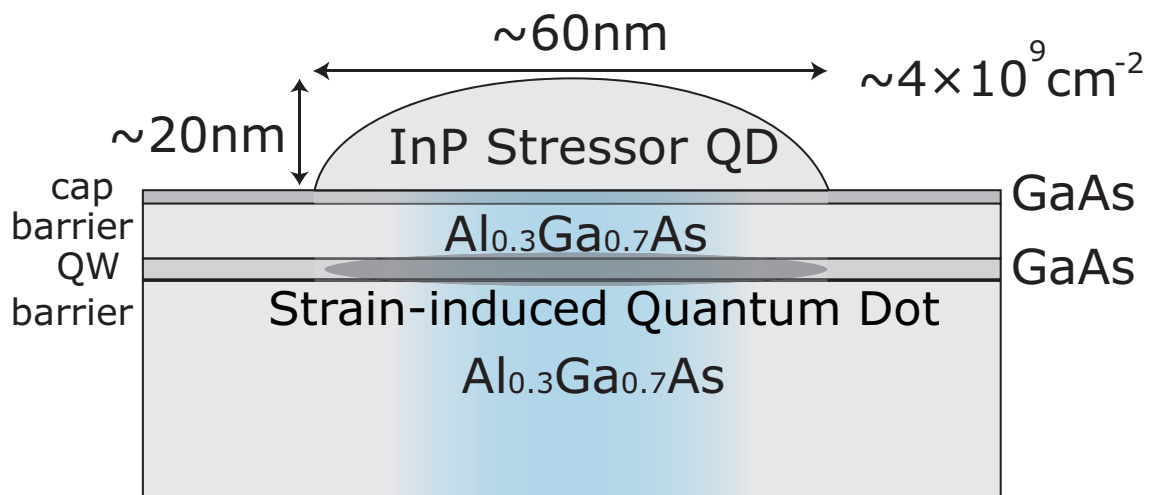


Fig. 2.9 The schematic drawing of the sample in this work. This is the cross sectional drawing.

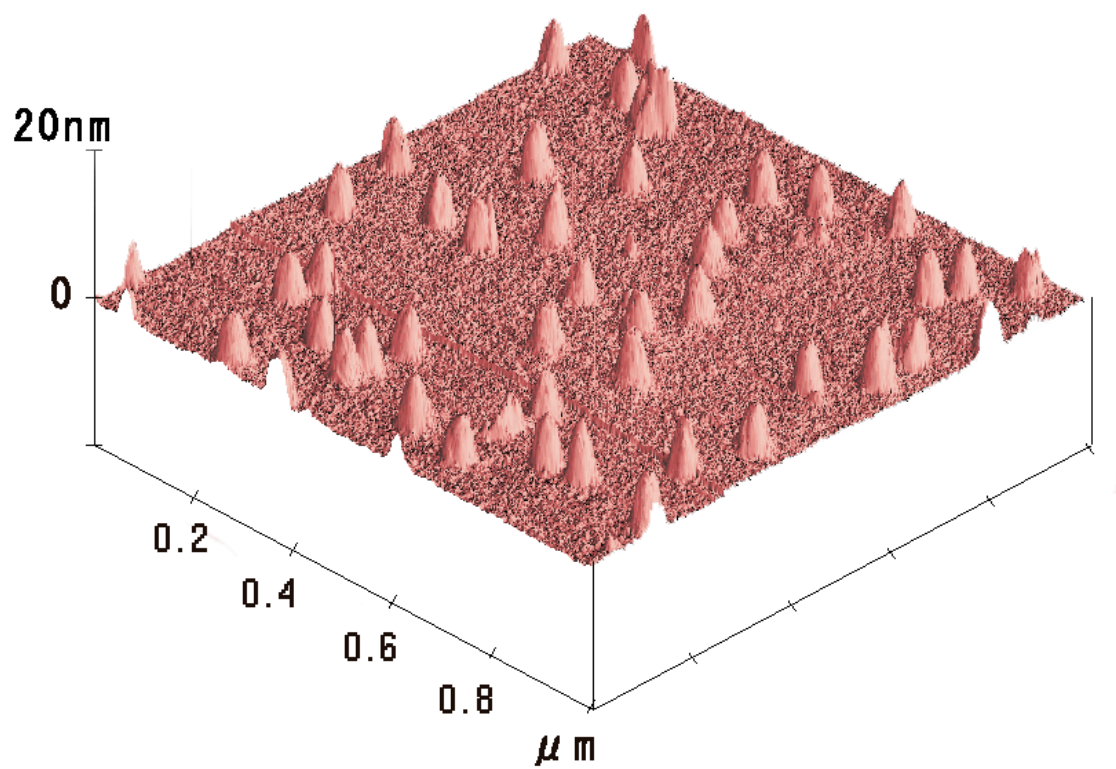


Fig. 2.10 Atomic force microscope image of the InP stressor quantum dots on the GaAs capped surface of the sample.

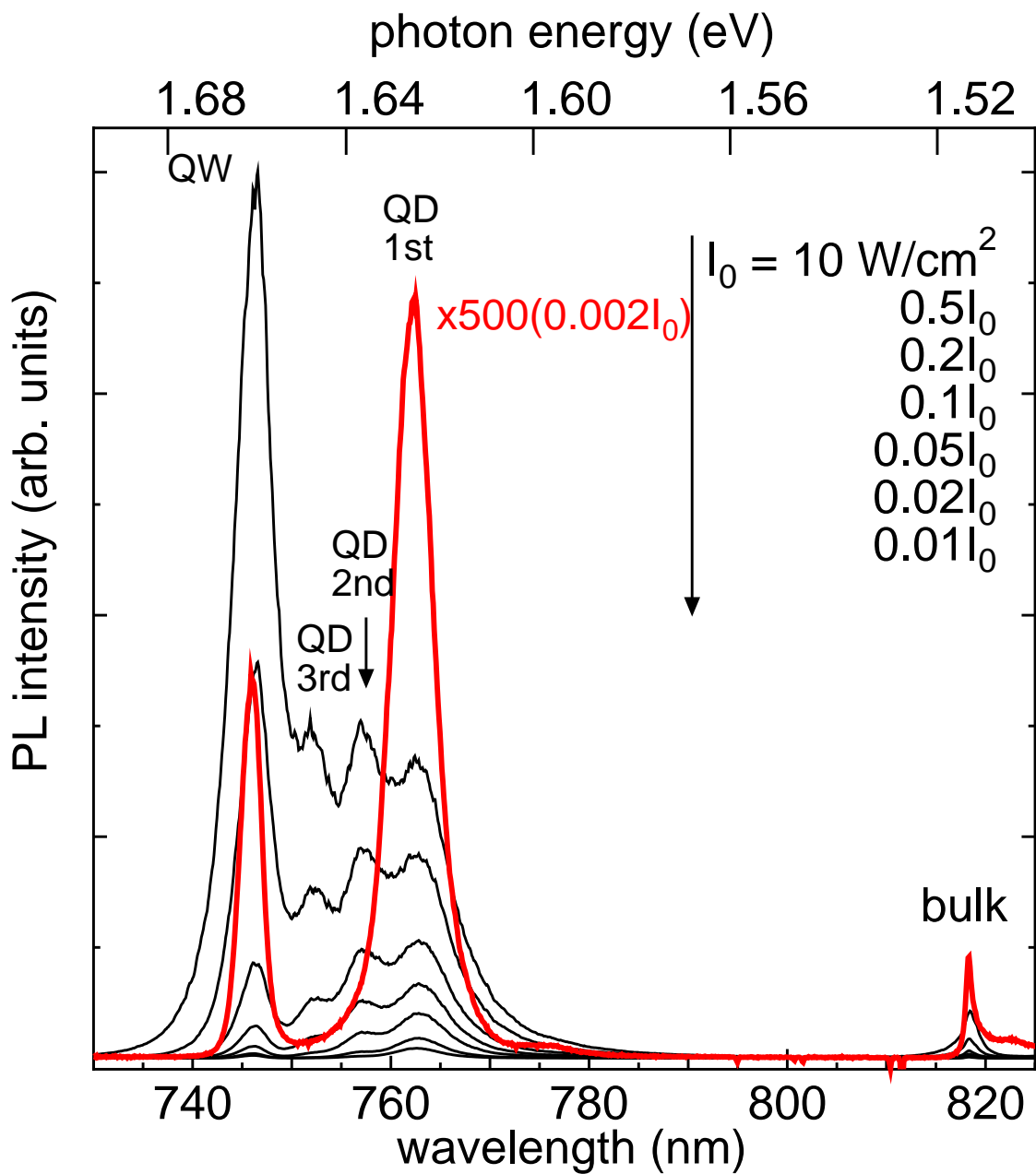


Fig. 2.11 Photoluminescence spectra observed at several excitation powers at  $T = 10 \text{ K}$  and  $B = 0 \text{ T}$ . The excitation light source is the frequency-doubled output of a Ti:sapphire laser. The wavelength is about 400nm

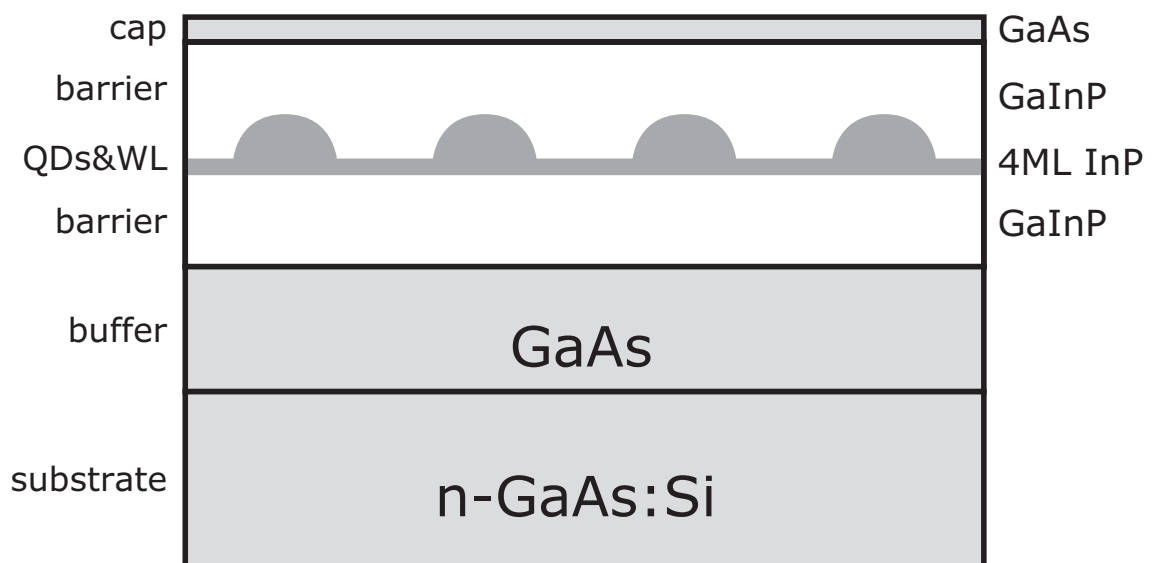


Fig. 2.12 The schematic drawing of self-assembled InP quantum dots sample structure.

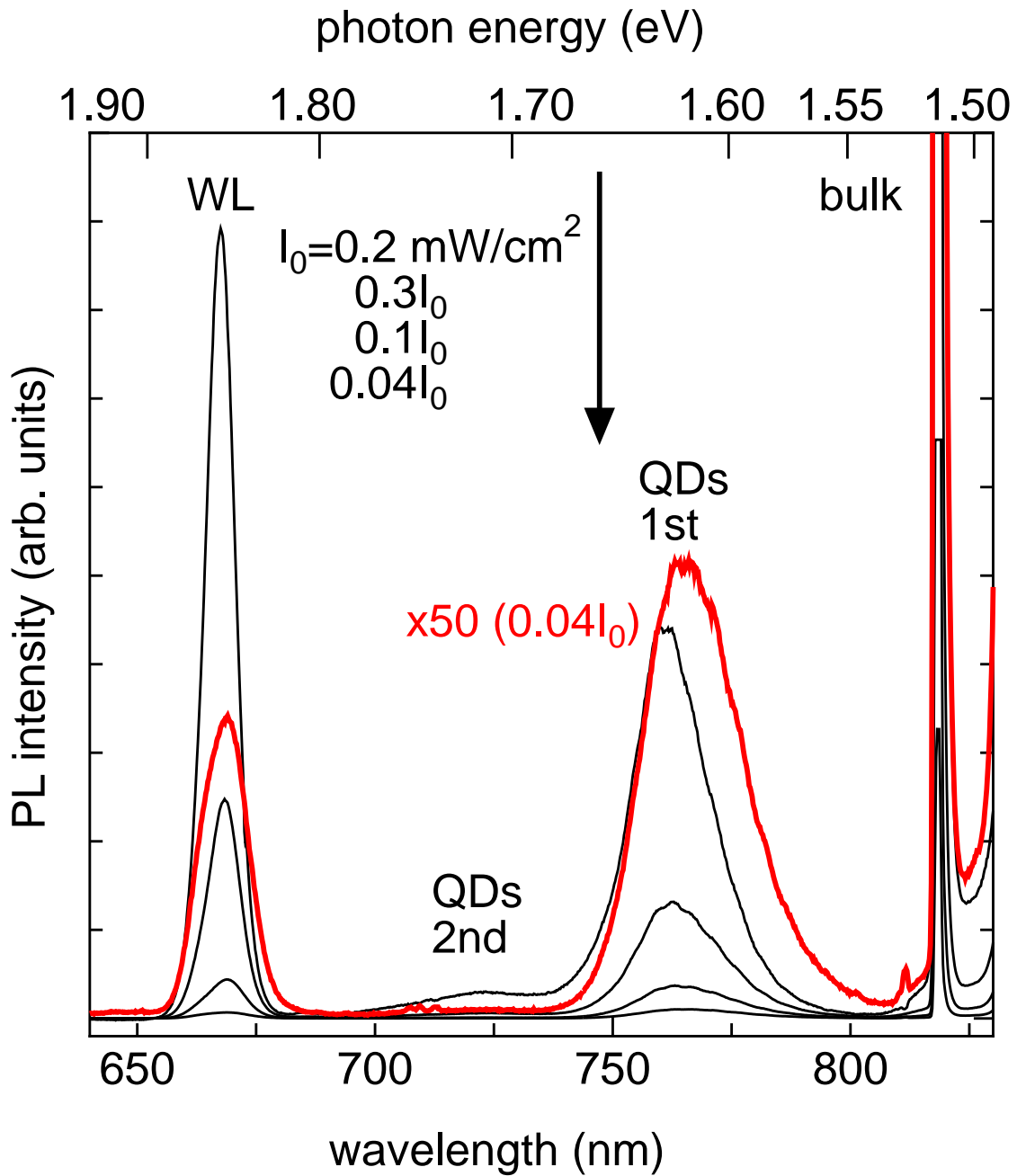


Fig. 2.13 The photoluminescence spectra observed at several excitation powers at  $T = 10 \text{ K}$ . Three peaks are clearly observed. The excitation light source is the frequency-doubled output of a Ti:sapphire laser. The wavelength is about 400nm.

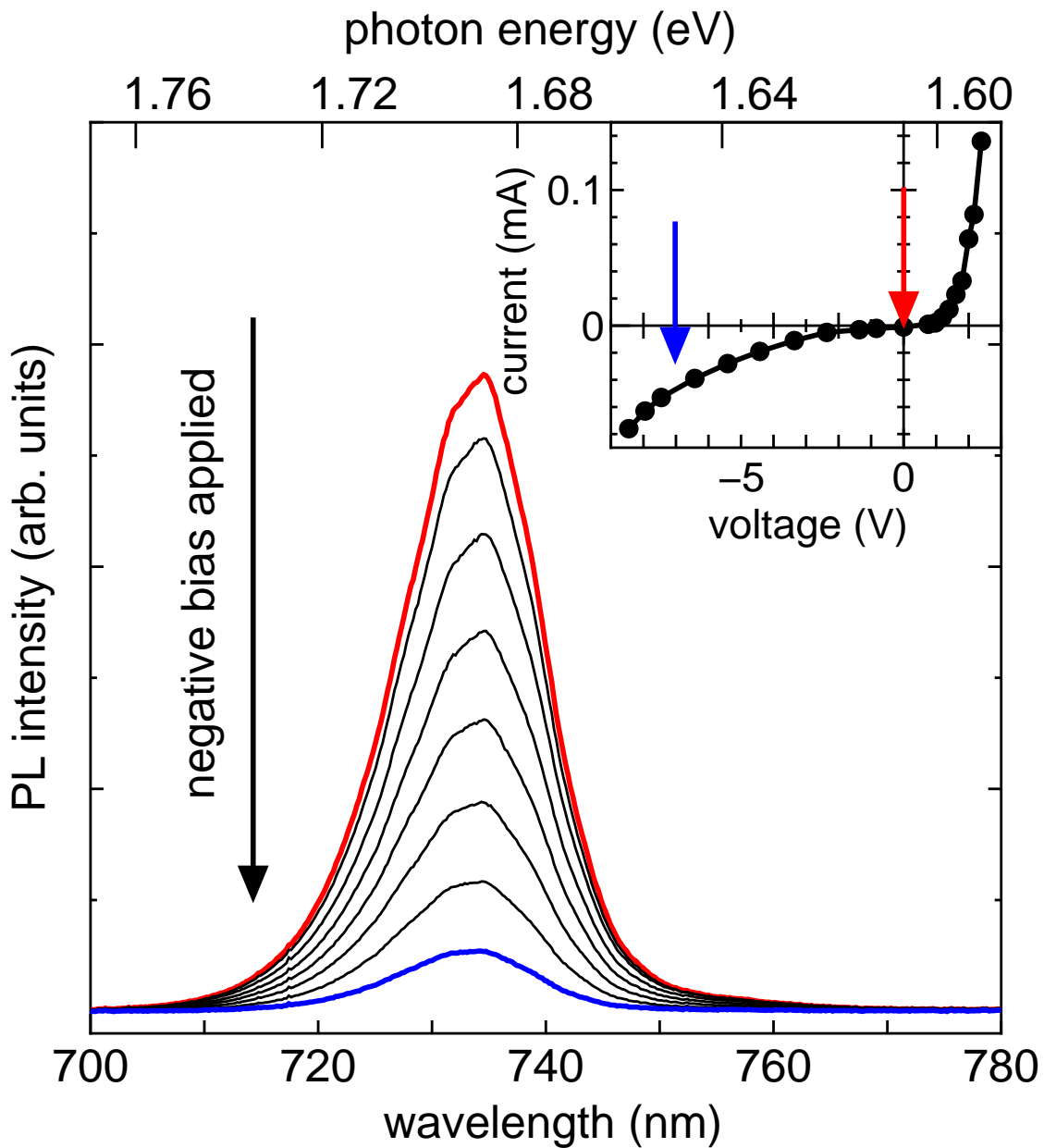


Fig. 2.14 The photoluminescence spectra depending on the negatively applied bias from 0 V to -7 V at  $T = 10$  K. The strongest photoluminescence is for 0 V. The suppression of the photoluminescence is clearly observed with increasing applied bias. Inset: I-V characteristic at room temperature.

# Chapter 3

## Experimental Setup

In this work, two kinds of experiments were performed. One is time-resolved photoluminescence measurement (TRPL) by a streak camera for an InP quantum dots sample. Another is time-resolved Kerr rotation measurement (TRKR). The TRKR system is shown first.

Figure 3.1 shows the experimental system of TRKR. A pump-probe system is used and improved for magneto-optic effect measurement. These improvements are done by means of a photoelastic modulator (PEM), an optical bridge with a balanced detector and tandem double lock-in amplifiers. The highest resolution for the rotation angle measurement of the polarized light around the world is achieved. The details are shown below.

The excitation light source was an energy tunable femtosecond mode-locked Ti:sapphire laser (Maitai; Spectra Physics). The repetition rate and the pulse width were 80 MHz and 80 fs, respectively. One beam splitted by a half mirror was used as the pump one. This was a circularly polarized light passing through a Glan-laser prism and a quarter waveplate. We can change the polarization of light by adjusting the waveplate angle. We usually used right or left circularly polarized light. An optical chopper at the frequency of about 200 Hz modulated the pump beam. Another splitted beam was used as the probe one. The temporally delayed probe beam through an optical delay was spectrally narrowed by passing through a grating to tune the probe energy. After that, the polarization of the probe beam was modulated by PEM (PEM-90; HINDS). These pump and probe beams were focused on the sample in a superconducting magneto-optic cryostat (SM4000; Oxford Instruments) in the transverse magnetic field geometry (Voigt configuration).

The angle between the pump and probe beams was about 3 degrees. It can be considered as the normal incident condition. The reflected light of the probe beam from the sample was passed through a half waveplate and a Wollaston prism and detected by a balanced detector (Nirvana; New Focus). The Wollaston prism worked as an optical bridge and divided the reflected light into two cross-linearly polarized components. The signal from the detector was amplified by a lock-in amplifier (SR830; Stanford Research Systems) at the trigger frequency of 2f mode of PEM (~83 kHz). The output signal of the *first* lock-in amplifier was amplified again by the *second* lock-in amplifier at the chopping frequency to avoid noise caused by the scattered light.

In this system, maximum length of the optical delay was about 100 cm, corresponding to about 3 ns for the time delay. The temporal resolution is about 1 ps which was evaluated by the pump-probe autocorrelation. The spectrally narrowed probe pulse is made by passing through the grating. It is longer than the initial laser pulse width. The sample temperature was varied from 10 to 140 K in the superconducting magneto-optic cryostat, and the applied magnetic field was changed from 0 to 8 T. On the other hand, a glass cryostat and a metal cryostat were used, in case of the absence of the magnetic field, because the sample temperature was more stable in these cryostats. The sample was directly immersed in superfluid helium and the sample temperature was kept at 2 K.

The angle resolution of an optical bridge and a balanced detector is about  $5 \times 10^{-6}$  degrees when the time constant of the second lock-in amplifier was set to be 3 seconds. Figure 3.2 shows the typical data. We compared the obtained angle resolution with those obtained by other groups [12–16], and found that the resolution in our experiment is better than those by 2 to 10 times. The highest angle resolution gave us a great advantage to measure the weak signals.

Figure 3.3 shows the measurement system of the time-resolved photoluminescence to measure carrier dynamics under the quasi-resonant excitation. The excitation light source was an energy-tunable picosecond mode-locked Ti:sapphire laser (Tsunami; Spectra Physics) pumped by LD pumped Nd<sup>3+</sup>:YVO<sub>4</sub> laser (Millenia; Spectra Physics). The repetition rate and the pulse width were 82 MHz and 1 ps, respectively. The pump light was focused on the sample at 2 K

(superfluid helium temperature) in a glass cryostat. Photoluminescence from the sample was collected and focused on an entrance slit of a subtractive-dispersion double monochromator (CT-25CD; JASCO) through two lenses. The focal length of the double monochromator was 25 cm. The wavelength resolution of the monochromator was about 1 nm. The monochromated photoluminescence was detected by a streak camera which consisted of a temporal disperser (C5680; Hamamatsu) and an optical multi-channel analyzer. The temporal resolution of this system was about 30 ps. To observe *pure* carrier dynamics for quantum dots, we performed this experiment under the quasi-resonant excitation. In this experiment, laser illuminated the excited state of InP quantum dots which is higher than the detection energy by the LO phonon energy of bulk InP, that is 43.5 meV. We observed the photoluminescence at 1.62 eV.

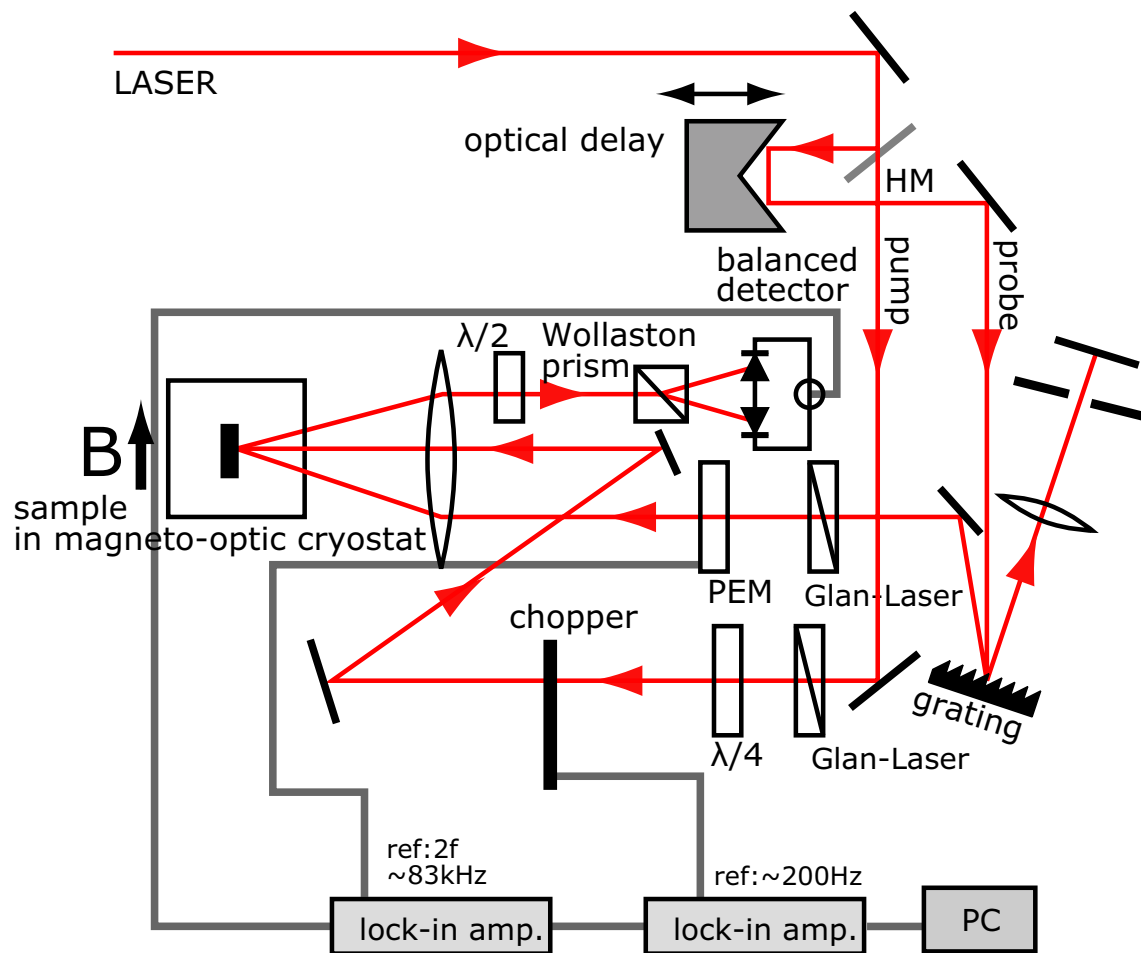


Fig. 3.1 Experimental setup of the time-resolved Kerr rotation experiment. PEM is a photoelastic modulator. The excitation light source is an energy-tunable femtosecond mode-locked Ti:sapphire laser. The detection system consists of a PEM, an optical bridge with a balanced detector and tandem double lock-in amplifiers.

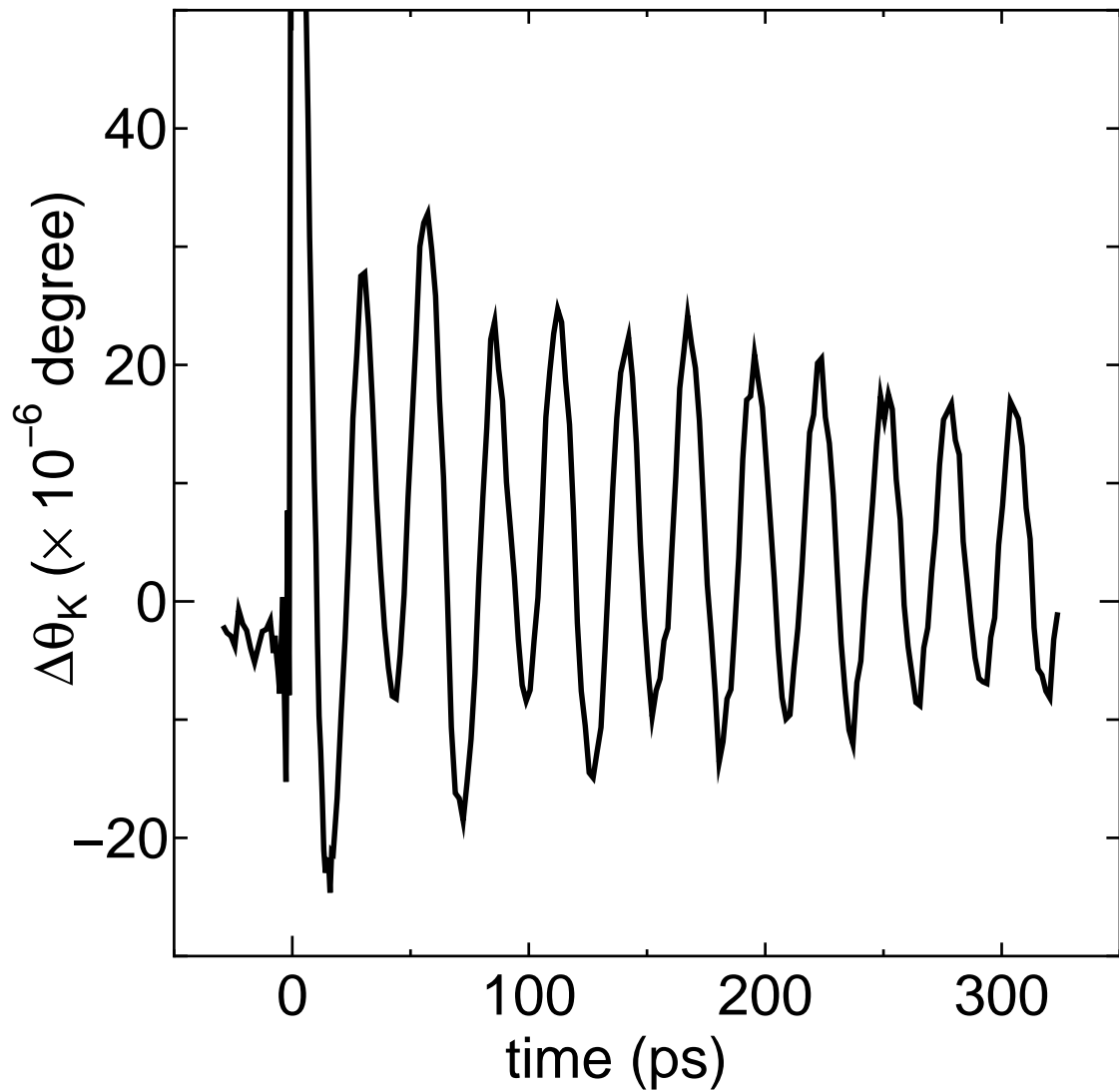


Fig. 3.2 TRKR signal for strain-induced GaAs quantum dots. The angle resolution is about  $5 \times 10^{-6}$  degrees. The time constant of the second lock-in amplifier is set to be 3 seconds.

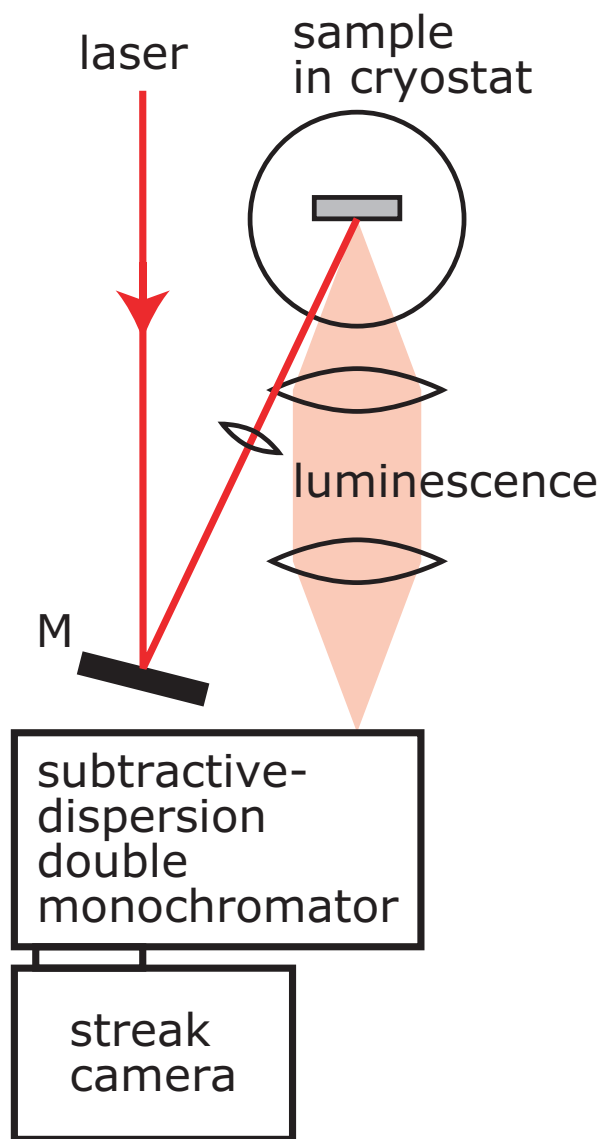


Fig. 3.3 Experimental setup of the time-resolved photoluminescence. The excitation light source is an energy-tunable picosecond mode-locked Ti:sapphire laser. The photoluminescence from the sample is collected by two lenses and focused on the entrance slit of a subtractive-dispersion double monochromator. A streak camera detects the monochromated light.

# Chapter 4

## Results and Discussion

### 4.1 Strain-induced GaAs Quantum Dots

In strain-induced GaAs quantum dots (SIQDs), the TRKR data without a magnetic field is shown in Fig. 4.1. The photoluminescence spectrum is already shown in Fig. 2.11 where the excitation light source is a frequency-doubled output of the Ti:sapphire laser whose wavelength is about 400 nm. The probe energy of TRKR signals for a quantum well (QW) and a SIQDs (QDs) was tuned at 746 nm and 762 nm, respectively. In Fig. 4.1, the TRKR signal for QW is about 20 times larger than that for the QDs. The coverage of stressor InP quantum dots is about 13 % evaluated by the average diameter of dots, 60 nm, and the areal density of dots,  $4 \times 10^9 \text{ cm}^{-2}$ . The ratio of the TRKR signals between the QW and QDs is fairly consistent with the coverage. These signals follow the equation,

$$I(t) \propto e^{-\frac{t}{\tau}},$$

characterized by a relaxation time  $\tau$ . They are fitted well and the observed relaxation times are 194 ps for the QDs, 9 ps for a fast component of the QW and 46 ps for a slow component of the QW, respectively. The decay time for the QDs is longer than that for the QW. This indicates that the spin relaxation time becomes longer due to the reduction of the dimension of system. We must note the high excitation intensity. In this experiment, the pump intensity is varied from 20 to 60 W/cm<sup>2</sup> and the probe intensity is smaller than the pump intensity by about 10 times. If we assume that an absorption coefficient is  $7 \times 10^4 \text{ cm}^{-1}$  (this value is for a bulk GaAs), and the volume of a single quantum dot is  $1.1 \times 10^{-17} \text{ cm}^3$  calculated for a pillar whose diameter

and height are about 60 nm and 4 nm, respectively, the number of the photoexcited carriers in one quantum dot is about one electron-hole pair at  $30 \text{ W/cm}^2$  in each pump pulse. The average distance between photoexcited electron-hole pairs in a quantum well is about 20 nm. This shows the high carrier density for the QW, because 20 nm is comparable with the exciton Bohr radius. We must consider the interactions between carriers such as electron-electron scattering and multiexcitons. Therefore, the decay for the QW consists of two components. As decreasing pump-probe intensities, the decay for the QW became a single exponential decay (not shown). We do not discuss about these high density effect in detail because they are not important in this work. A probe energy dependence of the TRKR signals without a magnetic field is shown in Fig. 4.2. The peak energies of the TRKR signals for the QW and QDs agree with those of the photoluminescence. The calculated frequency dependence of the Kerr rotation signal is already shown in Section 2.2. As is seen in that figure, it has a Lorentzian shape and is similar to the functional form of an attenuation coefficient  $\kappa$ .

The TRKR data for the QW and QDs under the magnetic field  $B = 8 \text{ T}$  are shown in Fig. 4.3. The oscillatory TRKR signals for the QW and QDs are clearly observed when the pump light is either right or left circularly polarized. There is no oscillation for the linearly polarized pump light since linearly polarized light is the equal sum of right and left circularly polarized light. In addition, the oscillations for right and left circularly polarized excitation are out of phase and their phase difference is just 180 degrees. This means that the carriers photoexcited by right and left circularly polarized light have anti-parallel spins to each other. These oscillations are caused by Larmor precessions of the carrier spins generated by the pump light. As mentioned in Section 2.3, the TRKR signals follow the equation,

$$I(t) \propto e^{-\frac{t}{T_2^*}} \cos(\omega t) ,$$

where  $\omega = g\mu_B B/\hbar$  and  $T_2^*$  denote the precession frequency and the spin relaxation time, respectively. The TRKR signal for the QDs has the beat coming from the interference between two components, while that for the QW shows almost single component oscillation. The probe energy dependence of the TRKR signals under the magnetic field  $B = 6 \text{ T}$  is shown in Fig. 4.4.

As is seen in Fig. 4.4 (c), the TRKR signal oscillates even when the probe energy does not correspond to the photoluminescence peak. In addition, the oscillation frequency and the phase are similar to the oscillation signal for the bulk GaAs, which is the substrate of this sample. The oscillation frequency of the damped-oscillatory signal is described by  $\omega = g\mu_B B/\hbar$  where  $g$  is the carrier g-factor. The g-factor is estimated to be about 0.43 from the data in Fig. 4.4 (c). Note that we can get only an absolute value of the carrier g-factor, and there is no information about the sign of it. This value is close to the absolute value of the electron g-factor of a bulk GaAs,  $g = -0.44$ . Thus, we can conclude that these oscillations are originated from the Larmor precession of the photoexcited electron spins in the bulk GaAs under the applied transverse magnetic field. This means that the pump light passing through the barrier layer and QW reaches to the substrate. In fact, because the QW layer was very thin, about 4 nm thick, and because the band gap energy of the barrier layer was larger than the pump light energy, the pump light excites the electrons in the substrate. Thus, the oscillation was observed at the photon energy of 1.61 eV where no photoluminescence peak was observed. The observed TRKR signals may contain the same oscillation signal at all probe energies. Therefore, we must analyze the TRKR signal by the combined oscillation components coming from the QDs, QW and bulk GaAs. So the TRKR signal including the oscillation component from the bulk GaAs is described by

$$I(t) \propto I_0 e^{-\frac{t}{T_{2\text{ GaAs}}^*}} \cos\left(\frac{g_{\text{GaAs}} \mu_B B}{\hbar} t\right) + I'_0 e^{-\frac{t}{T_2^*}} \cos\left(\frac{g \mu_B B}{\hbar} t\right),$$

where  $T_{2\text{ GaAs}}^*$ ,  $T_2^*$ ,  $g_{\text{GaAs}}$  and  $g$  are the spin relaxation time for the bulk GaAs, that for the QDs or QW, electron g-factor for the bulk GaAs and that for the QDs or QW, respectively. We will discuss the component analysis below.

The analysis for the QW signal is shown in Fig. 4.5. Figure 4.5(a) shows the experimental data and a fitting curve. This fitting by two components is in good agreement with the experimental data. The component for the bulk GaAs is shown in Fig. 4.5 (c). This signal oscillates at the frequency of the bulk GaAs and has long spin relaxation time. The long oscillating component is well-fitted with the estimated g-factor  $|g| \sim 0.43$  and the spin relaxation time  $T_{2\text{ GaAs}}^* \sim 363$  ps. This component is smaller than the other components at the initial stage

by about 10 times. The QW component, which is subtraction of the oscillating component of the GaAs substrate from the experimental data, is analyzed in Fig. 4.5 (b). The calculated data fits well the experimental data and gives the g-factor and the spin relaxation time for the QW from the oscillation period of the signal and the decay time of the envelope of the oscillatory signal. These are about  $|g| \sim 0.26$  and  $T_2^* \sim 30$  ps. On the other hand, the component analysis for the QDs is shown in Fig. 4.6. The TRKR signal in Fig. 4.6 (a) shows a beat coming from the interference between two components and is fitted very well by the calculated data. The dominant component is the oscillation from the bulk GaAs which is long lived and oscillates fast. The component for the bulk GaAs is shown in Fig. 4.6 (c). Another component, which is subtraction of the long living GaAs component from the experimental data, is shown in Fig. 4.6 (b). Although this signal is about 3 times smaller than the bulk component, the signal at the different oscillation frequency from the obtained frequency for the bulk GaAs is clearly observed. The g-factor and the spin relaxation time for the QDs are  $|g| \sim 0.22$  and  $T_2^* \sim 91$  ps obtained in the same manner as for the QW. We can compare the obtained spin relaxation times for the QW and QDs,

$$T_2^*(QW) \sim 30 \text{ ps} < T_2^*(QDs) \sim 91 \text{ ps} .$$

This indicates the suppression of the spin relaxation by the additional confinements in QDs. The suppression of the spin relaxation may be caused by the DP mechanism and the BAP mechanism in QDs.

To consider the physical origins of the spin relaxation, we discuss the temperature dependence of the spin relaxation time (Fig. 4.7). First, we discuss it for the QW and bulk GaAs. The spin relaxation rates  $1/\tau_S$  increase quickly at  $T \geq 100$  K. According to the equation (2.2), the spin relaxation rate for the DP mechanism should be proportional to  $T^3\tau_P$ . The momentum relaxation time  $\tau_P$  generally decreases with increasing temperature. The experimentally observed dependence of  $1/\tau_S$  on temperature is expressed by  $1/\tau_S \sim T^{3+n}$  when  $n$  varies with temperature. Here,  $n$  may be caused by the electron scattering by impurities etc. It is considered that the spin relaxation for the QW and bulk GaAs are dominated by the DP mechanism

at  $T \geq 100$  K. At  $T \leq 100$  K, the DP mechanism no longer explains the experimental data. The spin relaxation rate for the QDs also shows the similar behavior, and all spin relaxation rates are almost constant. Because electrons are localized at low temperature, the spin relaxation may be caused by other mechanisms such as exchange interaction with localized holes. It is the BAP mechanism. Especially, in the QDs and QW, the distance between an electron and hole generated by a photon is very short because of the reduction in the exciton Bohr radius. Therefore, the spin relaxations at low temperature for the nanostructures are not due to the DP mechanism but due to the BAP mechanism. Another evidence of the BAP mechanism is described below. The spin relaxation time for the bulk GaAs is longer than those for GaAs nanostructure at low temperature. The relation between the spin relaxation times may suggest that the dominant mechanism of the spin relaxations for the nanostructures is the BAP mechanism. On the other hand, the spin relaxation rate for the QDs increases at  $T \geq 80$  K. Note that the photoluminescence decreases with increasing temperature (Fig. 4.8). The observed spin relaxation time  $\tau_S$  is given by  $1/\tau_S = 1/T_1 + 1/T_2$ . Then  $\tau$  is limited by the energy relaxation time  $T_1$  in principle. Here the energy relaxation time  $T_1$  is given by

$$\frac{1}{T_1} = \frac{1}{\tau_r} + \frac{1}{\tau_{nr}},$$

where  $\tau_r$  and  $\tau_{nr}$  are the radiative and nonradiative lifetimes of the carriers. We assume that the quantum efficiency  $\eta$  of the PL intensity is given by

$$\eta(T) = \frac{1/\tau_r(T)}{1/\tau_r(T) + 1/\tau_{nr}(T)},$$

which depends on the temperature. Figure 4.9 shows the temperature dependence of  $1/\tau_S$  and  $1/\eta$  for the QW and QDs are presented in Fig. 4.7 and Fig. 4.8. We take notice of the behavior of these dependence for the QDs and QW. For the QDs,  $1/\eta(T)$  increases quickly at  $T = 80$  K. This indicates that the nonradiative rate  $1/\tau_{nr}(T)$  also increases and affects predominantly for the relaxation time  $T_1$ . Gotoh et al. and Okuno et al. showed the temperature dependence of the radiative lifetime for QDs [39, 40]. The results showed that unlike the case of QW, in QDs the radiative lifetime does not have a significant temperature dependence. Citrin calculated the tem-

perature dependence of the radiative lifetime for a quantum well, and found that the radiative lifetime is proportional to the temperature  $T$  [41]. The observed spin relaxation rate  $1/\tau_S$  increases with increasing the nonradiative rate  $1/\tau_{nr}(T)$  because the spin relaxation time depends on the energy relaxation time  $T_1$ . Therefore the nonradiative lifetime plays an important role in the spin relaxation time. At  $T < 80$  K, however, the spin relaxation rate is independent on the temperature, and the nonradiative lifetime is not significant. In fact, the radiative lifetime was found to be about 500 ps at  $T = 2$  K, and the long radiative lifetime is consistent with another result [17]. The observed spin relaxation time is given by

$$\begin{aligned}\tau_S &< T_1 && \text{at low temperature, and} \\ \tau_S &\sim T_1 && \text{at high temperature.}\end{aligned}$$

The spin relaxation time  $\tau_S$  is rewritten by  $\tau_S \sim T_2$  at the low temperature. Therefore the spin relaxation is dominated by the BAP mechanism in the low temperature regime. On the other hand, at the high temperature regime,  $\tau_S$  is limited by the carrier lifetime  $T_1$ . Therefore two kinds of processes are considered to govern the observed spin relaxation for the QDs, one is the BAP mechanism at  $T < 80$  K and another is nonradiative decay of electrons at  $T > 80$  K.

For the QW, we can find a dip in the spin relaxation rate at about 80 K, and the dip of the photoluminescence is also seen at the same temperature. Citrin showed the temperature dependence mentioned above. This indicates that the carriers move into the QW beyond the potential barrier of the QDs by the thermal activation. In fact, we can find increasing the photoluminescence intensity from the excited state of the QDs above this temperature. Thus the number of carriers increases, and then, the photoluminescence intensity increases. Therefore  $1/\tau_{nr}(T)$  decreases, and the radiative rate  $1/\tau_r(T) \propto 1/T$  plays a dominant role in the temperature dependence of the spin relaxation time and the photoluminescence intensity. For further discussion about the temperature dependence of the relaxation times, the time-resolved photoluminescence measurement at several temperatures is needed.

We performed the TRKR experiments under several magnetic fields to estimate the g-factor. The results are shown in Fig. 4.10. All of the evaluated splitting energies ( $\Delta E = g\mu_B B$ ) for the QW, QDs and bulk GaAs show linear relationships with applied magnetic field. This indicates

that the observed oscillation signals come from the electron Larmor precession. From the observed splitting energy, the absolute values of the g-factors for the QW, QDs and bulk GaAs are evaluated to be about 0.26, 0.22 and 0.43, respectively. Now we will discuss the evaluated g-factor for the QW. In the Voigt configuration, the direction of the external magnetic field is perpendicular to the direction of the incident and reflected light. Therefore, the carrier spins generated by the incident light precess in plane with the incident (reflected) light. The g-factor of the QW is anisotropic and the g-factor tensor can be represented by two components,  $g_{\perp}$  for perpendicular component to growth direction and  $g_{\parallel}$  for parallel component to growth direction. The Zeeman splitting between the energy levels of the spins depends on the direction and magnitude of the external magnetic field. In a case of Voigt configuration, the Zeeman splitting is caused by the magnetic field perpendicular to the growth direction. Thus the observed g-factor is the perpendicular component to the growth direction  $g_{\perp}$ . So the observed g-factor for QW is  $|g_{\perp}| \sim 0.26$ .

Now we compare the observed g-factors with the results of the photoluminescence quantum beat measurement [17] (Fig. 4.11). It is, however, difficult to compare directly those data because the used samples are slightly different. The main difference is the average size of stressor dots on the surface of sample and the depth of the QW layer from the surface. The average size is about 60 nm for this work and is about 90 nm for the quantum beat measurements. In addition, the QW layer locates deeper for this work. Therefore, carriers feel shallower confinement potential in this work than in the other. Although there are some differences in the sample, the relation between the g-factor for the QDs and the perpendicular component of g-factor for the QW is consistent with the each other. The calculated results in the Kane model by Ivchenko are also shown in Fig. 4.11 [42]. The observed  $g_{\perp}$  for the QW is in good agreement with the calculated result. The strain from the surface is weak so that the obtained g-factor for the studied the QW layer is similar to that of the unstrained quantum well so far reported.

Consequently, we could observe the electron spin relaxation in single-layer quantum dots under the resonant condition by means of newly developed highly sensitive detection system.

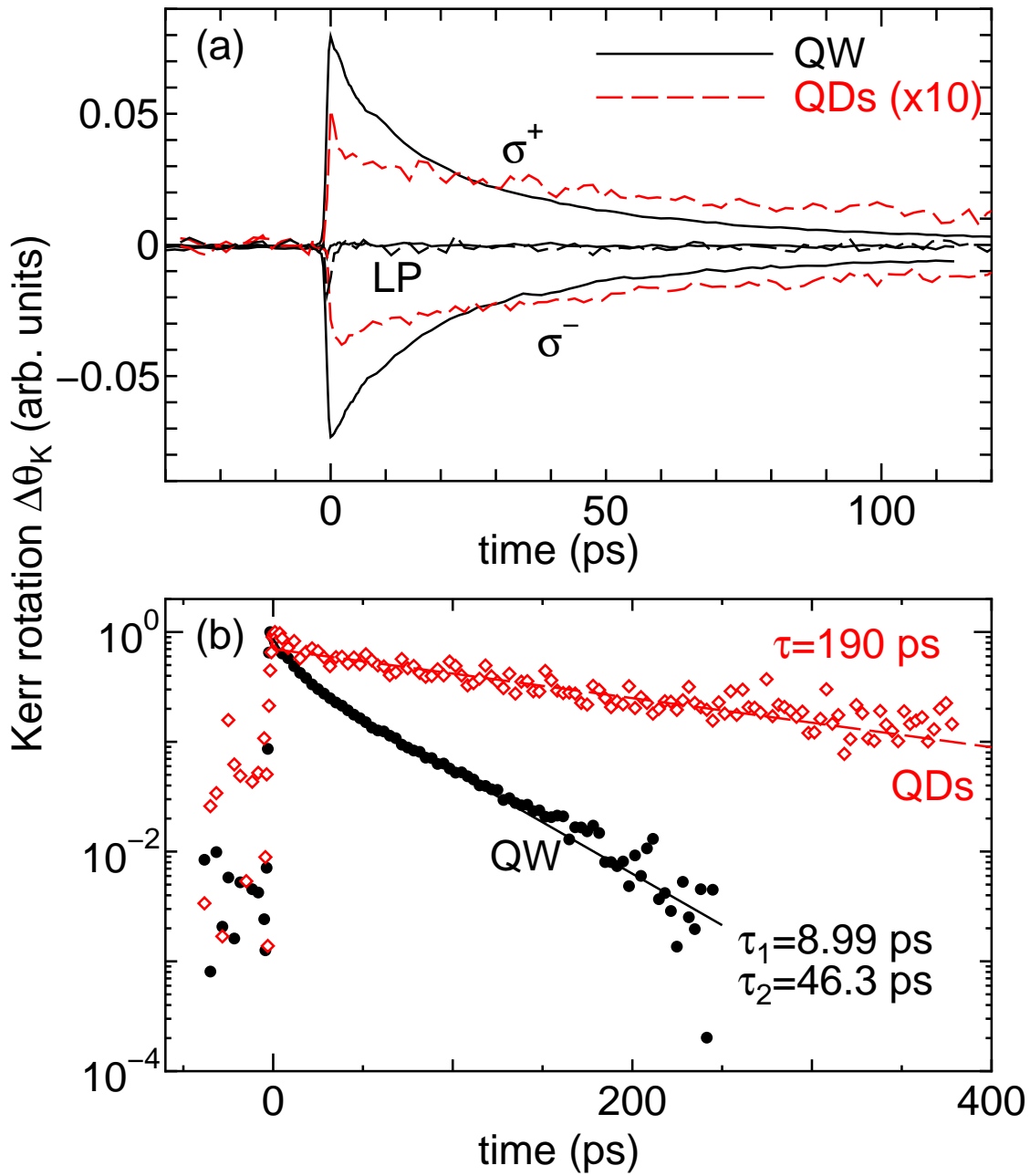


Fig. 4.1 TRKR signals without a magnetic field at  $T = 2$  K. (a) TRKR signals for quantum well (746 nm; solid line) and quantum dots (762 nm; dashed line) for a right circular ( $\sigma^+$ ), a left circular ( $\sigma^-$ ) and a linear polarization (LP) excitation. (b) Logarithmic plots of TRKR signal for quantum well (closed diamonds) and quantum dots (open circles). The solid lines are fitting ones by an exponential decay  $I \propto e^{-t/\tau}$ .

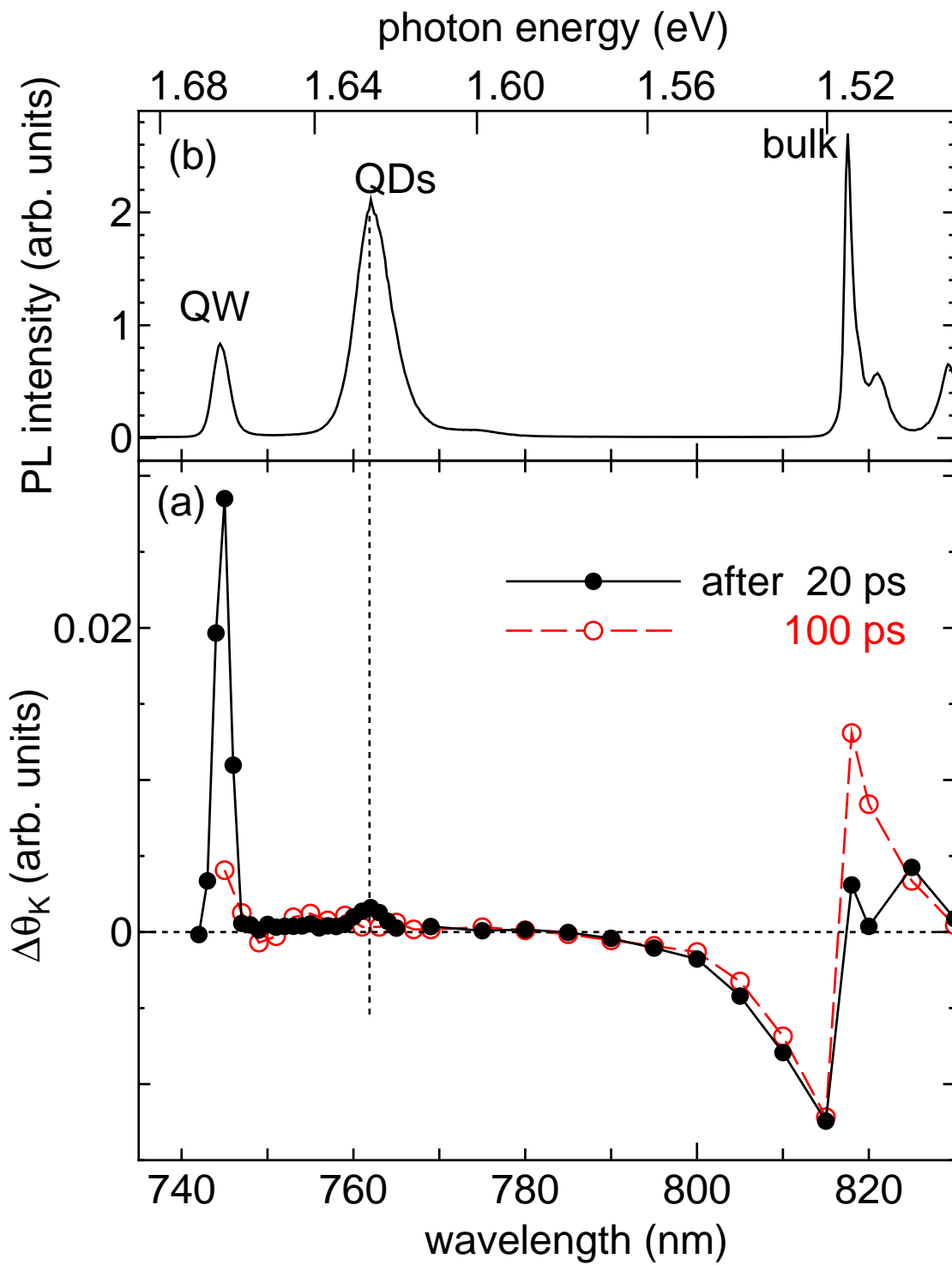


Fig. 4.2 (a) Wavelength dependence of TRKR signal at 20 ps (closed circles) and 100 ps (open circles). (b) Photoluminescence spectrum.

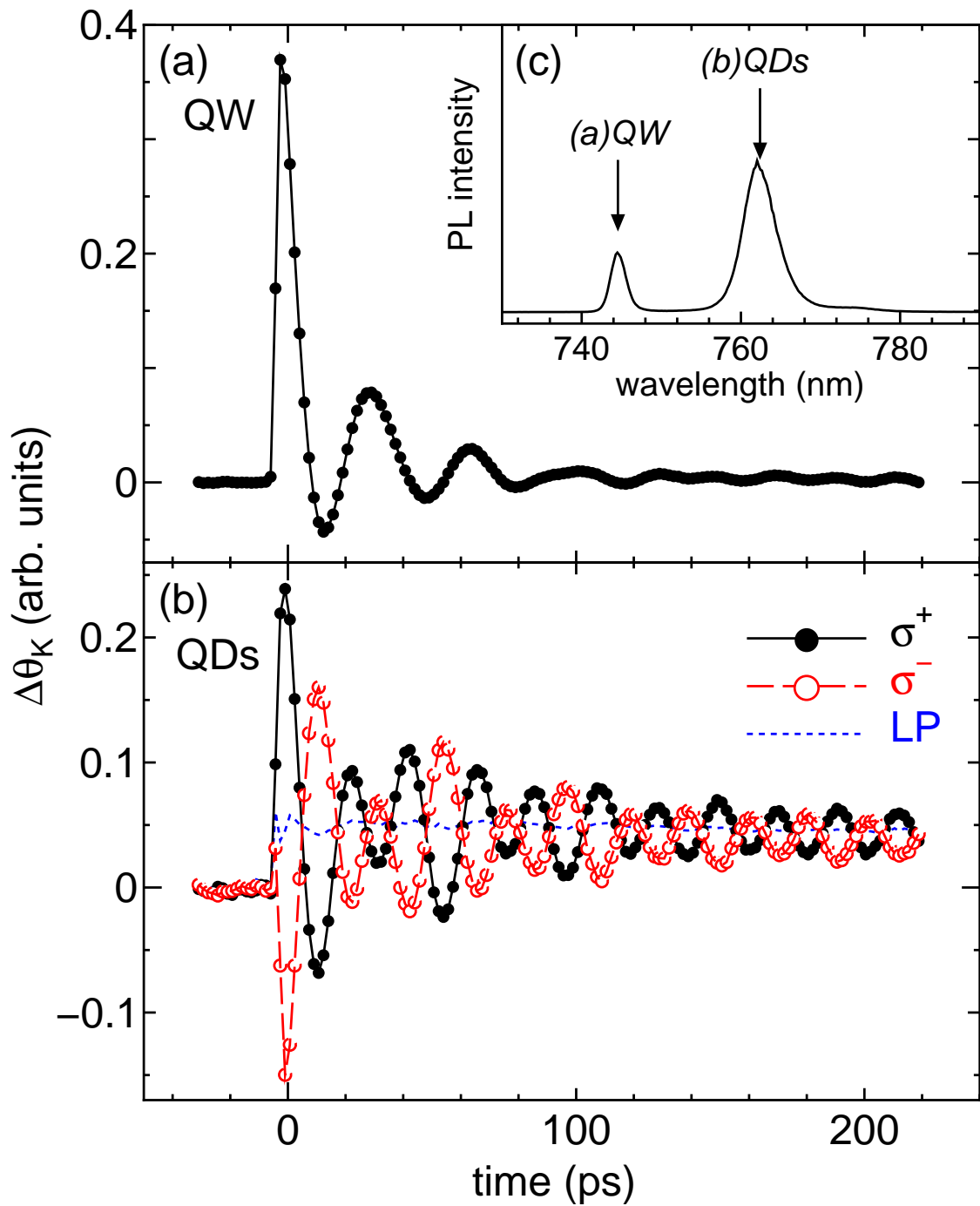


Fig. 4.3 TRKR signals under the magnetic field  $B = 8$  T at  $T = 10$  K for (a) a quantum well and (b) quantum dots. (c) Photoluminescence spectrum at  $B = 0$  T and  $T = 10$  K. The arrows show the probe energies for a quantum well and quantum dots.

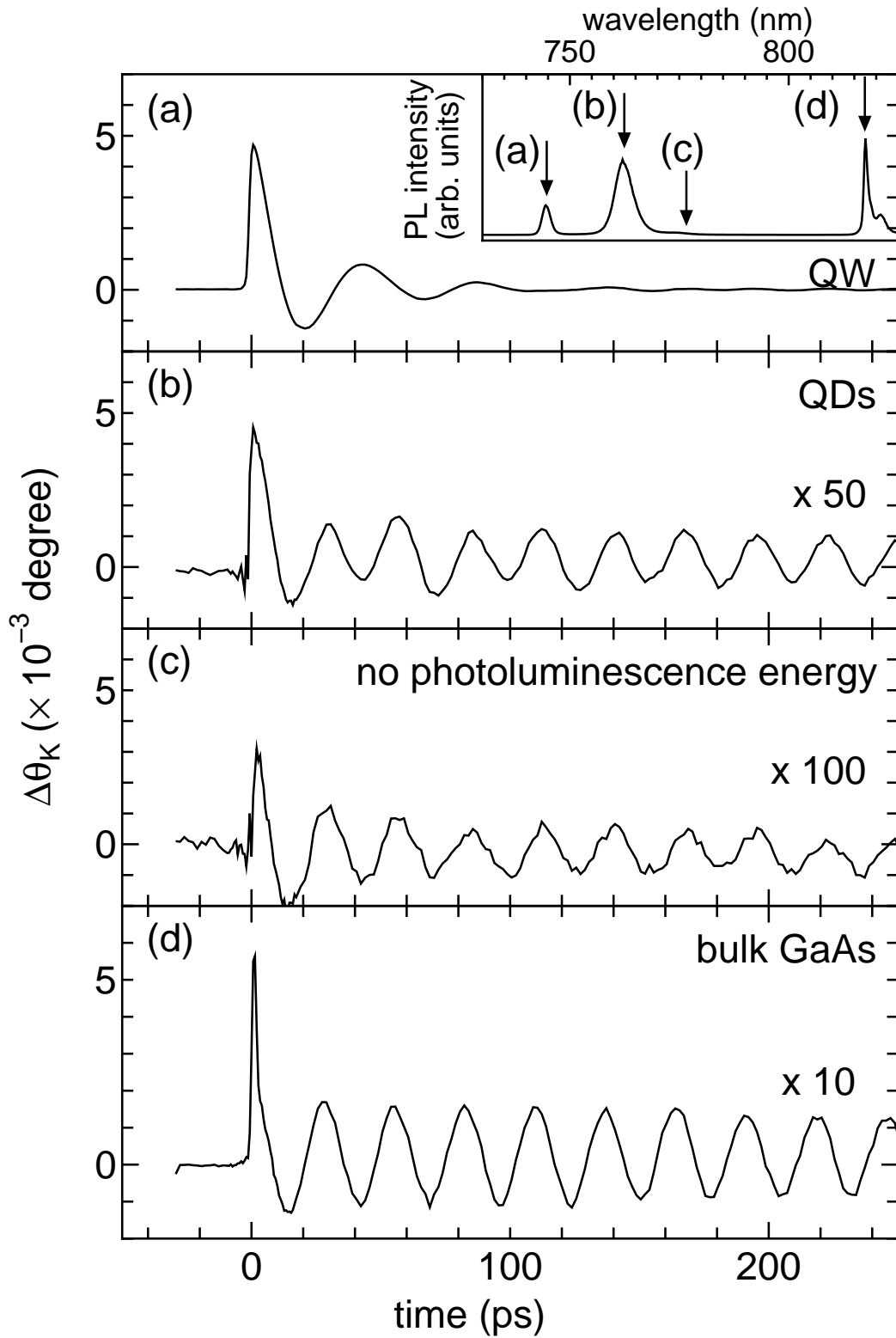


Fig. 4.4 TRKR signals at four different probe energies at  $T = 10$  K and  $B = 6$  T. These probe energies are (a) 746 nm (for QW), (b) 762 nm (for QDs), (c) 772 nm and (d) 816 nm (for bulk GaAs). The photoluminescence spectrum is also shown in the inset.

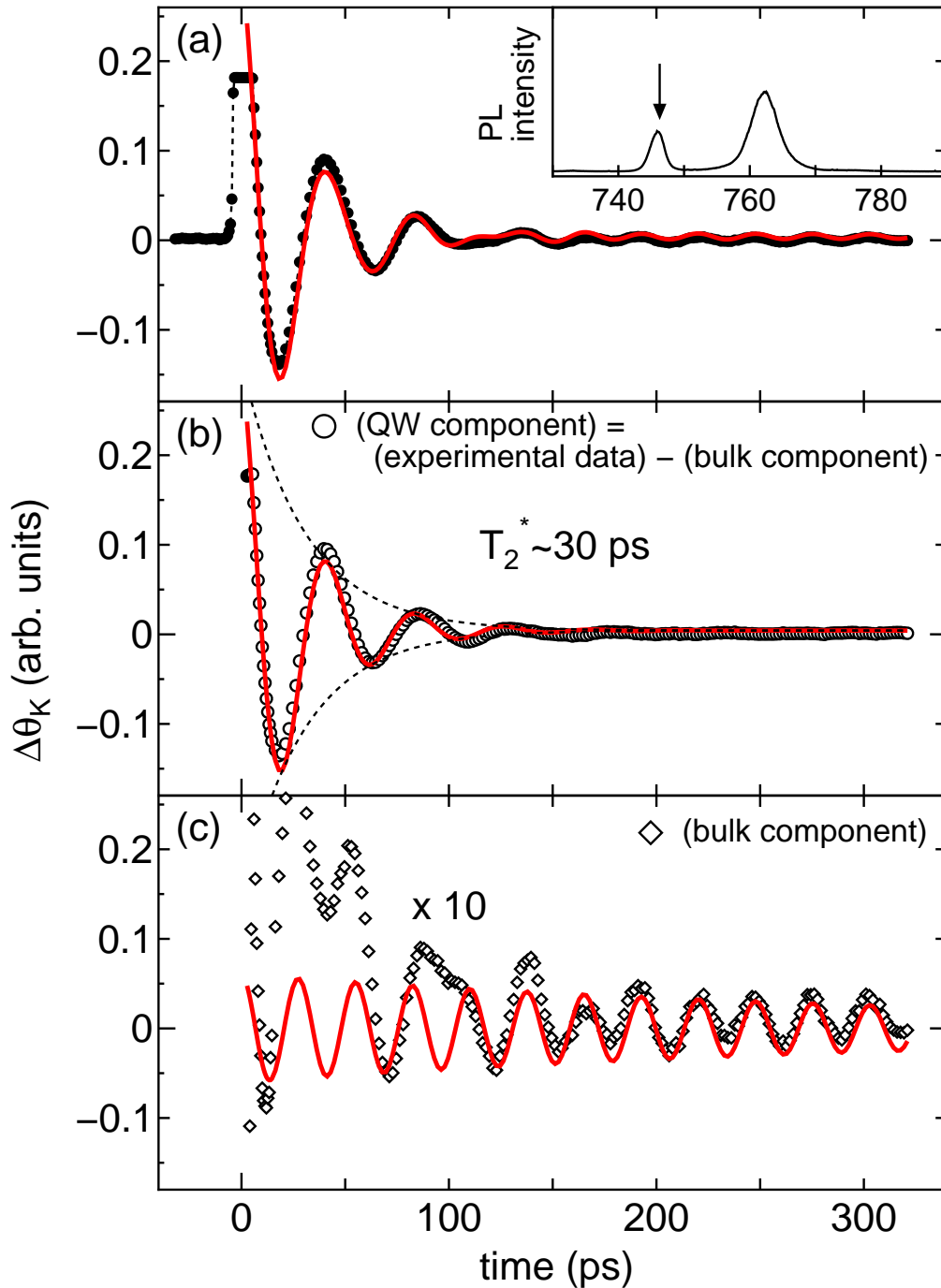


Fig. 4.5 Component analysis of TRKR signal for quantum well. (a) shows the experimental data (closed circles) and calculated signal (red solid line) by sum of two components. One component is originated from (b) quantum well, and the other is from (c) bulk GaAs. Open circles (diamonds) show the calculated data, which is subtraction of the fitting data for bulk GaAs (QW) from the experimental data. The red solid lines are fitting curves. The photoluminescence spectrum is also shown in the inset with an arrow, which indicates the probe energy.

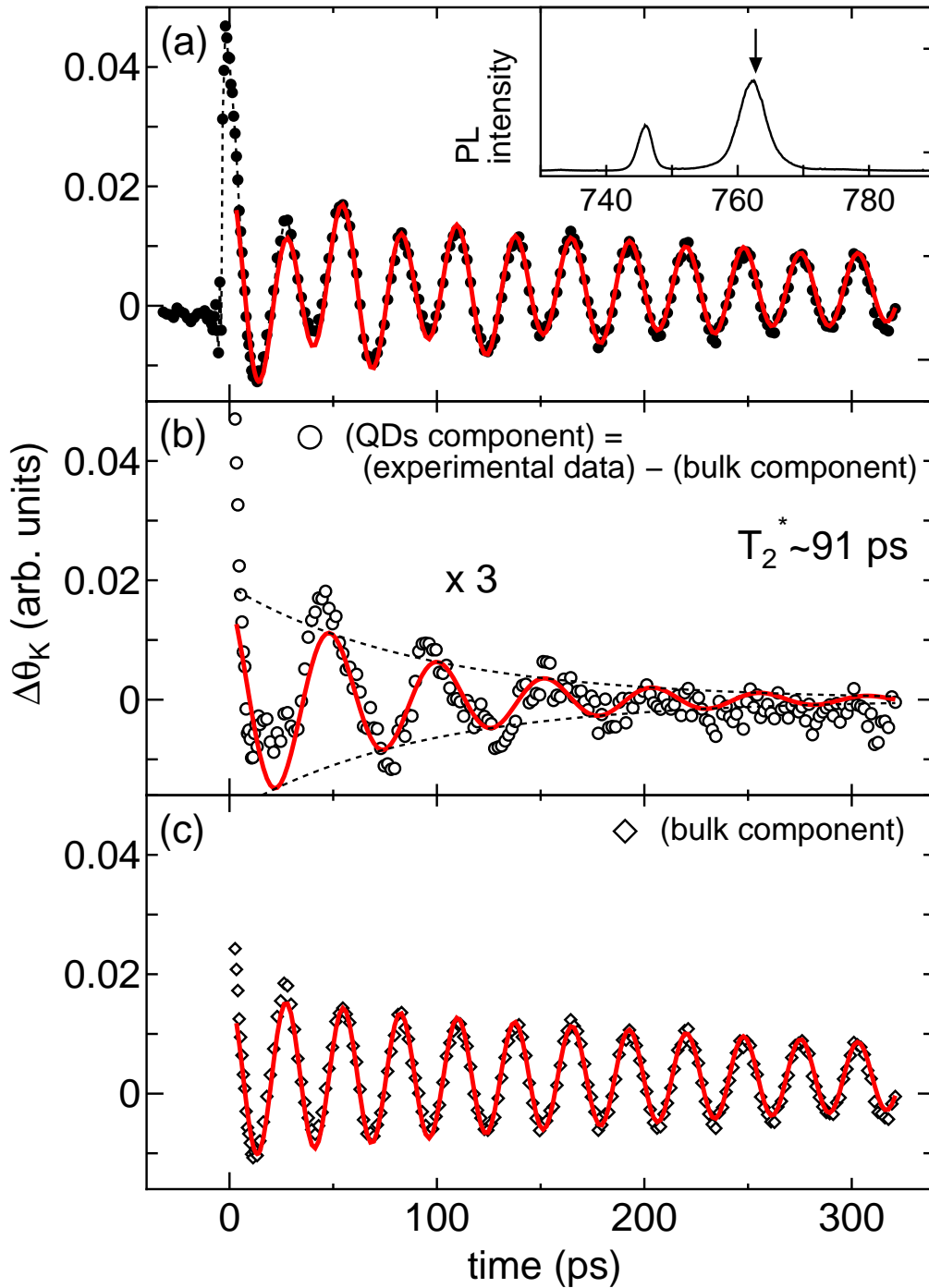


Fig. 4.6 Component analysis of TRKR signals for quantum dots. (a) shows the experimental data (closed circles) and calculated signal (red solid line) by the sum of two components. One component is originated from (b) quantum dots, and the other is from (c) bulk GaAs. Open circles (diamonds) show the calculated data which is subtraction of subtract the fitting data for bulk GaAs (QDs) from the experimental data. The photoluminescence spectrum is also shown in the inset with an arrow, which indicates the probe energy in this experiment.

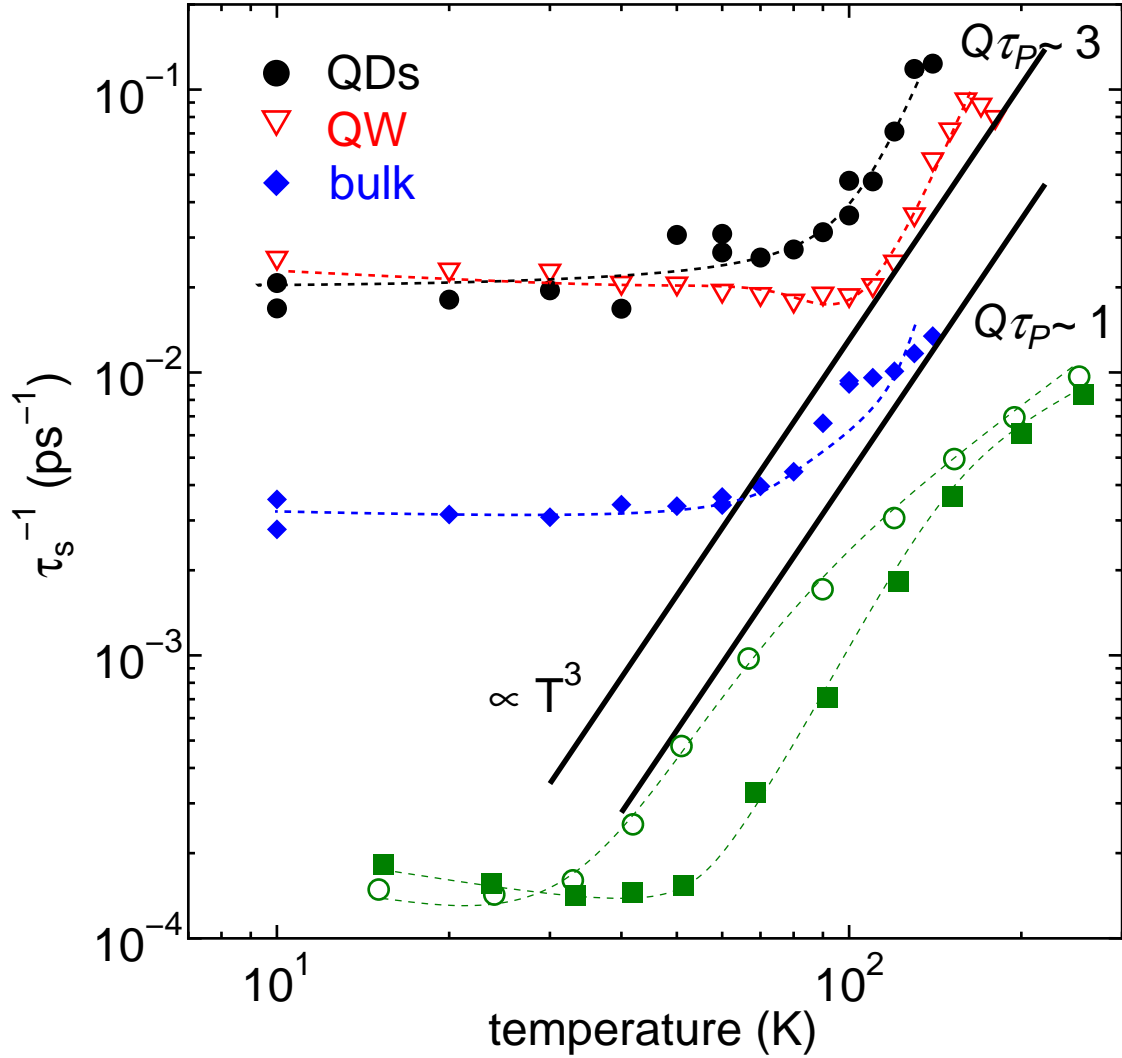


Fig. 4.7 Temperature dependence of spin relaxation rate for the QDs (black closed circles), QW (red open triangles) and bulk GaAs (blue closed diamonds). The green marks show the spin relaxation rates for p-GaAs [18]. The thick solid lines indicate the spin relaxation rate due to the DP mechanism at  $Q\tau_p \sim 3$  and  $Q\tau_p \sim 1$ .

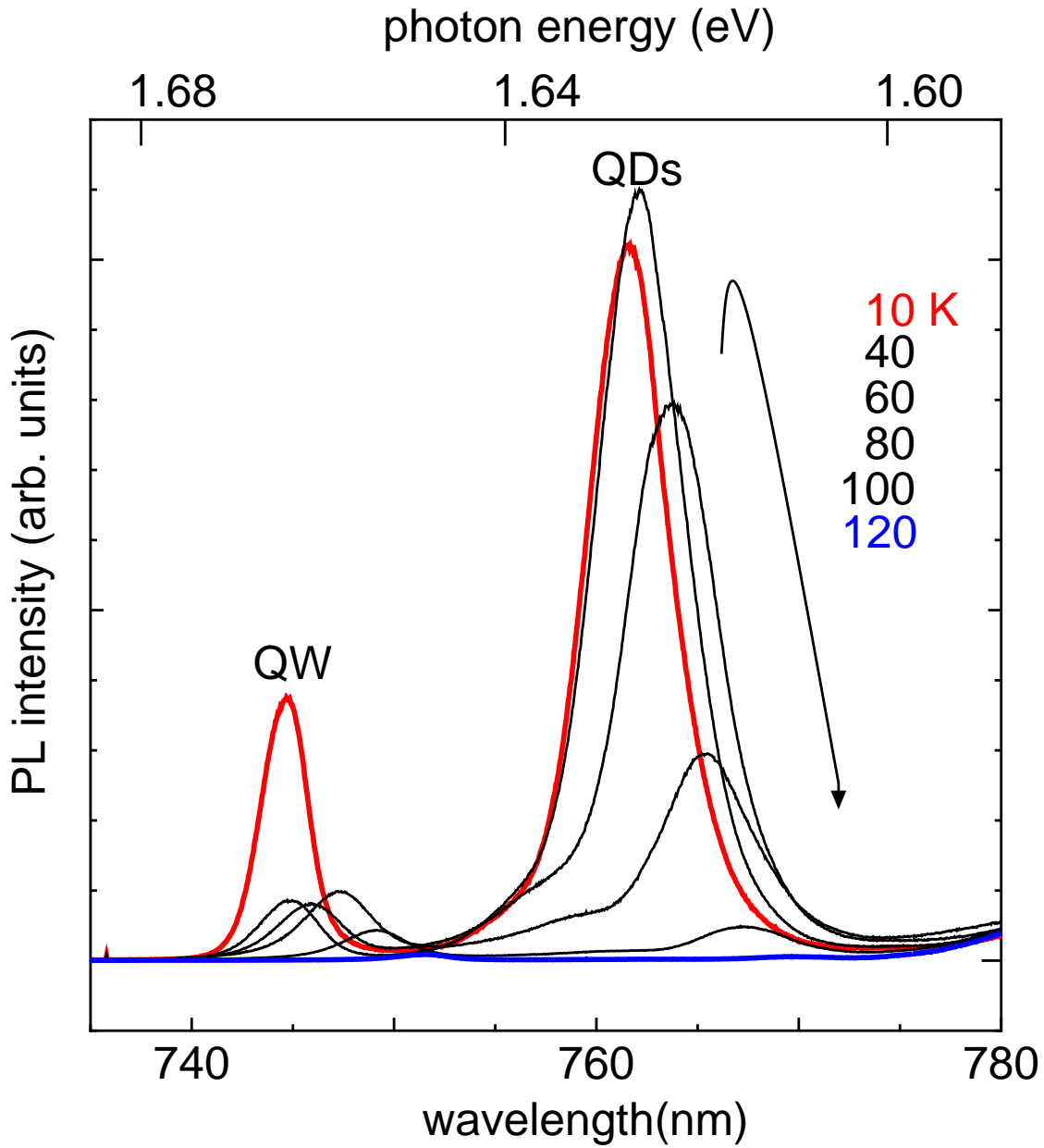


Fig. 4.8 Temperature dependence of photoluminescence without a magnetic field. The excitation light source is the frequency-doubled output of the Ti:sapphire laser. The wavelength and power are 400 nm and under  $1 \text{ W/cm}^2$ , respectively. The intensity of the photoluminescence decreases with increasing temperature, and the peak energy is red-shifted. At  $T \geq 100 \text{ K}$  the photoluminescence for the QDs almost annihilates.

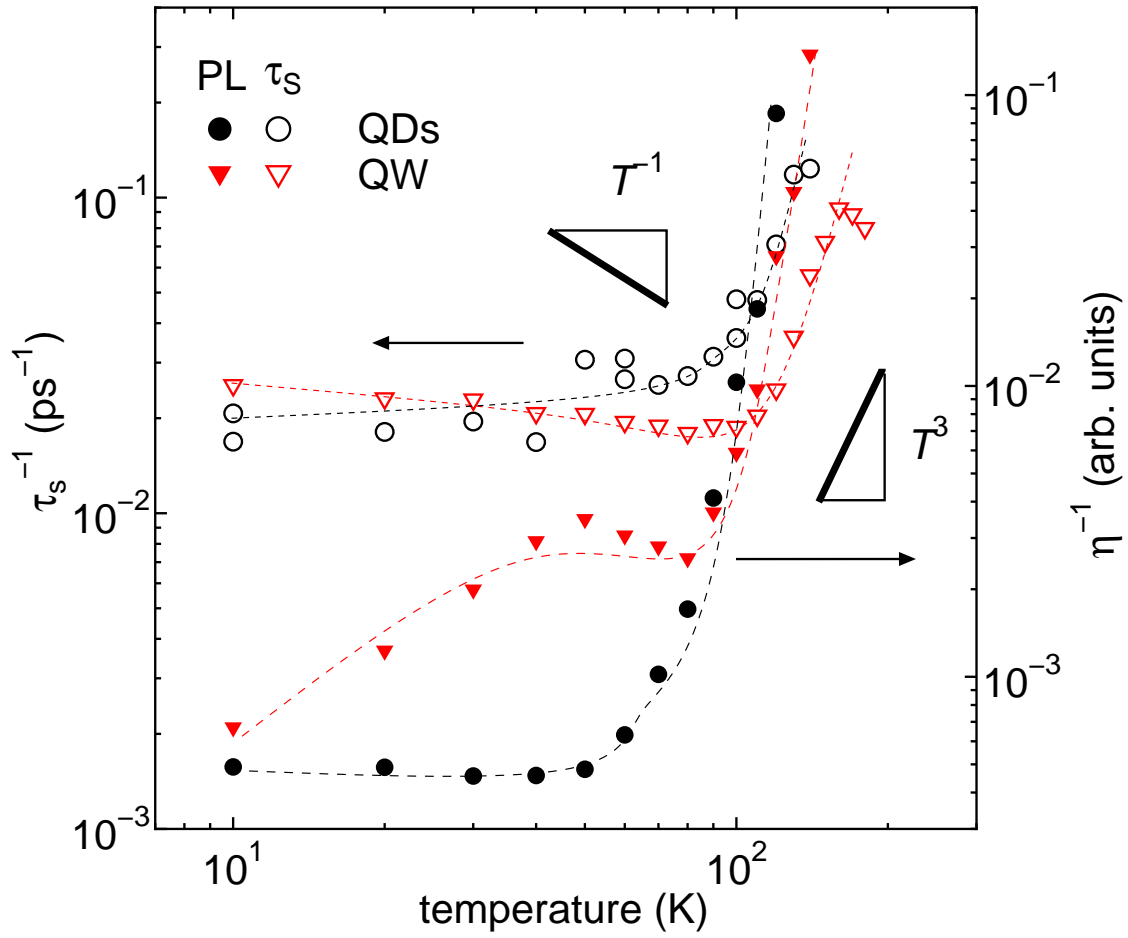


Fig. 4.9 Temperature dependence of photoluminescence efficiencies  $\eta$  for the QDs (black closed circles) and QW (red closed triangles) and spin relaxation rates for the QDs (black open circles) and QW (red open triangles). The behavior for the photoluminescence efficiency for the QDs is similar to that of the spin relaxation rate  $\tau_s^{-1}$ .

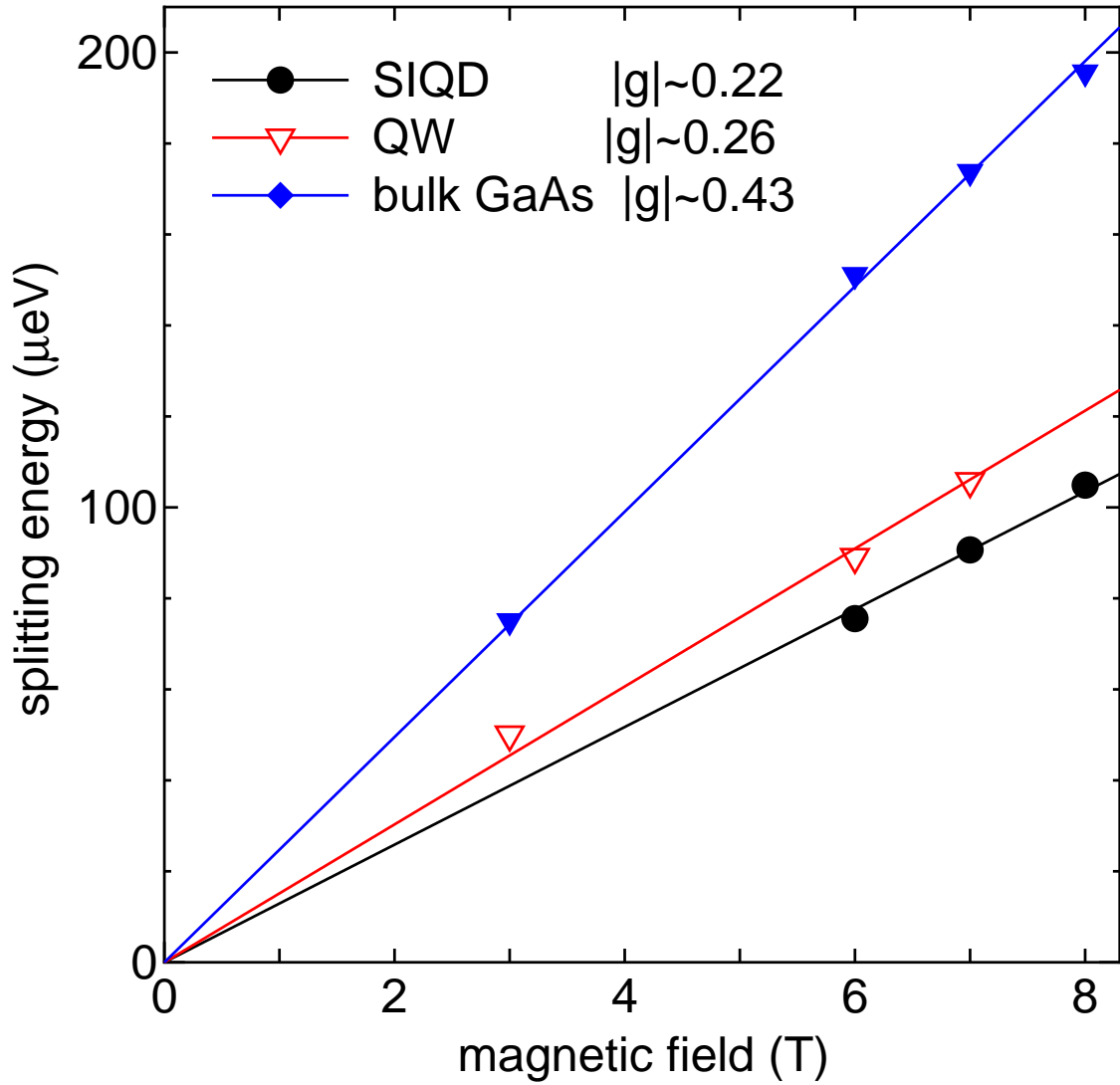


Fig. 4.10 Magnetic field dependence of splitting energies ( $\Delta E = g\mu_B B$ ). The symbols are obtained from the oscillation period of the TRKR signal for the QW (red open triangles), QDs (black closed circles) and bulk GaAs (blue closed diamonds). Solid lines are fitting ones of the observed splitting energies by linear relationship.

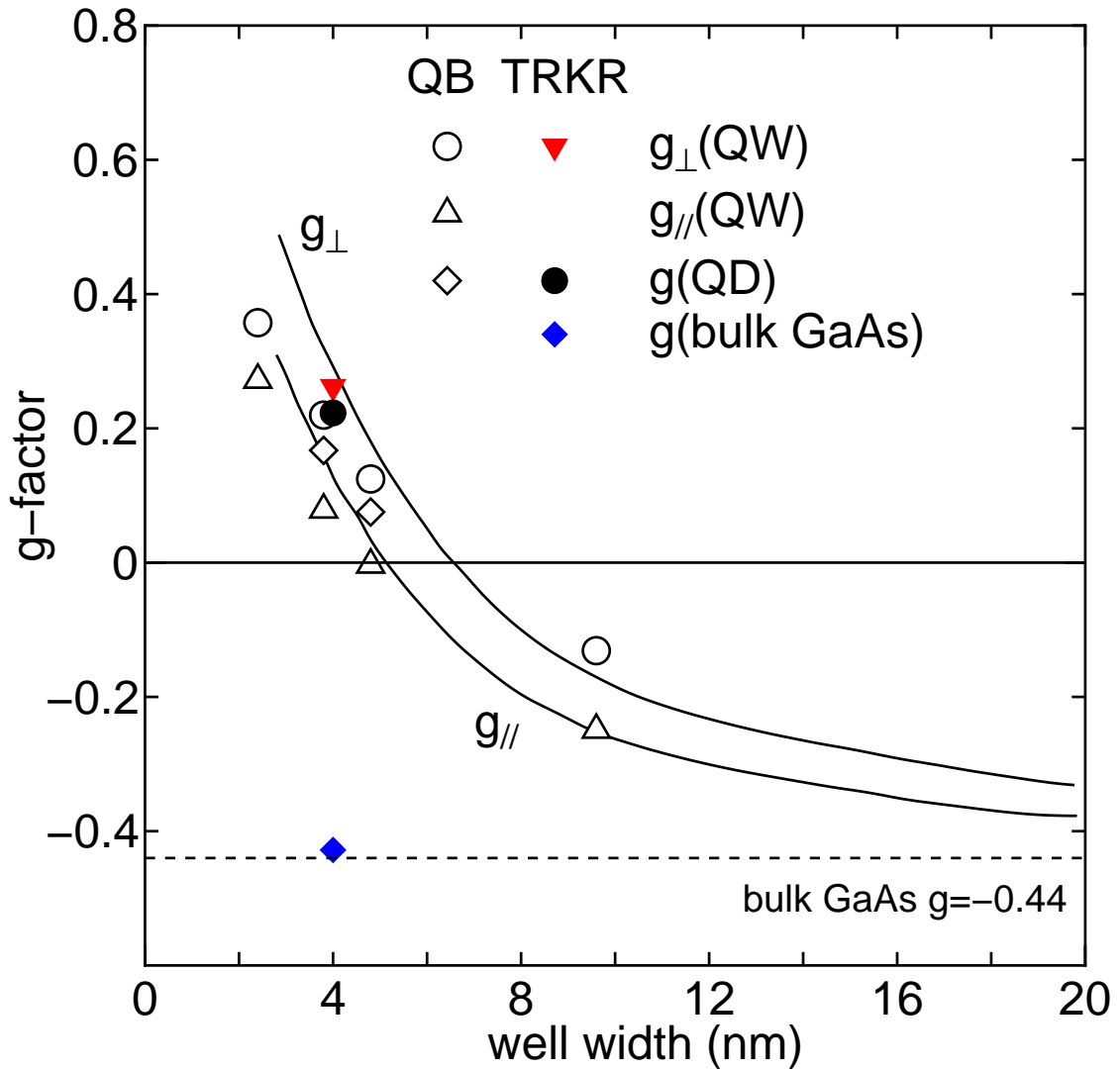


Fig. 4.11 Well width dependence of electron g-factor for the QW, QDs and bulk GaAs. Closed marks show the electron g-factors taken by photoluminescence quantum beat measurements for the different size of InP stressor dots (about 90 nm) [17]. Open marks and cross are the estimated electron g-factors in this TRKR measurement. A solid line shows the calculated electron g-factors,  $g_{\parallel}$  and  $g_{\perp}$ , in a single quantum well in the Kane model by Ivchenko [42].

## 4.2 Self-assembled InP Quantum Dots

Figure 4.12 shows the TRKR signals at  $T = 10$  K under a transverse magnetic field  $B = 8$  T. The wavelengths of the pump and probe beams are about 765 nm and 771 nm, respectively. The reason why we set the different pump and probe energies is discussed below. The intensity ratio between the pump and probe beams is about 10:1. In Fig. 4.12, it is clearly seen that the completely anti-phase oscillation is observed for the right and left circularly polarized excitation. This indicates that these oscillations are originated from Larmor precession of the carrier spins generated by the pump light because these carrier spins become opposite direction in cases of right and left circularly polarized excitations. The TRKR signal without a magnetic field is also shown in Fig. 4.13. In zero field, the decay is well fitted by

$$I(t) \propto e^{-\frac{t}{\tau_{decay}}}.$$

Under the magnetic field  $B = 5$  T, the TRKR signal is well fitted by

$$I(t) \propto e^{-\frac{t}{T_2^*}} \cos\left(\frac{2\pi t}{\tau_{precess}}\right).$$

These fitting parameters  $\tau_{decay}$ ,  $T_2^*$  and  $\tau_{precess}$  are about 60 ps, 98 ps and 270 ps, respectively. As the probe energy is tuned closer to the bulk GaAs energy (816 nm), the oscillation of the TRKR signal from the GaAs substrate is observed as mentioned for the strain-induced quantum dots in Section 4.1. The decay time of the envelope of the oscillatory TRKR signal is faster than that for SIQDs. The difference of the substrate, semi-insulating GaAs for SIQDs and n-type GaAs for InP QDs, plays an important role in this behavior. This change of the decay time is due to the number of doped carriers. In fact, Kikkawa and Awschalom reported that the coherence time of electron spins for a GaAs is changed by their doping level [43]. The result in this work is consistent with the report. In addition, since the TRKR component from the bulk substrate vanished faster, the contribution of this component to the TRKR signal for the QDs is negligible. Thus, the TRKR signals for the QDs are seen as a single component.

The probe energy dependence of the TRKR signal without a magnetic field is shown in Fig. 4.14. The spectral shape of the TRKR signal for the QDs is the so-called *dispersive* type. This

shows the different behavior from the probe energy dependence for SIQDs. In InP QDs, the peaks of the TRKR signal for the QDs disagree with that of the photoluminescence. The peak of the TRKR signal for the bulk GaAs, however, agrees with that of the photoluminescence and is consistent with the results for the SIQDs. This indicates that the behavior of the TRKR signal for the QDs in this case is different from that for the SIQDs. We take into account the equation (2.1),

$$I(t) \propto |r_+||r_-|\theta_K \sin 2pt .$$

The detected signal is dependent not only on the Kerr rotation angle  $\theta_K$  but also on the reflection coefficients  $|r_{\pm}|$ . The change of these reflection coefficients may contribute dominantly to the TRKR signal because their probe energy dependence is much larger than that of the rotation angle. Another explanation about the optical Kerr effect for n-GaAs was reported by Kimel et al. [14]. Assuming the spin-related energy splitting between the energy levels for right and left circularly polarized light, called *diamagnetic*, they calculated the spectrum of the Kerr rotation showing the *dispersive* shape [44]. It may indicate that the electron and/or hole energy levels for this QDs may be separated according to their spin.

The TRKR signals for the QDs under several magnetic fields are shown in Fig. 4.15. It is clearly observed that the oscillation period of the TRKR signals becomes shorter with increasing transverse magnetic field. By using the following relation,

$$I(t) \propto e^{-\frac{t}{\tau}} \cos\left(\frac{2\pi t}{\tau_{precess}}\right) ,$$

we estimated the energy splittings  $\Delta E = g\mu_B B = \hbar/\tau_{precess}$  from the observed TRKR signals. They are shown in Fig. 4.16. These are expressed well by linear dependence. Calculating from the slope of this fitting line, we obtained the absolute value of the g-factor, which is about 0.052. However, there remains a problem on which kind of carrier precesses. This is discussed below.

There are some reports on the electron g-factor in self-assembled InP quantum dots by Ignatiev et al. which are based on photoluminescence quantum beat measurements [6–9]. According to them, the electron g-factor is about 1.5. This is much larger than the obtained g-factor

$|g| \sim 0.052$  in this work. In addition, the value is far from the g-factor in bulk InP, that is 1.48 [34]. Thus, the observed oscillation is not due to the electron spin precession. On the other hand, the g-factor of hole spin was estimated to be about 0.1 by photoluminescence quantum beat experiment by Ignatiev et al. [8]. This value is close to the g-factor observed in this work. The small g-factor of about 0.05 for the heavy hole in the GaAs quantum well was also obtained from quantum beats experiments by Marie et al. [5]. This small value is caused by the quantum confinement effect. Considering these reports, we can conclude that the observed g-factor is originated from the photoexcited holes.

Why the Larmor precession of the hole spin is observed? In the studied sample, the quantum dots are charged unintentionally. Electrons are moved from the n-type GaAs substrate to the quantum dots. In fact, the evidences of the negatively charged quantum dots are shown in recent reports [6–9]. Next, we try to discuss the reason why we detect Larmor precession of holes in the charged quantum dots.

The energy of the probe light is lower than the peak energy of the photoluminescence. Because we excite only large quantum dots, the photoexcited electrons are not in the excited states of the QDs. Therefore a photoexcited electron exists with the lowest energy in a quantum dot.

The direction of the spin polarization of the electron generated by a photon is determined by the selection rule. In the negatively charged quantum dots where doped electrons are present, the spins of the photoexcited electrons become anti-parallel to the spins of the doped electrons because of the Pauli principle. Here, we assume the simple case where one doped electron exists in a quantum dot (Fig. 4.17). The spins of the doped electrons are randomly oriented first. Owing to the Pauli principle, the electron-hole pairs are generated only in QDs where the spins of the doped electrons have to be anti-parallel to those of the photoexcited electrons. Thus, the net magnetization by two electron spins becomes zero, and they do not contribute to the Kerr rotation signal. The hole spins obviously are oriented in the same direction. As a consequence, the *rest* hole spin generated by the pump light is detected in this system.

Another mechanism can also be concerned, in which the electrons disappear quickly from the quantum dots *nonradiatively*. This mechanism is negligible in this work because the lifetime of the photoexcited electrons are quite long as is explained below. In order to demonstrate the hole spin precession, time-resolved photoluminescence experiment was performed at  $T = 2$  K and  $B = 0$  T (Fig. 4.18). This experiment was performed under the quasi-resonant excitation. The difference between the pump and probe energies was tuned to about 1 LO phonon energy for bulk InP ( $\hbar\omega \sim 43.5$  meV). The decay of this photoluminescence indicates that an electron-hole pair is alive for long time. Compared with the observed lifetime  $T_1 \sim 800$  ps, the spin relaxation time  $T_2^* \sim 100$  ps is much shorter. This fact shows that the observed spin relaxation time is not limited by the lifetime of the photoexcited electron-hole pair. As the electron generated by a photon is alive during this spin relaxation time, the canceling mechanism is considered to be effective.

In addition, the TRKR measurement for another InP quantum dots sample was performed with applying bias. We could not observe the TRKR signal for the QDs, but the signal for the bulk GaAs was observed (Fig. 4.19). The oscillation frequency at the different bias is slightly different. The spin relaxation time and the carrier g-factor depending on the applied bias are shown in Fig. 4.19. We can observe the drastic change of these values at the bias  $V = -2$  V. The electron g-factors at  $V > -2$  V and  $V < -2$  V are estimated to be 0.366 and 0.394, respectively. These are smaller than that for bulk GaAs, that is -0.44. We discuss this difference below. The buffer GaAs layer is about 500 nm thick, and is located between the  $\text{Ga}_{0.5}\text{In}_{0.5}\text{P}$  barrier layer and the n-GaAs substrate. In fact, we could observe the TRKR signal for the buffer GaAs because of the thick buffer layer. Thus, it is considered that the electrons of the interface form two-dimensional electron gas. The g-factors of electrons for a GaP and InP are about 1.6 and 1.5, respectively [45]. Then the g-factor of electrons for a  $\text{Ga}_{0.5}\text{In}_{0.5}\text{P}$  should be positive and be about 1.55. When the wavefunction of the electron is located at the interface between the buffer and barrier layer, its g-factor can be the average of the g-factors for two materials, GaAs and  $\text{Ga}_{0.5}\text{In}_{0.5}\text{P}$ . Thus, the g-factor is estimated to be smaller than that for the bulk GaAs. This is

the reason why the estimated g-factor is smaller. Next, when we applied the negative bias to the sample, the observed g-factor is larger than that at the bias voltage  $V > -2$  V. At the applied negative bias, the wavefunction of the electron moves to the substrate, thus, it is attracted to the substrate (Fig. 4.20). Therefore, the g-factor becomes larger, and close to the value for the bulk GaAs. The spin relaxation times are varied depending on the applied bias. This may indicate that the number of the surrounding doped electrons is varied by applying bias. It is consistent with the report mentioned above [43]. This result indicates that we can control the electron g-factor and the spin relaxation time by applying bias voltage.

In summary, the TRKR signal for single-layer self-assembled InP quantum dots is detected, and the spin precession of the photoexcited holes is observed.

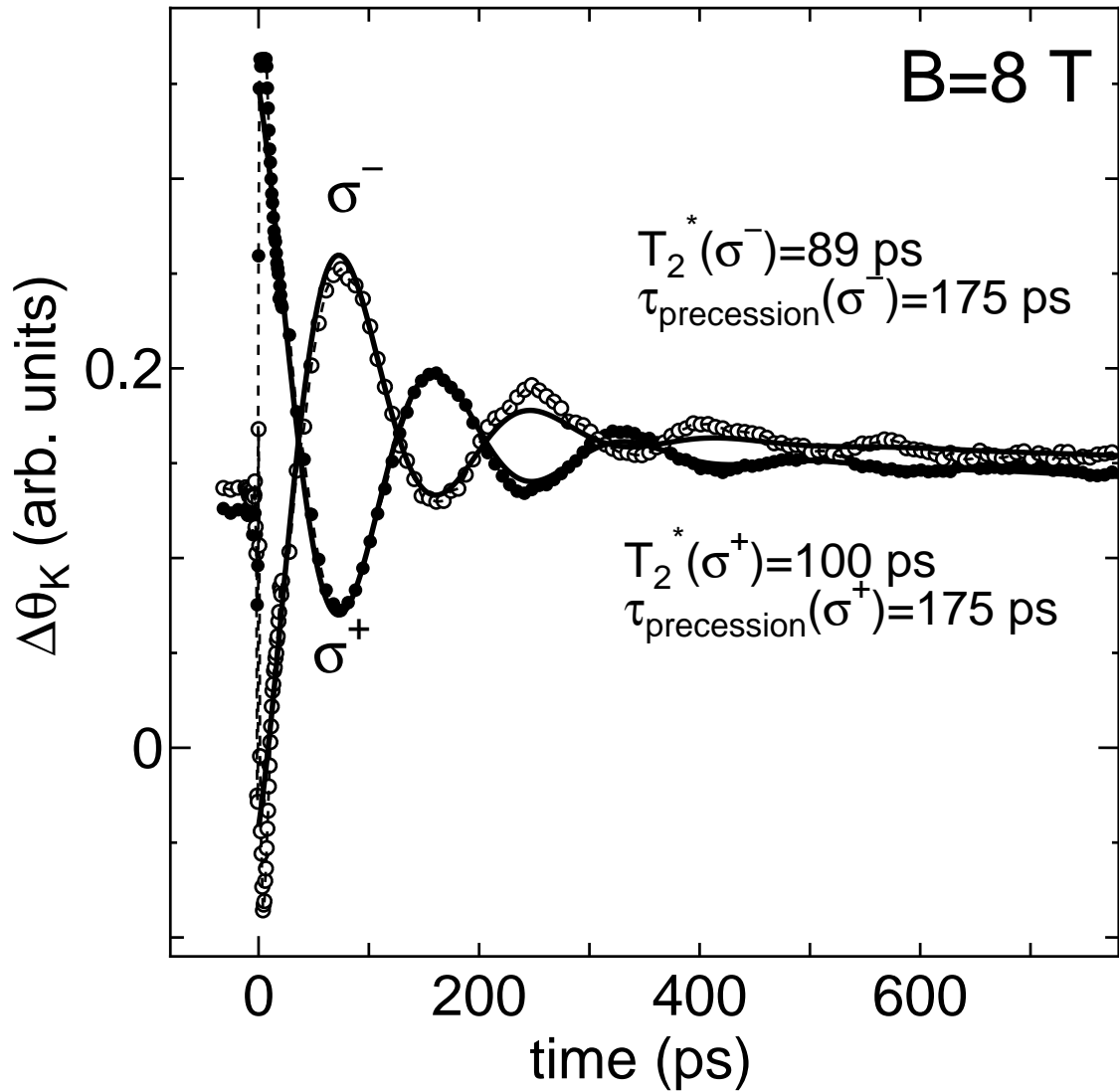


Fig. 4.12 TRKR signals for self-assembled InP quantum dots at  $T = 10$  K under the transverse magnetic field  $B = 8$  T. Closed (open) marks indicate the TRKR signal excited by a right (left) circularly polarized light. The solid lines are fitting ones. The observed spin relaxation time is about 90 ps.

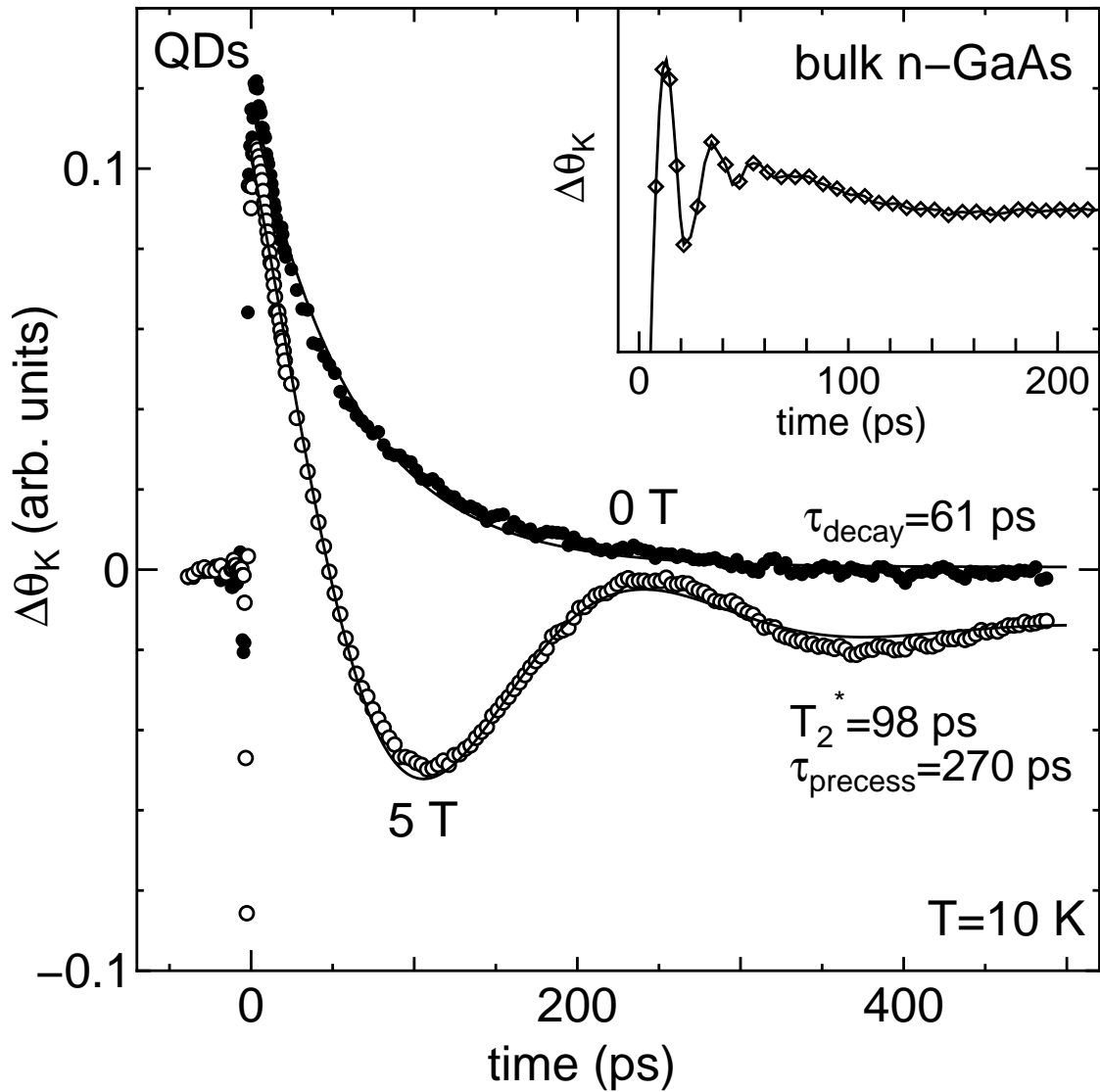


Fig. 4.13 TRKR signals for self-assembled InP quantum dots at  $T = 10$  K and  $B = 0$  T (closed circles) and 5 T (open circles). Solid lines are fitting ones of these data. At  $B = 5$  T, the decay time of the envelope function is about 98 ps and the oscillation period is about 270 ps. The pump and probe energies are 765 nm and 772 nm, respectively. The ratio of the pump and the probe intensity is about 10:1. Inset: The TRKR signal for a bulk n-GaAs substrate. The pump and probe energies are 816 nm. The precession from the substrate vanishes much faster than that from the bulk GaAs substrate of strain-induced GaAs quantum dots (Fig. 4.1).

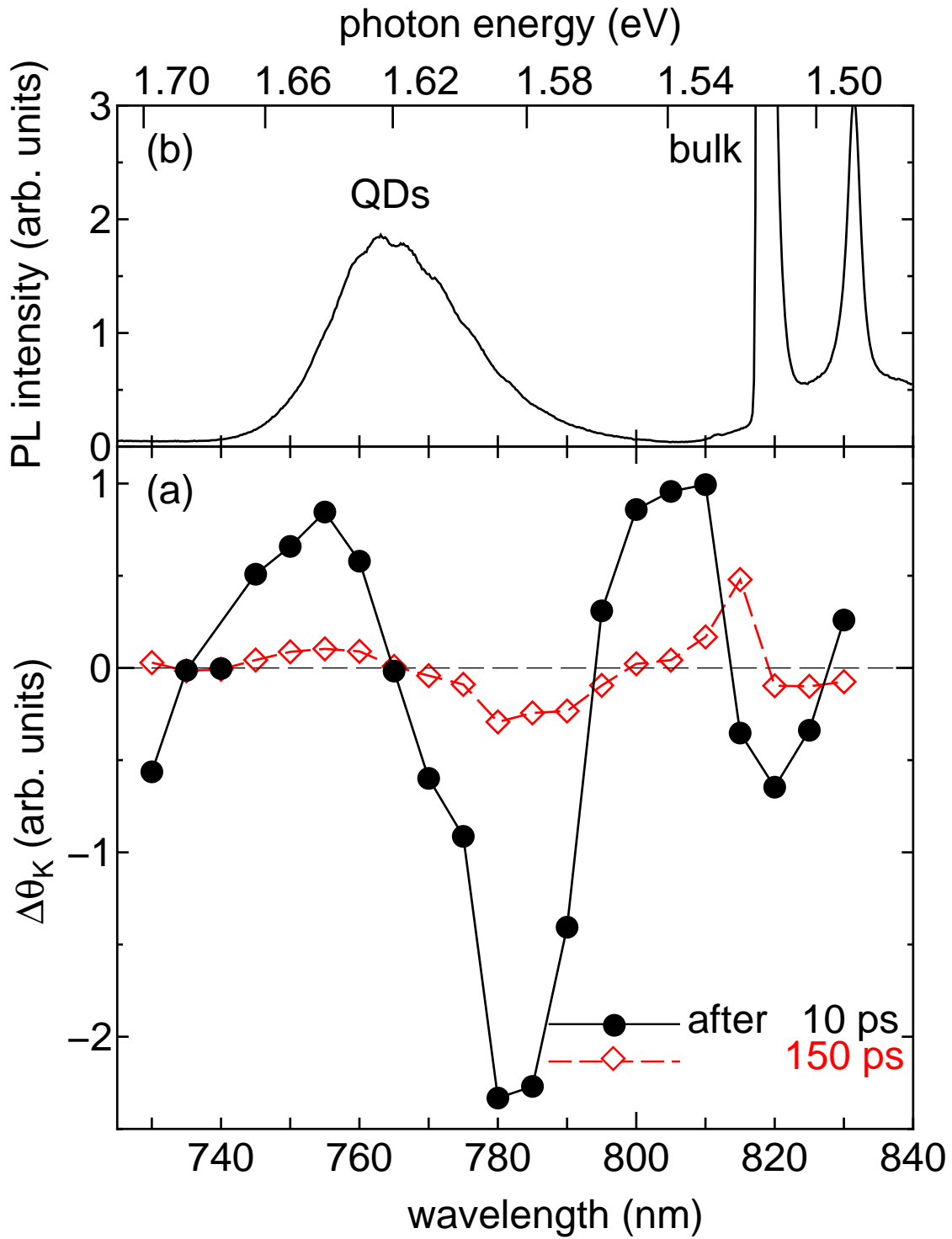


Fig. 4.14 (a) Probe energy dependence of the TRKR signal at  $T = 2$  K without a magnetic field. Closed circles are taken at the optical delay time of 20 ps and open diamonds are taken at 150 ps. (b) Photoluminescence spectrum.

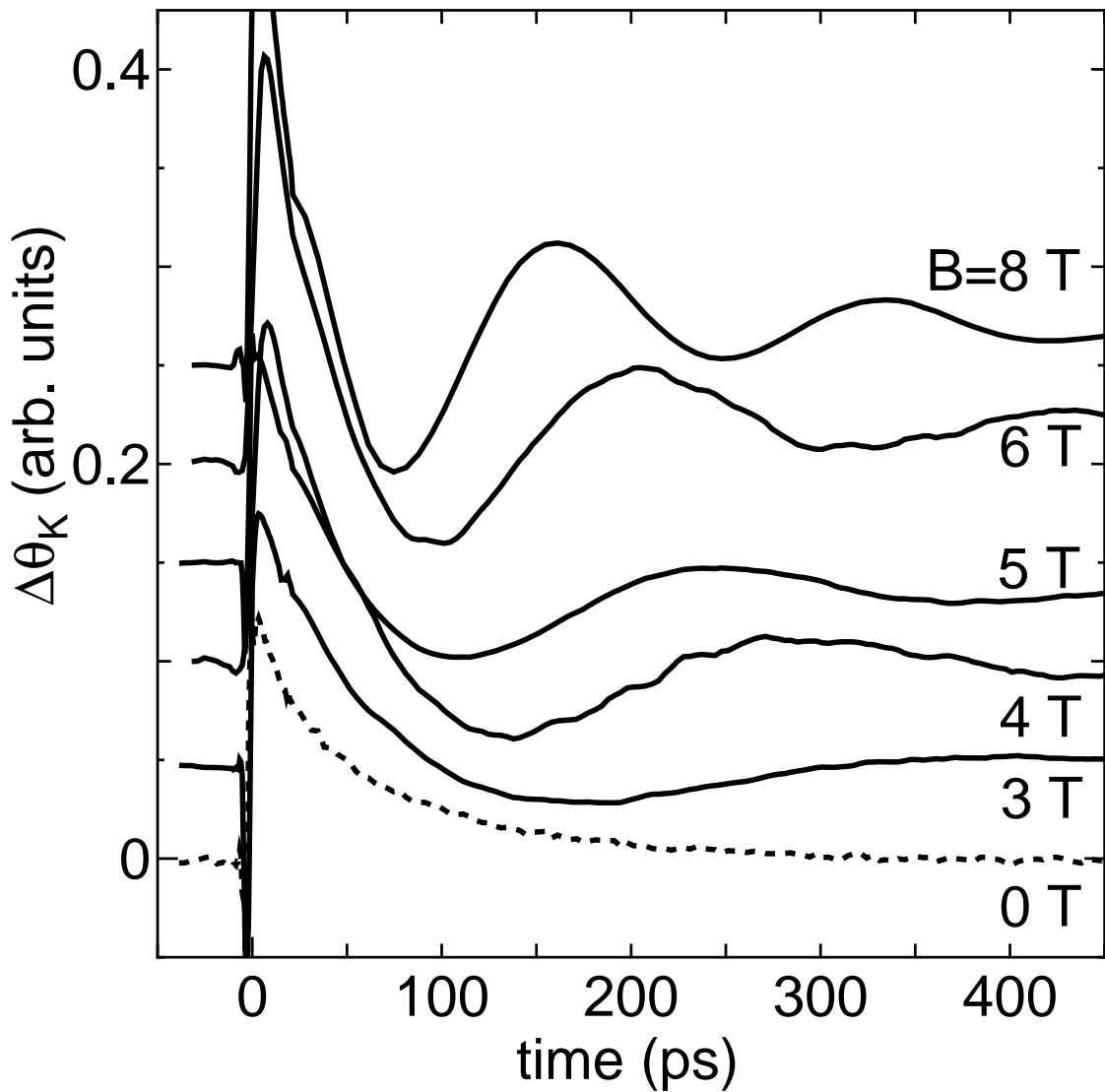


Fig. 4.15 TRKR signals for InP quantum dots under several magnetic fields ranging from 3 to 8 T at  $T = 10$  K. The TRKR signal without a magnetic field (dashed line) is also shown. The base lines are shifted for clarity. It is clearly observed that the oscillation frequency becomes shorter with increasing the magnetic field.

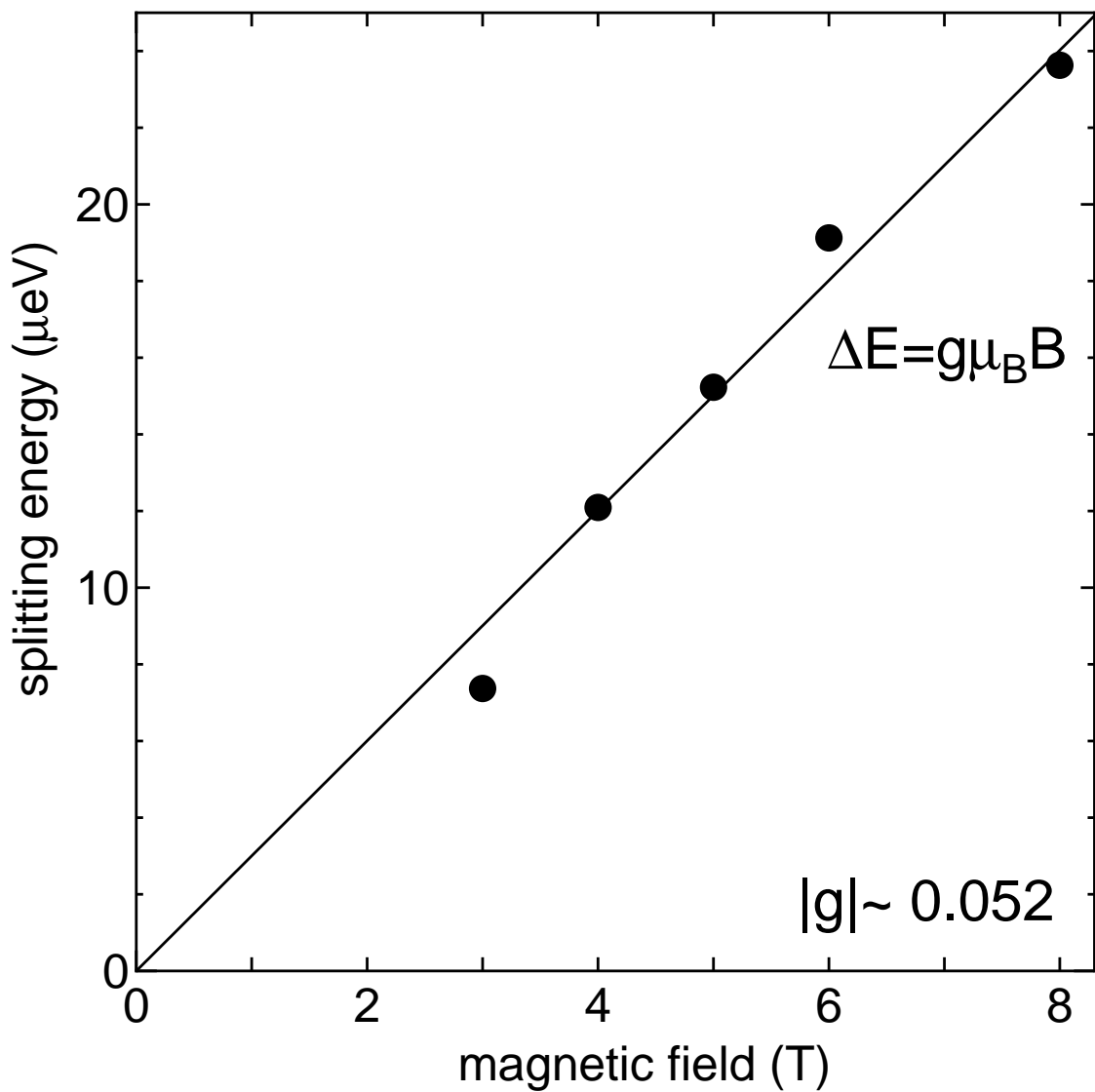


Fig. 4.16 Magnetic field dependence of the splitting energy ( $\Delta E = g\mu_B B$ ) estimated from the oscillation frequencies in Fig. 4.15. A solid line is the fitting one of the observed splittings (closed circles) assuming linear dependence. The absolute value of g-factor is about 0.052, which is estimated from the slope of the fitting line.

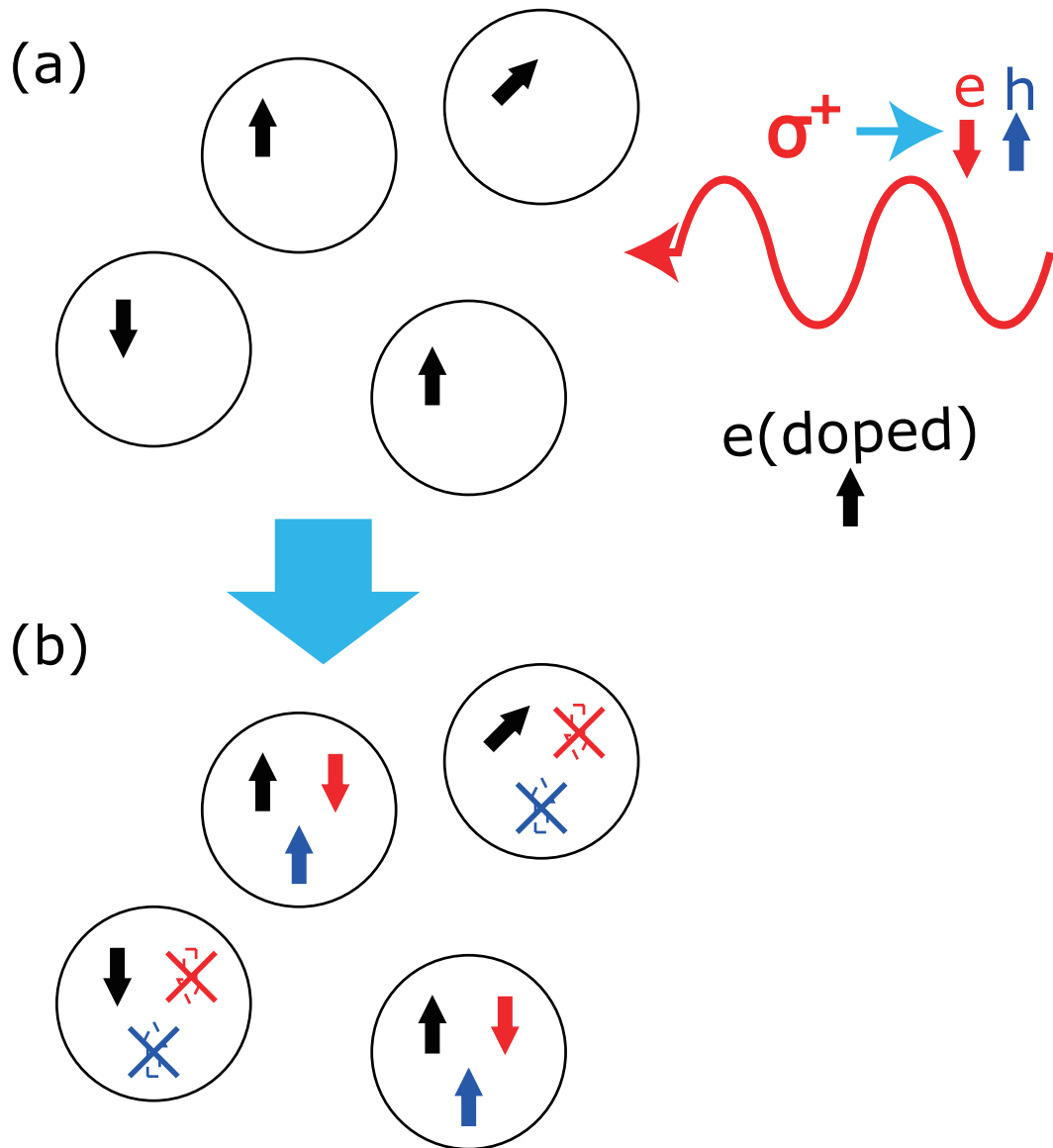


Fig. 4.17 Schematic image of carrier spins in negatively charged quantum dots. (a) The spins of the doped electrons (black arrows) are randomly oriented in quantum dots. The incident light with circularly polarization generates electron (red arrows) -hole (blue arrows) (e-h) pairs in the QDs. (b) Owing to the Pauli principle, the e-h pairs are generated only in the QDs where the spins of the doped electrons are anti-parallel to those of the photoexcited electrons. The photoexcited holes obviously must have the oriented spins in the same direction. Since the net magnetization of the electrons becomes zero, the precession of the remaining hole spins is seen in the TRKR measurement.

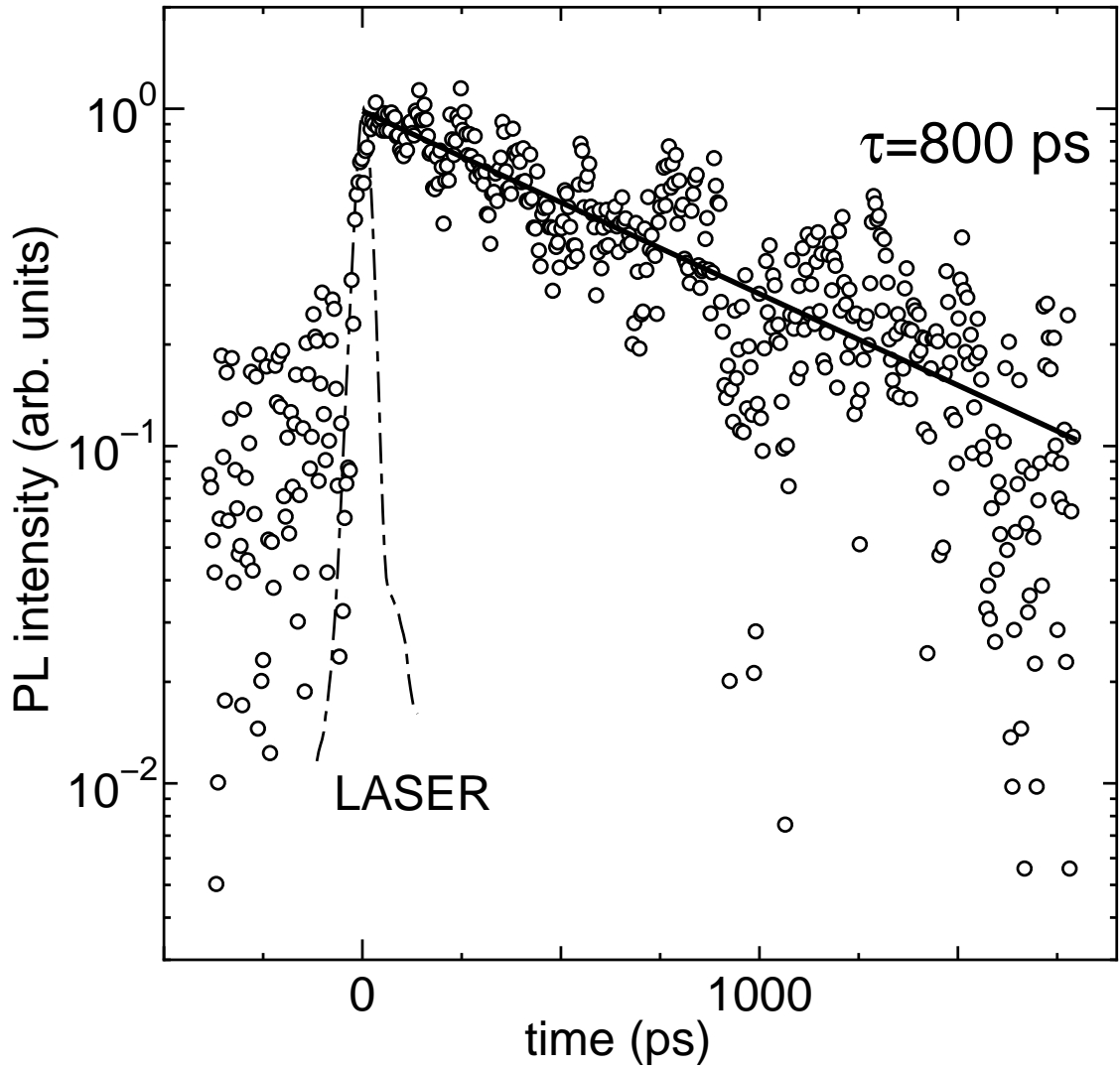


Fig. 4.18 Time-resolved photoluminescence for InP quantum dots at  $B = 0$  T and  $T = 2$  K. The excitation photon energy and density are 743 nm and  $80 \text{ W/cm}^2$ , respectively. The detection energy is about 763 nm which is lower than the excitation energy by about one LO phonon energy for bulk InP ( $\hbar\omega_{LO} \sim 43.5 \text{ meV}$ ). Temporal resolution is about 30 ps in this measurement.

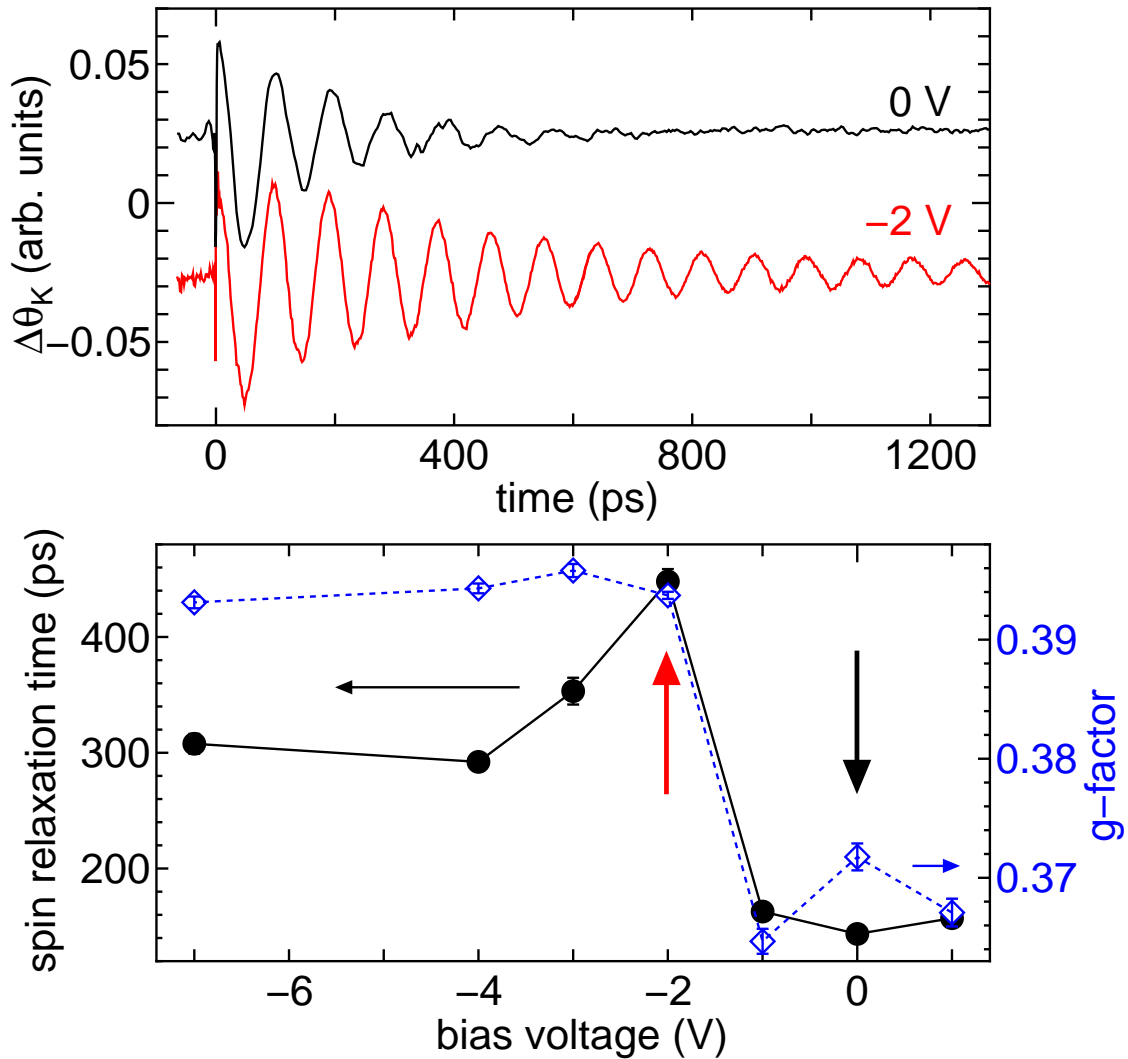


Fig. 4.19 Top: TRKR signals at the bias  $V = 0$  V, -2 V and at  $T = 10$  K under the magnetic field  $B = 2$  T. The oscillation frequency is different despite the same magnetic field. Bottom: Spin relaxation time and electron g-factor depending on the applied bias at  $T = 10$  K under the magnetic field  $B = 2$  T. Closed circles and blue open diamonds indicate the spin relaxation time and the electron g-factor, respectively. These values are drastically changed at  $V = -2$  V.

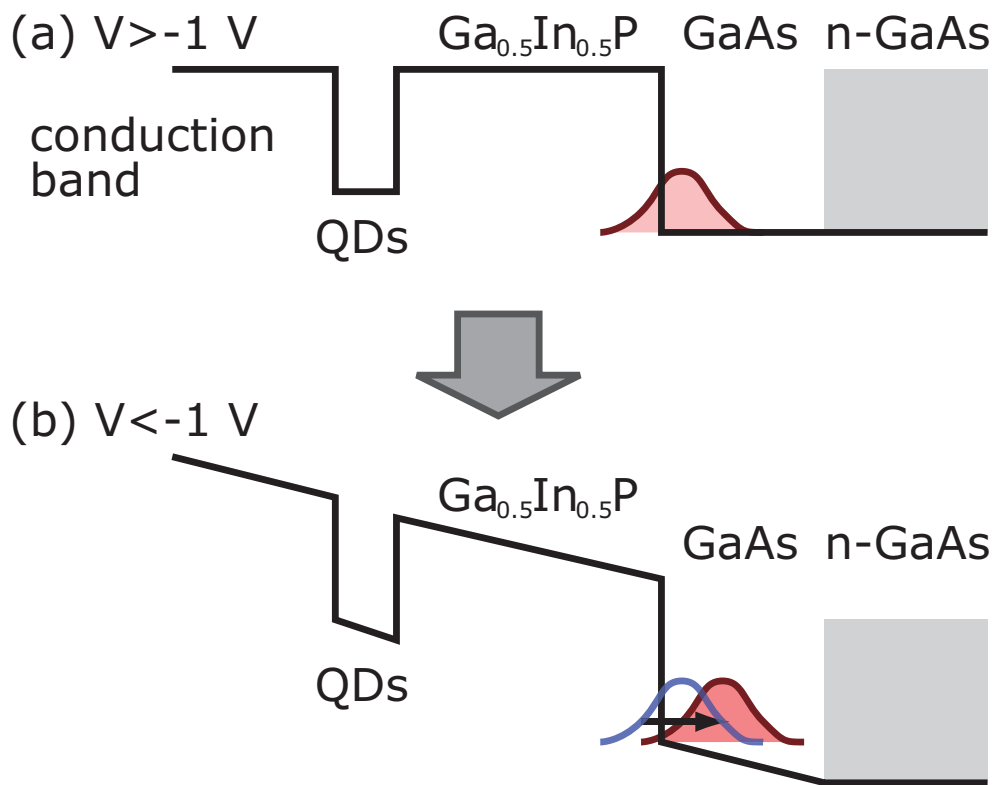


Fig. 4.20 Schematic drawing of the conduction band depending on the applied bias and the wavefunction of the electron in a GaAs buffer. (a) shows them at  $V < -1$  V. The wavefunction is located at close to the interface between an Ga<sub>0.5</sub>In<sub>0.5</sub>P barrier and a GaAs buffer. (b) At the applied negative bias, the wavefunction moves to the GaAs buffer.

# Chapter 5

## Conclusion

In this thesis, the spin dynamics for single layer quantum dots are studied by the time-resolved Kerr rotation measurement. For this study, we constructed a highly sensitive Kerr-rotation-angle detection system by means of a photoelastic modulator, an optical bridge with a balanced detector and tandem double lock-in amplifiers. The performance of this system achieved the highest angle resolution obtained so far in the world, and allows us to detect the weak signals from single-layer quantum dots. Although the weak signals coming from the quantum dots are detected, the strong signal coming from the bulk substrate was also detected because of their absorbance ratio. So the observed signals generally have two components. For strain-induced GaAs quantum dots, we successfully observed the Larmor precessions of the photoexcited electron spins in quantum dots under the transverse magnetic field. The observed electron g-factor was consistent with the results of photoluminescence quantum beat experiments and can be consistently understood with the theoretically calculated values for a quantum well. In addition, the spin relaxation time for quantum dots is found longer than that for a quantum well. This is because the spin relaxation by the DP mechanism is suppressed due to the reduction of the dimensions for electrons, and the BAP mechanism works at low temperature. This indicates the long spin coherence time in quantum dots, which is demanded for applications to quantum information processing technology. At low temperature, we observed that the spin relaxation times are almost constant. This indicates that the BAP mechanism plays an important role at low temperature because the movement of carriers is *frozen*. The relation

between the spin relaxation times for the quantum well and quantum dots and bulk GaAs can indicate that the dominant mechanism of the spin relaxation for the quantum well and quantum dots is the BAP mechanism. For self-assembled InP quantum dots, we observed Larmor precessions of the photoexcited hole spins. This is because electrons are unintentionally doped in these quantum dots from the n-type GaAs substrate, and because the vector sum of a spin of a photoexcited electron and a spin of a doped electron becomes zero. In addition, we demonstrated that the g-factor and the spin relaxation time of the electron for GaAs/InGaP interface are controlled by applying electric bias. We can measure the carrier spin dynamics for single-layer quantum dots under the resonant excitation by this highly sensitive Kerr rotation measurement.

# Acknowledgments

This study has been performed under the supervision of Prof. Yasuaki Masumoto in University of Tsukuba. I wish to express my sincere and special thanks to him for his devoted guidance to a foresight theme and his instructive suggestions and numerous discussions.

I wish to thank Prof. Tsuyoshi Okuno for his helpful suggestions and instructions on the sample preparation and the laser spectroscopies.

I would like to acknowledge Dr. Kazuki Bando and Dr. Kazuhiro Nishibayashi for their various recommendations and guidance to experiments.

I would like to thank Dr. Hong-Wen Ren for sample preparations, Dr. Shinichi Tomimoto, Dr. Bipul Pal, Dr. Ivan V. Ignatiev, Dr. Serguei Verbin and Dr. Vladimir K. Kalevich for fruitful discussions.

Especially, I am grateful to Dr. Michio Ikezawa. He always discussed with me and gave numerous help about experiments and great guidance.

I would like to thank other members of Masumoto Laboratory, especially, Wataru Maruyama for his various helps.

Finally, I would like to thank my family for their supports.

# References

- [1] D. D. Awschalom, D. Loss, and N. Samarth: Eds., *Semiconductor Spintronics and Quantum Computation* (Springer, Berlin, 2002).
- [2] R. J. Epstein, D. T. Fuchs, W. V. Schoenfeld, and P. M. Petroff, *Appl. Phys. Lett.* **78**, 733 (2001).
- [3] H. Gotoh, H. Ando, H. Kamada, A. Chavez-Pirson, and J. Temmyo, *Appl. Phys. Lett.* **72**, 1341 (1998).
- [4] V. K. Kalevich, M. Paillard, K. V. Kavokin, X. Marie, A. R. Kovsh, T. Ammand, A. E. Zhukov, Yu. G. Musikhim, V. M. Ustinov, E. Vanelle, and B. P. Zakharchenya, *Phys. Rev. B* **64**, 45309 (2001).
- [5] X. Marie, T. Ammand, P. Le Jeune, M. Paillard, P. Renucci, L. E. Golub, V. D. Dymnikov, and E. L. Ivchenko, *Phys. Rev. B* **60**, 5811 (1999).
- [6] I. E. Kozin, V. G. Davydov, I. V. Ignatiev, A. V. Kavokin, K. V. Kavokin, G. Malpuech, H. W. Ren, M. Sugisaki, S. Sugou, and Y. Masumoto, *Phys. Rev. B* **65**, 241312 (2002).
- [7] I. E. Yugova, I. Y. Gerlovin, V. G. Davydov, I. V. Ignatiev, I. E. kozin, H. W. Ren, M. Sugisaki, S. Sugou, and Y. Masumoto, *Phys. Rev. B* **66**, 235312 (2002).
- [8] I. V. Ignatiev, T. Okuno, S. Y. Verbin, I. A. Yugova, and Y. Masumoto, *Physica E* **17**, 365 (2003).
- [9] Y. Masumoto, I. V. Ignatiev, K. Nishibayashi, T. Okuno, S. Y. Verbin, and I. A. Yugova, *J. Lumin.* **108**, 177 (2004).

- [10] J. A. Gupta, D. D. Awschalom, X. Peng, and A. P. Alivisatos, *Phys. Rev. B* **59**, 10421 (1999).
- [11] J. A. Gupta, E. L. Efros, A. V. Rodina, and D. D. Awschalom, *Phys. Rev. B* **66**, 125307 (2002).
- [12] S. A. Crooker, D. D. Awschalom, J. J. Baumberg, F. Flack, and N. Samarth, *Phys. Rev. B* **56**, 7574 (1997).
- [13] R. Akimoto, K. Ando, F. Sasaki, S. Kobayashi, and T. Tani, *Phys. Rev. B* **57**, 7208 (1998).
- [14] A. V. Kimel, F. Bentivegna, V. N. Gridnev, V. V. Pavlov, R. V. Pisarev, and Th. Rasing, *Phys. Rev. B* **63**, 235201 (2001).
- [15] Y. Mitsumori, A. Oiwa, T. Slupinski, H. Maruki, Y. Kashimura, F. Minami, and H. Munekata, *Phys. Rev. B* **69**, 33203 (2004).
- [16] Y. K. Kato, R. C. Myers, A. C. Gossard, and D. D. Awschalom, *Science* **306**, 1910 (2004).
- [17] K. Nishibayashi, T. Okuno, H. W. Ren, and Y. Masumoto, *Phys. Rev. B* **68**, 35333 (2003).
- [18] F. Meier and B. P. Zakharchenya: Eds., *Optical Orientation* (North-Holland, Amsterdam, 1987).
- [19] G. L. Bir, A. G. Aronov, and G. E. Pikus, *Sov. Phys. JETP* **42**, 705 (1976).
- [20] S. Sugano and N. Kojima: Eds., *Magneto-Optics* (Springer, Berlin, 2000).
- [21] K. Sato, *Jpn. J. Appl. Phys.* **20**, 2403 (1981).
- [22] K. Sato, H. Hongou, H. Ikekame, Y. Tosaka, M. Watanabe, K. Takanashi, and H. Fujimori, *Jpn. J. Appl. Phys.* **32**, 989 (1993).
- [23] J. J. Baumberg, S. A. Crooker, D. D. Awschalom, N. Samarth, F. Luo, and K. Furdyna, *Phys. Rev. B* **50**, 7689 (1994).

- [24] J. Fabian and S. Das Sarma, *J. Vac. Sci. Technol. B* **17**, 1708 (1999).
- [25] M. I. D'yakonov, *cond-mat/0404391* (2003).
- [26] B. G. Dick Jr. and A. W. Overhauser, *Phys. Rev.* **112**, 90 (1958).
- [27] G. Lampel, *Phys. Rev. Lett.* **20**, 491 (1968).
- [28] A. Tackeuchi, Y. Nishikawa, and O. Wada, *Appl. Phys. Lett.* **68**, 797 (1996).
- [29] A. Tackeuchi, O. Wada, and Y. Nishikawa, *Appl. Phys. Lett.* **70**, 1131 (1997).
- [30] R. I. Dzhioev, K. V. Kavokin, V. L. Korenev, M. V. Lazarev, N. K. Poletaev, B. P. Zakharchenya, E. A. Stinaff, D. Gammon, A. S. Bracker, and M. E. Ware, *Phys. Rev. Lett* **93**, 216402 (2004).
- [31] A. V. Khaetskii and Yu. V. Nazarov, *Physica E* **6**, 470 (2000).
- [32] A. V. Khaetskii and Yu. V. Nazarov, *Phys. Rev. B* **61**, 12639 (2000).
- [33] A. V. Khaetskii and Yu. V. Nazarov, *Phys. Rev. B* **64**, 125316 (2001).
- [34] *Landolt-Börnstein, Numerical data and functional relationships in science and technology, New Series III/22a* (Springer, Berlin, 1986).
- [35] C. G. V. Walle, *Phys. Rev. B* **39**, 1871 (1989).
- [36] S. L. Chuang, *Phys. Rev. B* **43**, 9649 (1991).
- [37] S. Adachi, *GaAs and related materials: Bulk Semiconducting and Superlattice Properties* (Worlds Scientific Publishing, Singapore, 1994).
- [38] I. Vurgaftman, J. R. Meyer, and L. R. Ram-Mohan, *J. Appl. Phys.* **89**, 5815 (2001).
- [39] H. Gotoh, H. Ando, and T. Takagahara, *J. Appl. Phys.* **81**, 1785 (1997).

- [40] T. Okuno, H.-W. Ren, M. Sugisaki, K. Nishi, S. Sugou, and Y. Masumoto, *Jpn. J. Appl. Phys.* **38**, 1094 (1999).
- [41] D. S. Citrin, *Phys. Rev. Lett.* **69**, 3393 (1992).
- [42] E. L. Ivchenko and A. A. Kiselev, *Sov. Phys. Semicond.* **26**, 827 (1992).
- [43] J. M. Kikkawa and D. D. Awschalom, *Phys. Rev. Lett.* **80**, 4313 (1998).
- [44] S. Wittekoek, T. J. A. Popma, J. M. Robertson, and P. F. Bongers, *Phys. Rev. B* **12**, 2777 (1975).
- [45] H. Kosaka, A. A. Kiselev, F. A. Baron, K. W. Kim, and E. Yablonovitch, *Elec. Lett.* **37**, 464 (2001).

# List of Publications

1. **"Photoinduced electric dipole in CuCl quantum dots"**

Yasuaki Masumoto, Fumitaka Naruse and Atsushi Kanno

Journal of Luminescence **102**, 629 (2003).

2. **"Longitudinal optical phonons in the excited state of CuBr quantum dots"**

Jialong Zhao, Atsushi Kanno, Michio Ikezawa and Yasuaki Masumoto

Physical Review B **68**, 113305 (2003).